UNIVERSITY OF CALIFORNIA SAN DIEGO

Exploration and Characterization of Thin Film Materials for Future Battery and Memory Device

A Dissertation submitted in partial satisfaction of the requirements
for the degree Doctor of Philosophy

in

Nanoengineering

by

Ryosuke Shimizu

Committee in charge:

    Professor Ying Shirley Meng, Chair
    Professor Jian Luo, Co-Chair
    Professor David P. Fenning
    Professor Eric E. Fullerton
    Professor Ping Liu

2023

The Dissertation of Ryosuke Shimizu is approved, and it is acceptable in quality and form for publication on microfilm and electronically.

University of California San Diego

2023

DEDICATION

To my family

TABLE OF CONTENTS

LIST OF FIGURES

LIST OF TABLES

ACKNOWLEDGEMENTS

I also would like to thank my collaborators and coauthors, Jamie Weaver from NIST, and Dr. Mingjie Xu and Dr. Xiaoqing Pan from UC Irvine for their technical support and knowledge.

Moreover, I appreciate my family for their total support physically, mentally and financially.

Chapter 3, in full, is a reprint of the material as it appears in Shimizu, R.*; Cheng, D.*; Weaver, J. L.; Zhang, M.; Lu, B.; Wynn, T. A.; Burger, R.; Kim, M.; Zhu, G.; Meng, Y. S. Unraveling the Stable Cathode Electrolyte Interface in All Solid-State Thin-Film Battery Operating at 5 V. Advanced Energy Materials 2022, 2201119. The dissertation author was the co-primary investigator of this paper.

Chapter 4, in part, is currently being prepared for submission for publication of the material as Shimizu, R.; Cheng, D.; Zhu, G.; Han, B.; Burger, R.; Xu, M; Pan, X.; Zhang, M.; Meng, Y.S., Elucidating Dynamic Conductive State Changes in amorphous Lithium Lanthanum Titanate for Resistive Switching Devices. All the parts in the manuscript were developed and performed by the author.

Chapter 5 contains unpublished materials coauthored with Weikang Li. The dissertation author was the primary author of this chapter.

VITA

2012   Bachelor of Science in Physics, Tohoku University, Japan

2015   Master of Science in Physics, Tohoku University, Japan

2023   Doctor of Philosophy in Nanoengineering, University of California San Diego

PUBLICATIONS

(* authors contributed equally to the work)

Shimizu, R.; Cheng, D.; Zhu, G.; Han, B.; Burger, R.; Xu, M; Pan, X.; Zhang, M.; Meng, Y.S., Elucidating Dynamic Conductive State Changes in amorphous Lithium Lanthanum Titanate for Resistive Switching Devices. *Manuscript in-preparation*.

Shimizu, R.*; Cheng, D.*; Weaver, J. L.; Zhang, M.; Lu, B.; Wynn, T. A.; Burger, R.; Kim, M.; Zhu, G.; Meng, Y. S. Unraveling the Stable Cathode Electrolyte Interface in All Solid-State Thin-Film Battery Operating at 5 V. *Advanced Energy Materials* **2022**, 2201119.

Cheng, D.; Wynn, T.; Lu, B.; Marple, M.; Han, B.; **Shimizu, R.**; Sreenarayanan, B.; Bickel, J.; Hosemann, P.; Yang, Y.; Nguyen, H.; Li, W; and Zhu, G.; Zhang, M.; Meng, Y.S. Freestanding LiPON: from fundamental study to uniformly dense Li metal deposition under zero external pressure. *Accepted in Nature Nanotechnology* **2023**

Yao, W.; Chouchane, M.; Li, W.; Bai, S.; Liu, Z.; Li, L.; X. Chen, A.; Sayahpour, B.; **Shimizu, R.**; Raghavendran, G.; A. Schroeder, M.; Chen, Y.-T.; S. Tan, D. H.; Sreenarayanan, B.; K. Waters, C.; Sichler, A.; Gould, B.; J. Kountz, D.; J. Lipomi, D.; Zhang, M.; Shirley Meng, Y. A 5 V-Class Cobalt-Free Battery Cathode with High Loading Enabled by Dry Coating. *Energy & Environmental Science* **2023**, *16* (4), 1620–1630.

Li, Y.; Li, W.; **Shimizu, R.**; Cheng, D.; Nguyen, H.; Paulsen, J.; Kumakura, S.; Zhang, M.; Meng, Y. S. Elucidating the Effect of Borate Additive in High-Voltage Electrolyte for Li-Rich Layered Oxide Materials. *Advanced Energy Materials* **2022**, *12* (11), 2103033.

Li, W.; Cheng, D.; **Shimizu, R.**; Li, Y.; Yao, W.; Raghavendran, G.; Zhang, M.; Meng, Y. S. Artificial Cathode Electrolyte Interphase for Improving High Voltage Cycling Stability of Thick Electrode with Co-Free 5 V Spinel Oxides. *Energy Storage Materials* **2022**, *49*, 77–84.

Hirsh, H.; Li, Y.; Cheng, J.-H.; Shimizu, R.; Zhang, M.; Zhao, E.; Meng, Y. S. The Negative Impact of Transition Metal Migration on Oxygen Redox Activity of Layered Cathode Materials for Na-Ion Batteries. *J. Electrochem. Soc.* **2021**, *168* (4), 040539.

Bao, W.; Fang, C.; Cheng, D.; Zhang, Y.; Lu, B.; Tan, D. H. S.; Shimizu, R.; Sreenarayanan, B.; Bai, S.; Li, W.; Zhang, M.; Meng, Y. S. Quantifying Lithium Loss in Amorphous Silicon Thin-Film Anodes via Titration-Gas Chromatography. *Cell Reports Physical Science* **2021**, *2* (10), 100597.

Marple, M. A. T.; Wynn, T. A.; Cheng, D.; Shimizu, R.; Mason, H. E.; Meng, Y. S. Local Structure of Glassy Lithium Phosphorus Oxynitride Thin Films: A Combined Experimental and Ab Initio Approach. *Angewandte Chemie International Edition* **2020**, *59* (49), 22185–22193.

Li, W.; Cho, Y.-G.; Yao, W.; Li, Y.; Cronk, A.; Shimizu, R.; Schroeder, M. A.; Fu, Y.; Zou, F.; Battaglia, V.; Manthiram, A.; Zhang, M.; Meng, Y. S. Enabling High Areal Capacity for Co-Free High Voltage Spinel Materials in next-Generation Li-Ion Batteries. *Journal of Power Sources* **2020**, *473*, 228579.

Cheng, D.; Wynn, T. A.; Wang, X.; Wang, S.; Zhang, M.; Shimizu, R.; Bai, S.; Nguyen, H.; Fang, C.; Kim, M.; Li, W.; Lu, B.; Kim, S. J.; Meng, Y. S. Unveiling the Stable Nature of the Solid Electrolyte Interphase between Lithium Metal and LiPON via Cryogenic Electron Microscopy. *Joule* **2020**, S2542435120303949.

Ghalgaoui, A.; Shimizu, R.; Hosseinpour, S.; Álvarez-Asencio, R.; McKee, C.; Johnson, C. M.; Rutland, M. W. Monolayer Study by VSFS: In Situ Response to Compression and Shear in a Contact. *Langmuir* **2014**, *30* (11), 3075–3085.

ABSTRACT OF THE DISSERTATION

Exploration and Characterization of Thin Film Materials for Future Battery and Memory

Device

by

Ryosuke Shimizu

Doctor of Philosophy in Nanoengineering

University of California San Diego, 2023

Professor Ying Shirley Meng, Chair
Professor Jian Luo, Co-Chair

Lithium-ion batteries have been growing rapidly for the past few decades, finding application in portable devices such as cell phones, and laptop computers. Recently, the surging demand for electric vehicles and grid storage necessitates the development of safer batteries that offer higher performance, longer life, and lower cost. Spinel-type $LiNi_{0.5}Mn_{1.5}O_4$ (LNMO) stands out as a promising cathode material for 5 V-class Li-ion batteries enabling high energy density and low material costs. However, common carbonate-based liquid electrolytes suffer

from oxidative decomposition under high voltage, resulting in continuous cell degradation. In contrast, certain solid-state electrolytes have a wide electrochemical stability range and can withstand the required oxidative potential. In this study, we test a thin-film battery comprising an LNMO cathode with a solid lithium phosphorus oxynitride (LiPON) electrolyte and characterized their interface before and after cycling. Utilizing Li metal as the anode, this system can deliver stable performance for 600 cycles with an average Coulombic efficiency exceeding 99%. Neutron depth profiling reveals a slight overlithiated layer at the interface prior to cycling, a result that is consistent with the excess charge capacity measured during the first cycle. Additionally, cryogenic electron microscopy indicates intimate contact between LNMO and LiPON without any noticeable structure or chemical composition evolution after extended cycling, underscoring the superior stability of LiPON against a high voltage cathode. These findings accelerate the commercialization of a high voltage cell with solid or liquid electrolytes.

In addition to thin film batteries, the thin film platform of battery materials offers another potential application in the form of a resistive switching device for future computing. With conventional silicon-based memory devices approaching their quantum mechanical limits, it is imperative to seek new functional materials to replace them. Therefore, in this thesis, solid-state electrolyte lithium lanthanum titanate (LLTO) is explored as a resistive switching device, and its material properties are investigated through micro and macroscopic characterization. Electronic conductivity changes that provoke the LLTO switching are investigated experimentally and computationally through the comparison of LLTO with different oxygen compositions, under the hypothesis that oxygen vacancy plays a role in altering local LLTO conductivity. Based on those data, switching mechanisms are proposed as filament growth created by local conductivity change through a simplified model.

Chapter 1 Background and Introduction

1.1 Lithium-ion battery - Demands as Energy Storage

Within a few decades, global warming has been an issue and government, researchers, industries, etc. have been trying to solve this problem with developing sustainably. Greenhouse gas including CO_2, CH_4 and N_2O is considered to cause the global warming and emitted by variety of sectors as shown Figure 1.1[1]. In the largest category (inner pie chart in Figure 1.1), energy sector occupies about three quarters of the total gas emissions, in which energy sector consists of electricity, heat and transport. To reduce the emissions, energy storage such as batteries plays an important role. For instance, electrification of vehicles by replacing conventional combustion engines with motor and battery directly contributes to reduction in greenhouse gas emissions or potentially zero-emission. This electrification can influence other sectors, such as motorcycles, farming tools/vehicles, airplanes, which rely on combustion engines as a power train. Furthermore, energy storage can maximize the use of green energy e.g. made by photovoltaic (PV, also known as solar) power. Solar cell devices that convert solar power to electricity, and, thus, are regarded as sustainable energy resources. These are equipped on roofs of houses and parking lots in a small scale or arranged in vacant land as a "mega-solar" power plant. Although, solar power seems almost perfect solution to generate electricity without CO_2, there is a mismatch of supply and demand in an actual situation. While electricity supply generated by PV cells in daytime around noon, the demand for the electricity peaks at around evening, when majority of people go back home from work and start using electricity at home[2] (Figure 1.2). Such a mismatch between the supply and demand causes some loss of the generated energy, leading to inefficient use of energy. To address it, energy storage can be used as a grid storage, where batteries store electricity generated by PV cells in daytime and provide it when it is needed in evening time. As exemplified

above, battery technologies are necessary in our daily life and future to slow down or stop global

warming.
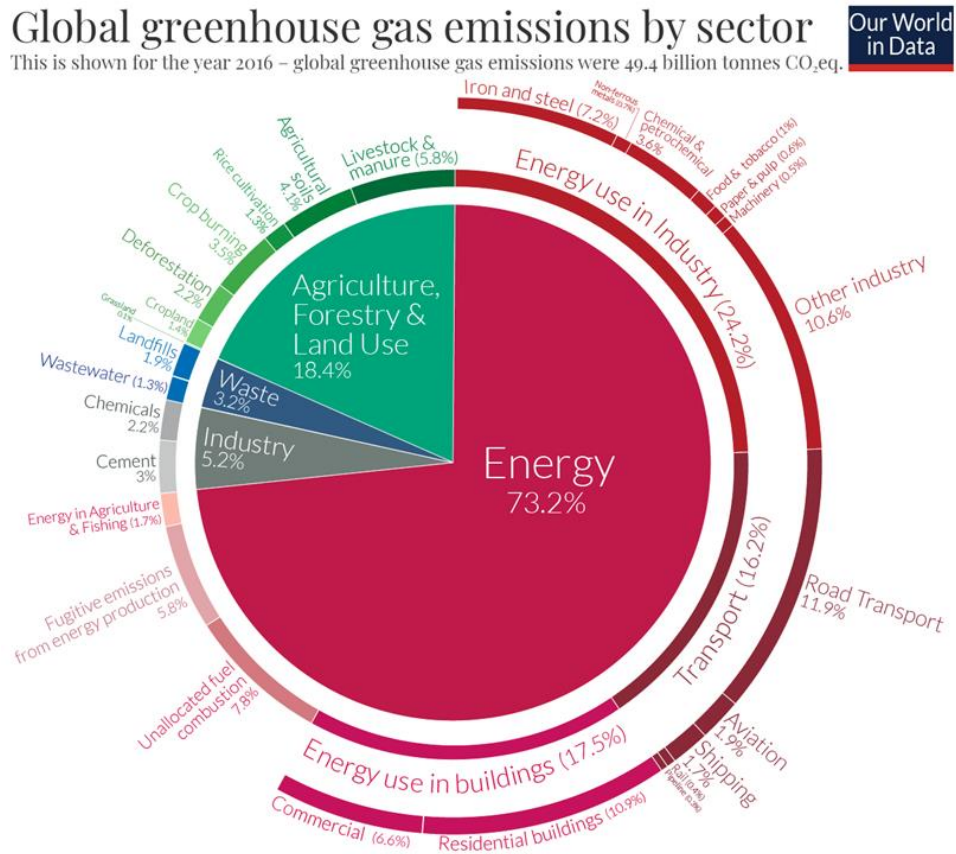
Figure 1.1 Global greenhouse gas emissions breakdown by sector[1] in 2016.
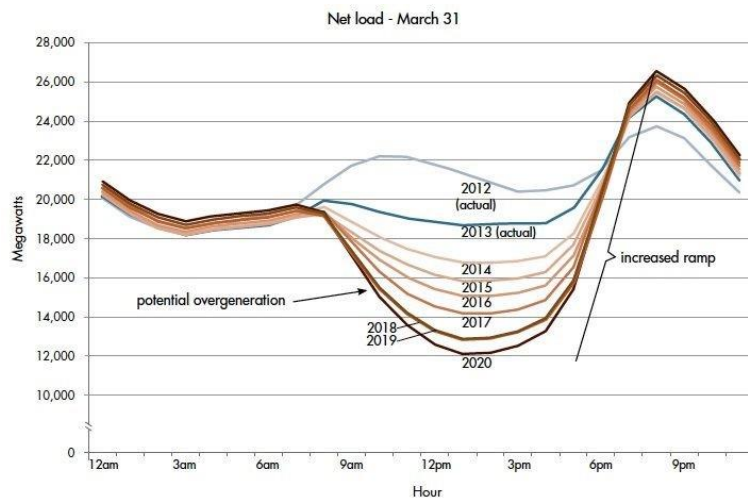
Figure 1.2 Daily energy consumption curve in California, known as "Duck curve"[2].

When lithium-ion batteries were first commercialized, they were utilized as a rechargeable power source in portable devices such as cell phones and laptop computers. In such devices, only one or a few cells (packs) were needed since required power and capacity was relatively not so much and they were easily charged every day. However, as the demand for the batteries to electric vehicles (EV) and grid storage increases, more cells with higher performance such as more capacity and longer cycler life are needed. Figure 1.3, indeed, demonstrates sales of (fully) electric vehicle (e.g. Tesla) significantly grows within past ten years while hybrid electric vehicle (e.g. Prius from Toyota), meaning simply more batteries are needed, and additionally higher capacity and long life cycles are required to guarantee the quality and performance of the EVs.
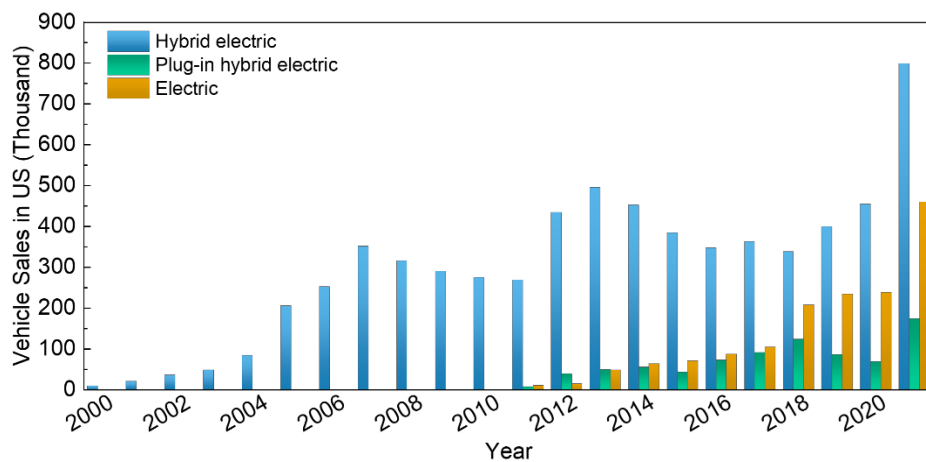
Figure 1.3 Hybrid-Electric (HEV), Plug-in Hybrid-Electric (PHEV) and Electric Vehicle (EV) Sales in US vs. year[3].

1.2 Lithium-ion battery - Basic Mechanism

In the previous section, I explained the need for batteries as an energy source and storage has been exponentially growing. In this section, the basic mechanism of conventional lithium-ion batteries is focused. Major components of Li-ion battery are two electrodes (cathode and anode), electrolyte, and separator. In a Li-ion battery, lithium ions are shuttled between cathode and anode electrodes through liquid electrolyte and electrons migrate through external circuit, resulting in

charge and discharge of a cell. During the charging process, Li ions are deintercalated from a cathode material, flow inside the electrolyte, and then intercalated into an anode material. The reactions happening in each electrode are shown as follows with using LiCoO$_2$ as a cathode and graphite (C) as an anode, which are most popular electrode materials[4]:

$$LiCoO_2 = Li_{1-x}CoO_2 + xLi^+ + xe^- \text{ (cathode)}$$

$$C + xLi^+ + xe^- = Li_xC \text{ (anode)}$$
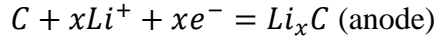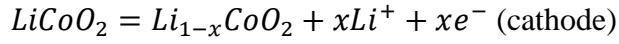
On cathode side, Li ions and electrons are extracted from cathode with the oxidation reaction of cobalt from 3+ to 4+ to compensate total charge.
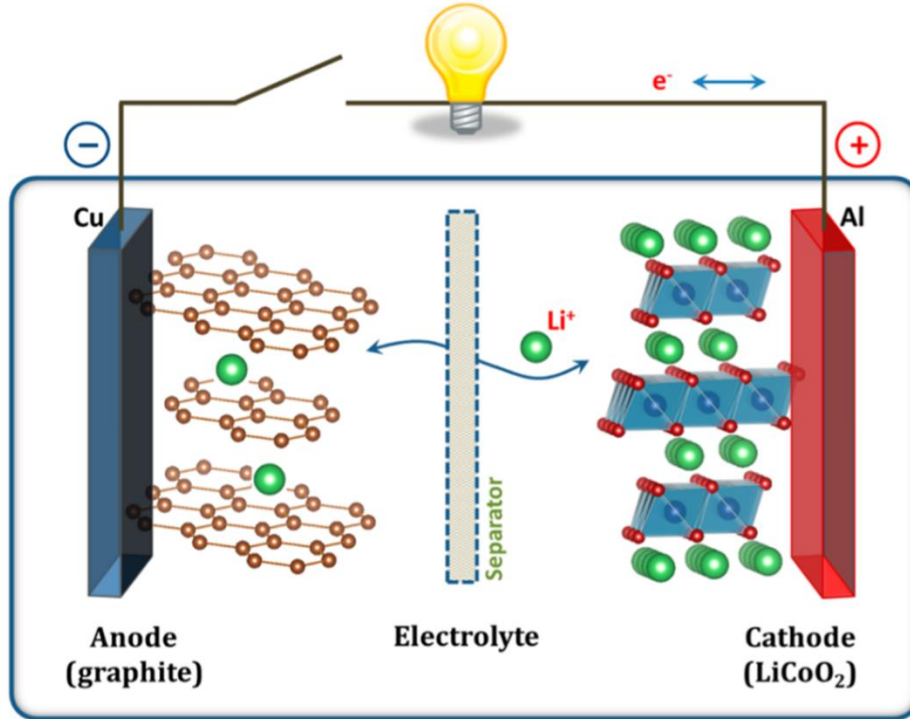
Figure 1.4 Schematic picture of the commercialized Li-ion battery, where LiCoO$_2$ as a cathode and graphite as an anode are in electrolyte with Li$^+$ salt[4].

Theoretical cell voltage, E, is thermodynamically determined by the equation $\Delta\mu = -zFE$, where $\Delta\mu$ is difference of lithium chemical potential between two electrodes, z is the number of charges, F is Faraday constant[5]. From this equation, it is found that to establish higher-voltage

battery, aiming for batteries with higher power and higher energy density, anode should have lower reduction potential and cathode should have high oxidative potential[6]. Not only voltage value but also voltage curve is an important factor to determine cell quality and to interpret essential reactions inside cells. As shown in Figure 1.5, voltage curve of each cathode material varies and are classified to two types: flat (LiFePO$_4$, LiFeSO$_4$F) and slopy (LiCoO$_2$, LiNi$_{0.33}$Co$_{0.33}$Mn$_{0.33}$O$_2$, etc.) lines. To understand how the voltage curve behaves, Gibbs phase rule should be considered, which is represented as $F = C - P + 2$. Here, C is the number of components present, P is the number of phases present, and F is the number of degrees of freedom.
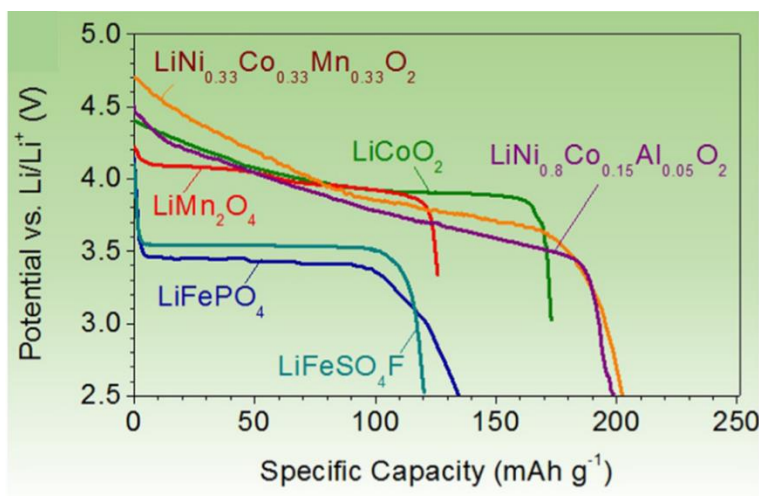
Figure 1.5 Voltage curve of typical cathode materials.

1.3 All solid-state battery

Currently, the batteries used in EVs and HEVs consist of electrodes and liquid electrolyte. However, conventional batteries have a risk of fire due to organic solvent inside. All the automobile companies that sell EVs or HEVs attempt to protect battery system in the vehicle from electric shortening, fire, and physical destruction due to crash and tough environments such as flooding and high and low temperature. Therefore, it is natural to explore alternative, inflammable electrolytes. One of the solutions is to use solid-state electrolyte. Commercialization of solid-state

batteries would be able to not only make vehicle safe but also reduce parts that have been used for the protection of battery systems, such as solid case covering battery modules or sensors working to detect a crash and stop the electric supply. This is more applicable to vehicles with more batteries such as PHEVs and EVs. Consequently, replacing liquid electrolytes to solids electrolyte leads to reducing the total weight of a vehicle and lead EVs, resulting in longer all-electric range per one charge.

From the viewpoint on the material level, using solid electrolyte is also beneficial. Because some solid electrolytes have a voltage window around 5 V, which is a highly oxidative environment for conventional liquid electrolyte, they are usable with high voltage cathode materials such as $LiNi_{0.5}Mn_{1.5}O_4$ (LNMO)[7–11]. Furthermore, solid state batteries are free from the issue of transition metal dissolution from a cathode, which occurred in batteries with liquid electrolytes[8,12–14]. On the anode side, proper choice of solid electrolytes potentially enables us to utilize Li metal, leading to high energy density when they are packaged as a cell.[15]

Among solid electrolytes, there are two promising types of solid electrolytes, sulfide-based electrolytes, and oxide-based electrolytes. Sulfide-based solid electrolytes mostly have higher ionic conductivity ($\sim 10^{-5}$ to 10^{-2} S cm^{-1}) than oxide-based one ($\sim 10^{-6}$ to 10^{-3} S cm^{-1}) as summarized in Figure 1.6. This is because sulfide ions are larger than oxide ions, so the channels where lithium ions pass through are wider. In addition, because sulfide ions have higher polarizability than oxide ions, the framework consisting of sulfide is less attractive to Li ions than the oxide framework. Therefore, Li ions are likely to be more movable, which results in higher ionic conductivity. Another advantage of sulfide-based solid electrolytes is that they are soft materials. Thus, electrolyte particles can be densely packed, which leads to low grain boundary resistance[16]. However, ionic conductivity is not only the critical factor to determine solid electrolytes, but

chemical and electrochemical stability should also be considered. The problem of sulfide-based solid electrolytes is chemical instability against humidity in the atmosphere, which requires careful moisture control, particularly, in the manufacturing phase. Muramatsu et al., for example, studied the structural change of solid electrolyte L_2S_5-P_2S_5. They investigated the amount of harmful H_2S, which is generated from L_2S-P_2S_5 by its decomposition after exposure to the air with humidity[17].Compared to Sulfide-based solid electrolytes, oxide-based ones are chemically more stable and, thus, various types of oxide-based solid electrolytes have been investigated.
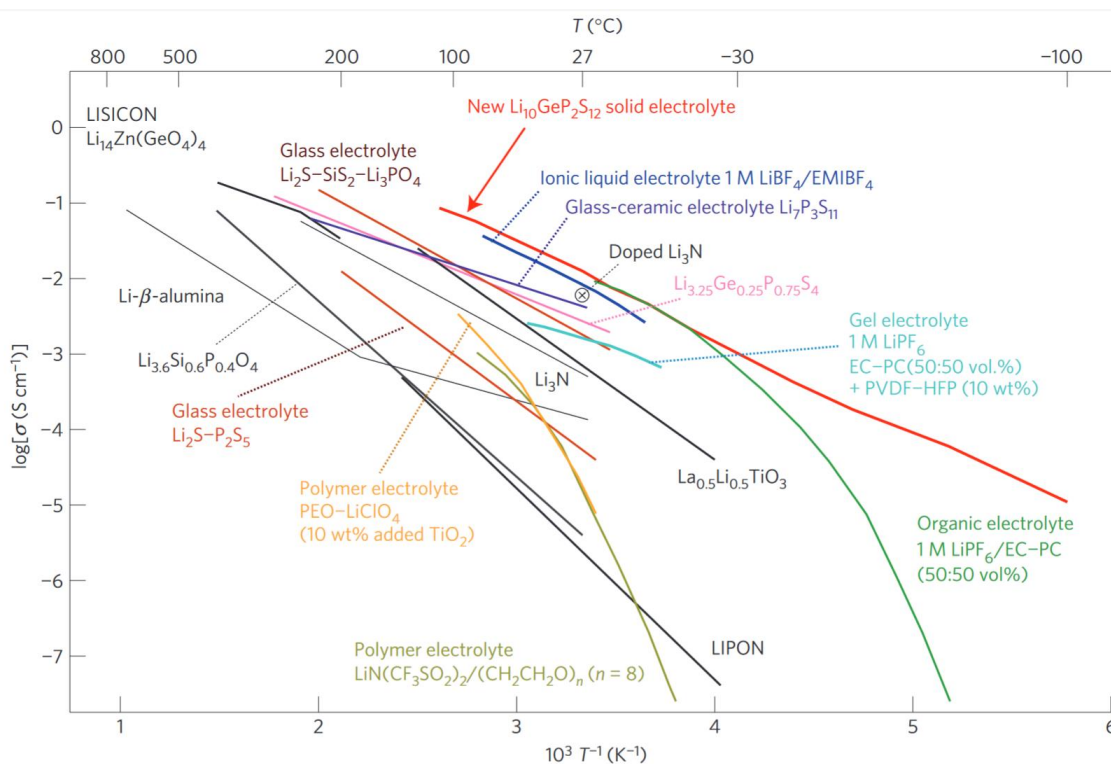
Figure 1.6 Ionic conductivities of major solid-state electrolytes[18].

When we select solid state electrolyte for solid state battery, electrochemical stability, where electrolytes are coupled with cathode and anode under a certain electric potential during a battery operation, should be considered, as well as ionic conductivity. Figure 1.7 shows electrochemical stability window of various solid electrolytes predicted by computation[19], representing that voltage stability, especially high voltage side, is depending on anions in the

electrolytes. When the battery is operated, chemical potential shifts higher in anode and lower in cathode. If these shifts exceed the electrochemical window of the solid electrolyte, the electrolyte is decomposed, forming solid electrolyte interphase (SEI) and cathode electrolyte interphase (CEI) (Figure 1.8)[20]. Thus, while sulfur-electrolytes has narrow stability window that tend to cause decomposition during cell operation and form SEI/CEI at the interface, oxide-type is stable at high voltage but at low voltage. Therefore, sulfur-type electrolytes require the study to engineer SEI and CEI formation to make system stable, not interfering cycling reaction once they are formed. On the contrary, oxide-type electrolytes need to focus more on anode/electrolyte interface, especially Li/electrolyte interface, since it is intrinsically stable against oxidation reaction at the cathode side.

In the later sections, lithium phosphate (Li_3PO_4, or LPO), lithium phosphorous oxynitride (LiPON), and lithium lanthanum titanate (LLTO) are explained more in details because the fabrication method of these thin film (sputtering and pulsed laser deposition) is suitable for oxide-type electrolytes, where oxygen can be introduced during the deposition.
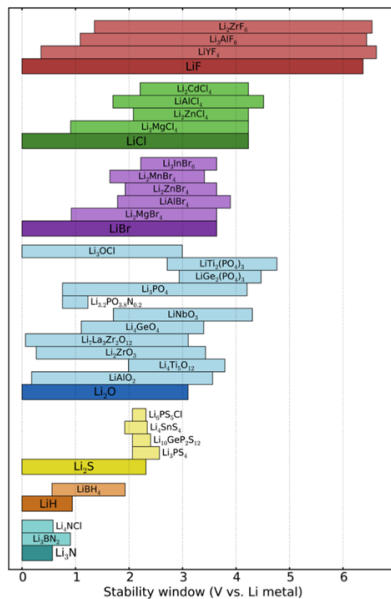
Figure 1.7 Electrochemical stability window of various solid electrolyte materials, studied by first-principles methodology[19].
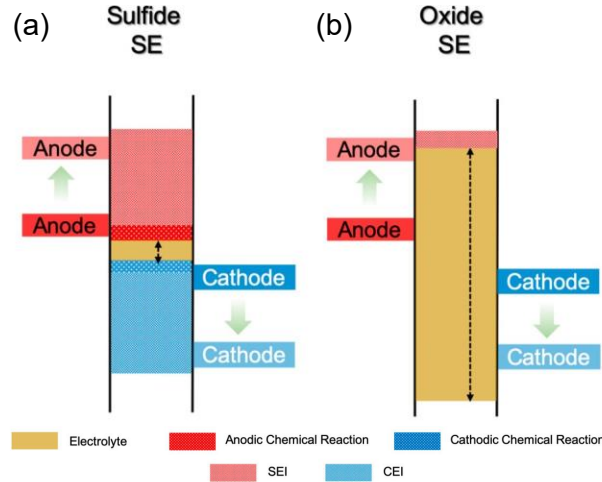
Figure 1.8 Schematic diagram of HOMO and LUMO of the different types of electrolytes against cathode and anode chemical potential: (a) Sulfur-type and (b) oxide-type electrolyte[20].

1.4 All solid-state thin film Battery

All solid-state thin film batteries are one type of solid-state batteries. It comprises layers of thin films deposited by physical vapor deposition (PVD), chemical vapor deposition (CVD), and/or atomic layer deposition (ALD). Compared to porous, bulk batteries, thin film batteries have micron to tens of microns of thickness and each layer is densely packed and stacked, where electrode/electrolyte interface is in good contact even without external pressure. Such small-sized features can fit semiconductor chip production, enabling us to integrate it use it in wearable device, devices for IoT (internet of things), medical implants, energy harvesting, and smart cards[21].

Although the first Li-based thin film battery was invented in 1969 by Liang and Bro as Li/LiI/AgI system[22], the breakthrough that leads to modern thin-film lithium rechargeable batteries has been made by the invention of lithium phosphorous oxynitride (LiPON) by Bates et al[23] from Oak Ridge National Lab (ORNL), USA. Typical thin-film batteries are fabricated as shown in Figure 1.9 and various kinds of substrates, electrodes, and electrolytes are selected. To avoid unwanted electrical leakage, substrates are typically selected from insulative material such as Al_2O_3 or SiO_2 coated Si wafer, which are easy to access and process. On top of the substrate, layers

9

of cathode, solid electrolyte, and anode, as well as current collectors, are deposited by PVD, CVD, or ALD. The cell needs to have protective coating to protect air-sensitive electrodes/electrolyte from air-exposure when it is cycled outside of the glovebox. In the early stage of the development researchers including ORNL group has invented various types of thin film batteries with LiPON as an electrolyte, for instance, lithium-ion thin-film batteries (V_2O_5[24] or amorphous silicon tin oxynitride as an anode[25]), lithium-metal thin film batteries[26–29] (Li-metal as an anode), and lithium-free thin-film batteries[30] (also known as anode-free batteries). Currently, numerous types of materials are selected as cathode, anode, and electrolyte, as performance of these materials are verified in bulk batteries (see Figure 1.10), and further improvement of the fabrication process and cell performance are critical for both fundamental study and device application.
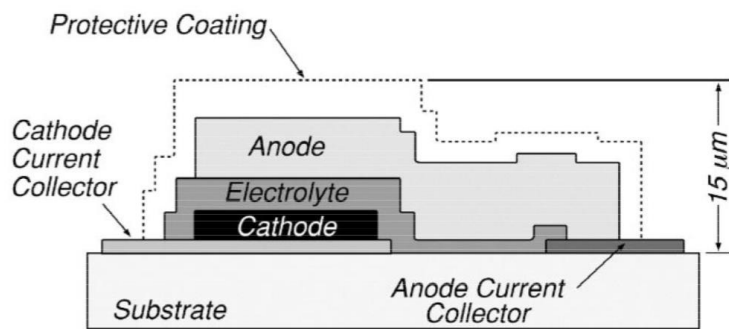
Figure 1.9 Schematic illustration of typical thin film battery[31].
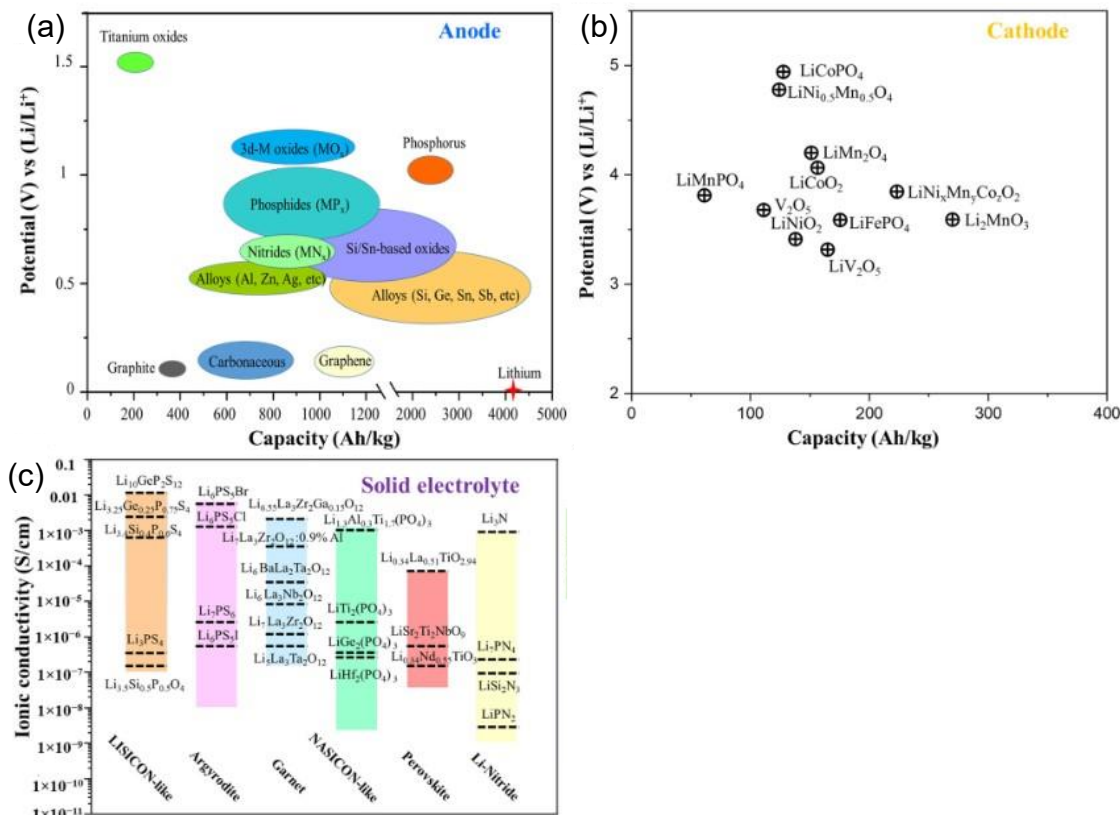
Figure 1.10 Various materials that has been used for thin-film batteries: (a) Anode materials, (b) cathode materials, and (c) electrolyte materials[21].

1.5 Thin-film battery materials

As discussed in the previous section and shown in Figure 1.10, various materials have been used as thin film batteries. Here, I will focus on three materials that are important for my dissertation research: High-voltage cathode material $LiNi_{0.5}Mn_{1.5}O_4$ (LNMO), glassy solid electrolyte lithium phosphorous oxynitride (LiPON), and high conductivity solid electrolyte lithium lanthanum titanate (LLTO).

1.5.1 5 V-class High Voltage Cathode Material: $LiNi_{0.5}Mn_{1.5}O_4$

Spinel-type cathode material, $LiNi_{0.5}Mn_{1.5}O_4$ (LNMO) has been attracting significant attention due to its high operating voltage and low material cost (Co-free). In stoichiometric LNMO, all Li atoms sit in 8a tetrahedral sites and are intercalated/deintercalated reaction during

11

normal operation at above 3.5 V, giving voltage plateau at 4.7 V corresponding to Ni redox

reaction between 4+ and 2+. In a cell using LNMO, voltage range is generally set between 3.5 V

and 5.0 V, where Li composition changes from 0 to 1 in the stoichiometry $Li_xNi_{0.5}Mn_{1.5}O_4$.

However, LNMO can accommodate more Li than 1 by transforming its cubic structure to

tetragonal structure, where Li atoms sit in 16c octahedral sites, instead of 8a sites, and structure is

elongated in c direction due to Jahn-Teller distortion of transition metal octahedrons. This phase

transformation is reversible reaction as shown in Figure 1.11 (a) and by Kawasoko et al[32]. In their

work, they achieved to double the cell capacity although the voltage is about 3 V in the half of the

charge and discharge capacity.
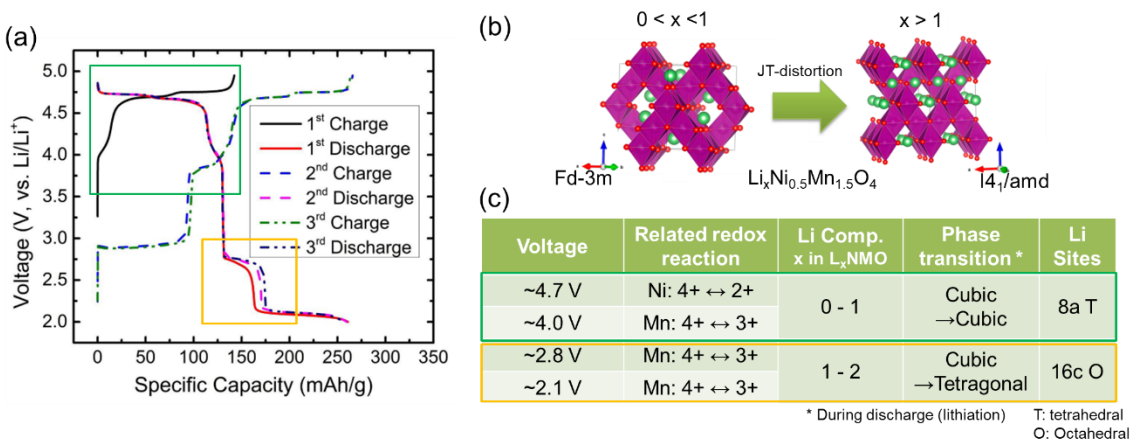
Figure 1.11 LNMO voltage and structure. (a) Voltage curve at 2 - 5 V, (b) structural change below 3 V, and (c) summary of voltage, redox reaction and LNMO phase.[33]

While such high operating voltage is an attractive characteristic, e.g., for the application to

EVs, the cell using LNMO suffered from limited cycle life due to severe degradation. In particular,

when LNMO is coupled with conventional liquid electrolytes ($LiPF_6$ salt with carbonate-based

solvent), the electrolyte experiences high oxidative environment on the cathode surface during

charging or storage after charge, leading to electrolyte decomposition[34-36]. To avoid the negative

reactions between LNMO and liquid electrolytes, proper passivation layers are required to be

formed artificially by coating[37] or chemically by additives[37], helping further corrosion reaction on

cathode surface. Another solution is to replace liquid electrolyte with solid electrolyte, which can prevent transition metal dissolution and migration from cathode to anode[8,13,38]. As an example, the coupling LNMO cathode with LiPON solid electrolyte will be illustrated in the next section.

Thin film LNMO was firstly fabricated by electrostatic spray deposition by Mohamedi et al.[39] and, later then, by pulsed laser deposition (PLD) by Xia et al[40,41]. Voltage curve of their LNMO film represents almost identical to that of bulk LNMO electrode, meaning there is no impurity phase formation in the film. Moreover, Konishi et al. have developed an epitaxial LNMO thin film, which has a specific crystalline orientation by choosing a $SrTiO_3$ substrate with similar lattice parameters[42]. The films with the controlled crystalline orientation facilitated to clarify crystalline-orientation dependent surface reactions with coating materials and electrolytes[43,44].

1.5.2 Glassy Solid-State electrolyte: LiPON

Lithium phosphorous oxynitride (LiPON) has been one of the key solid-state electrolyte materials since its development[45] that pioneered lithium rechargeable thin-film batteries due to its accessible fabrication process (RF sputtering), decent ionic conductivity ($\sim 10^{-6}$ S/cm), and compatibility against various cathode and anode materials. Indeed, most of the early development of thin-film battery employed LiPON as mentioned in section 1.4, and LiPON is still used as a solid-state electrolyte or coating material[46,47] to avoid direct contact between cathode and electrolyte.

LiPON has been coupled with $LiCoO_2$ (LCO)[48–50], $LiMn_2O_4$ (LMO)[51,52], $LiNi_{0.6}Mn_{0.2}Co_{0.2}O_2$ (NMC622)[53], and $LiFePO_4$. Owing to its high oxidative stability, LiPON retains its functionality upon combination with high voltage cathode materials such as LNMO or NMC, or operation at high voltage. For instance, Li et al. demonstrated long-term stability of LiPON against LNMO in LNMO/LiPON/Li thin-film battery[54]. Their cell cycles exhibited great

capacity retention (90.6%) and coulombic efficiency (99.98%) after 10,000 cycles (Figure 1.12 (a) and (b), respectively), where irreversible capacity loss was minimal and voltage curve was identical with each other (Figure 1.12 (c) and (d), respectively). This result explicitly indicates LiPON's stability against a highly oxidative environment, in which conventional liquid electrolyte cannot survive. Furthermore, the long-term, stable cycling performance also demonstrated that LiPON has reduction stability against Li metal anode, while most of solid-electrolytes are thermodynamically or chemically not compatible with Li metal[19,55–57].
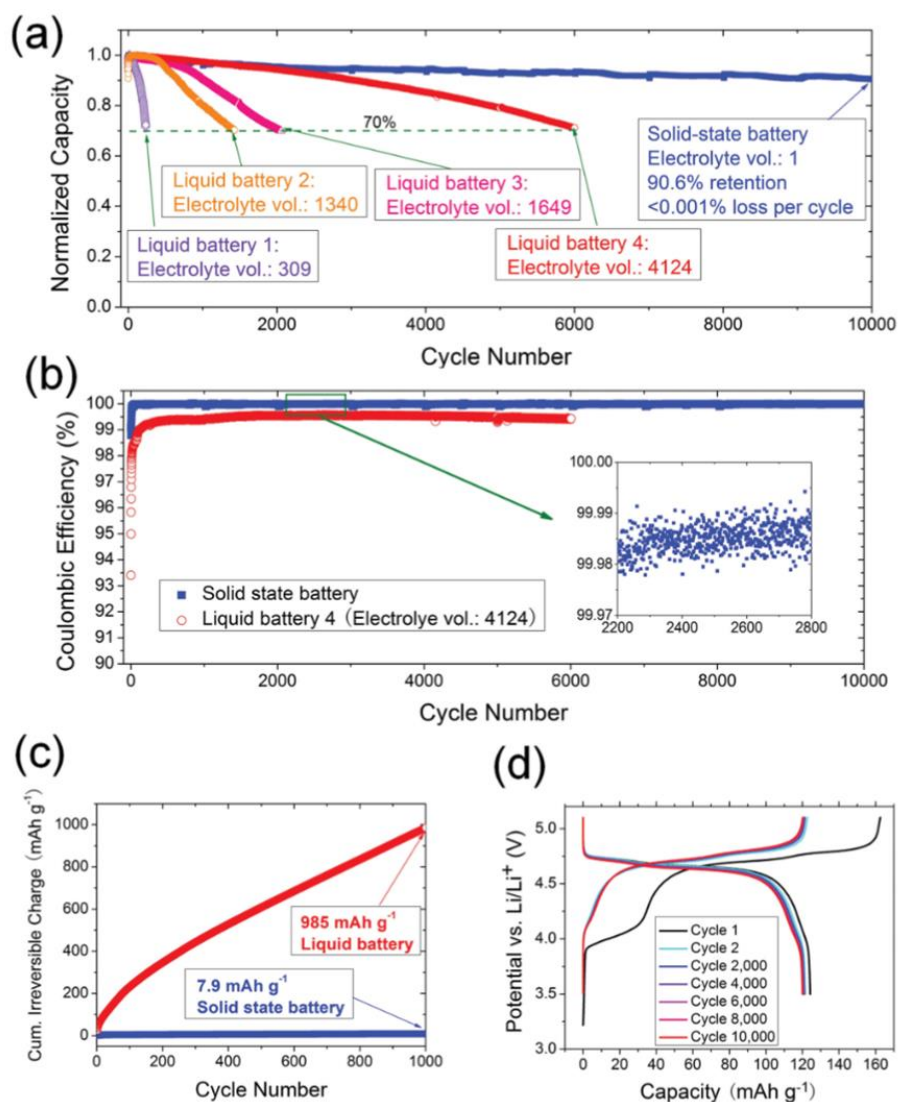
Figure 1.12 Cycling performance of LNMO/LiPON/Li metal thin-film battery[54]. (a) Capacity vs. cycle number, (b) Coulombic efficiency vs. cycle number, (c) cumulative irreversible charge capacity vs. cycle number, and (d) Voltage profile of the cell up to 10,000 cycles.

14

Until recently various aspects of LiPON and its interface have been directly and indirectly investigated, such as fabrication process, and (electro-)chemical compatibility, since interfacial resistance at a solid electrode and electrolyte interface is crucial to have better efficiency, cycle life, and rate performance. For example, Haruta et al. studied LiPON/LCO interface, measuring interfacial resistance with changing sputtering configuration[58]. They fabricated thin film batteries that consist of LCO cathode, LiPON electrolyte and Li anode on Al_2O_3 single crystal substrate with a gold current collector, where LiPON were deposited by sputtering in on-axis or off-axis configurations. The the thin film batteries properly worked with 97% coulombic efficiency after 100 cycles and electrochemical impedance spectroscopy (EIS) demonstrated 8.6 Ω cm^2 of interfacial resistance in Li/LiPON/LCO structure, where LiPON film was deposited by sputtering in off-axis configuration. In contrast, the thin film battery with LiPON deposited in on-axis configuration show about a hundred times higher resistance, 880 Ω cm^2, representing that the sputtering configuration makes difference in the interfacial resistance due to the sputtering damage on the LCO surface by nitrogen atoms. It is, therefore, confirmed that surface conditions such as damage and contamination through sputtering process directly affects interfacial resistance.

Kawasoko et al. also pointed out the importance of keeping interface clean and to mitigate the resistance[32,59,60]. In their work, Li_3PO_4 (LPO), which is source material of LiPON and has similar oxidation stability, is used as a solid electrolyte, and their deposition procedures were all done inside vacuum chamber, where there is no risk of air-exposure. As a result, surprisingly, the interface resistance of the LNMO/LPO interface was 7.6 Ω cm^2, which was much smaller than that observed in liquid-electrolyte-based batteries with LNMO (28.7Ω cm^2).

Till now, various studies have demonstrated stable, long-term stability of LiPON, paring with different cathode materials, followed by impedance spectroscopy to seek interfacial

resistance. However, little study has been done about direct observation at such interface, especially morphology and chemistry. This might be partially attributed to intrinsic air- and beam-sensitivity of LiPON[61], which makes it difficult to utilize electron microscopy techniques. By overcoming such research background and technical difficulty, our study in Chapter 3 firstly elucidate interface stability of high voltage cathode material LNMO and LiPON by using neutron depth profiling and cryo-electron microscopy.

1.5.3 Highly Ionic Conductive Solid-State Electrolyte: Amorphous LLTO

$Li_{3x}La_{2/3-x}TiO_3$ (LLTO) is another promising solid electrolyte and has higher bulk ionic conductivity ($\sim 10^{-3}$ S cm^{-1}), than that of LiPON ($\sim 10^{-6}$ S cm^{-1}), which is advantageous as well as negligible electronic conductivity and electrochemical stability. Like other solid electrolytes, since ceramic feature of LLTO is basically free from flammability, it is expected to be able to replace conventional organic-liquid electrolytes. Moreover, composition dependency of LLTO ionic conductivity was studied and plotted in Figure 1.13, which shows $Li_{0.36}La_{0.55}TiO_3$ has highest ionic conductivity at 1.1×10^{-4} S/cm.[62]
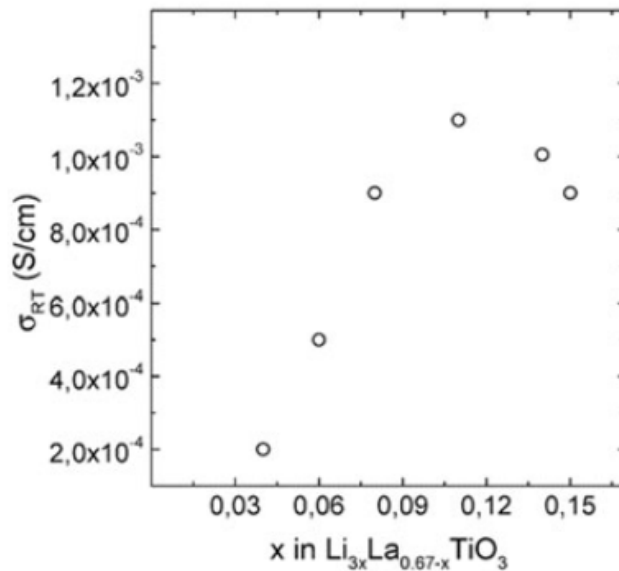
Figure 1.13 Ionic conductivity of $Li_{3x}La_{0.67-x}TiO_3$ as a function of Li composition x.

However, there are several things to be improved. One of the major challenges is low grain-boundary conductivity ($<\sim10^{-5}$ S cm^{-1}). Despite its high bulk ionic conductivity, low grain boundary conductivity impairs effective ionic conductivity to $\sim10^{-5}$ S/cm. To overcome this issue, various kinds of approaches have been tried: introducing silica ($\sim1\times10^{-4}$ S/cm)[11,63,64] and LLZO[65,66] (1.2×10^{-4} S/cm), doping Al (2.95×10^{-3} S/cm)[67] or other elements (e.g. Cr, Zr, Mn, V, Nb, Ta, W, and Mo), and so on[62]. Amorphous structure is inherently free from grain boundary, amorphization of LLTO can be another direction. Lee et al. from our group explored amorphous LLTO (a-LLTO) instead of crystalline LLTO[68], as well as other researchers employing PLD[69,70] and sputtering[71–76]. They fabricated a-LLTO with varying O$_2$ pressure and temperature conditions and maximized ionic conductivity of thin film LLTO. Ionic and electronic conductivity of LLTO thin films deposited at different temperatures is plotted in Figure 1.14. As shown in Figure 1.14, ionic conductivity has a maximum value at 400°C. Furthermore, selected area electron diffraction (SAED) of a-LLTO deposited at 600°C showed both amorphous diffuse ring and diffuse diffraction spots, which means LLTO begin to be crystallized at high temperature.
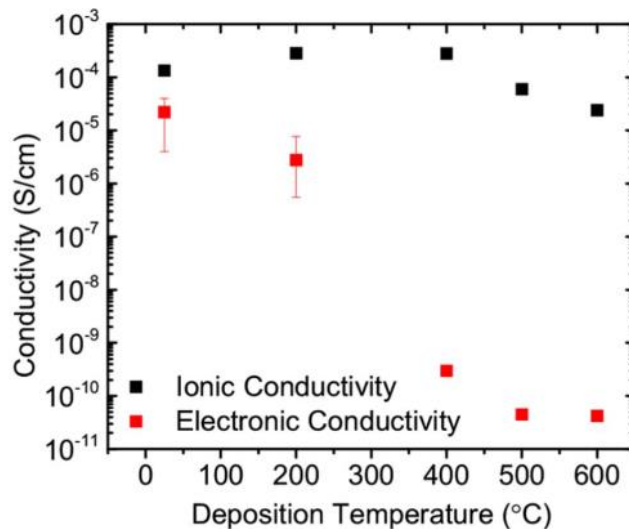
Figure 1.14 Ionic conductivity and electronic conductivity at various deposition temperatures[68].

17

Amorphous LLTO can solve another problem of LLTO, which is transition to conductive state of LLTO when in contact with Li metal. Crystalline LLTO has experienced reduction of Ti^{4+} to Ti^{3+} due to Li insertion from Li metal anode, turning LLTO into electric conductor[77,78]. This reaction is not desirable as an electrolyte material. On the contrary to crystalline LLTO, Zheng et al[79]. experimentally confirmed that amorphous LLTO pellets in contact with Li metal did not show electric conductor transition, which matched results from Ahn and Yoon[70]. For those reasons above, preparation conditions of LLTO should be sought to maximize its ionic conductivity and minimize electronic conductivity.

1.6 Application of Battery Materials to Resistive Switching Device Materials

1.6.1 Resistive Switching (RS) Device

To date, transistors have been developed over 50 years to achieve fast, low-cost, portable, high-performance computing, which are essential for our daily life. Currently the demand for such computing technology is further growing due to internet of things (IoT), which connects all the tiny sensors incorporated in home appliances into internet and manage them comprehensively, and autonomous driving, which needs high-speed image processing to cope with environment changing every second. To meet such demands, the transistor technologies grow over years, following "Moore's law", predicting the number of transistors on an integrated circuit chip doubles approximately every two years[80]. Figure 1.15 is a plot of number of transistors per chip per year[81,82], demonstrating that actual technology development follows the Moore's law. The data in Figure 1.15 were collected up to 2015, and the latest chips, for example, Apple M2 chip and IBM Telum chip have 20 billion transistors[83] and 22.5 billion transistors per chip[84], respectively, which confirms that the transistors is still growing along with Moore's law. However, this growth might be approaching some limits: (i) size, (ii) cost, and (iii) speed[81]. Increasing the number of transistors

on chip means the size of a transistor becomes smaller and smaller. However, if the size is close to nanoscale, quantum effect is not negligible and electron flow cannot be controlled. Also, as Figure 1.15 right axis depicts, such nanoscale design increases both verification and design cost exponentially due to the difficulty of engineering. Moreover, current von Neumann architecture, where data stored in memory and transported to the calculation engine, limits the computation speed. For those reasons, new functional material needs to be explored to replace conventional silicon-based transistor for future computing devices.
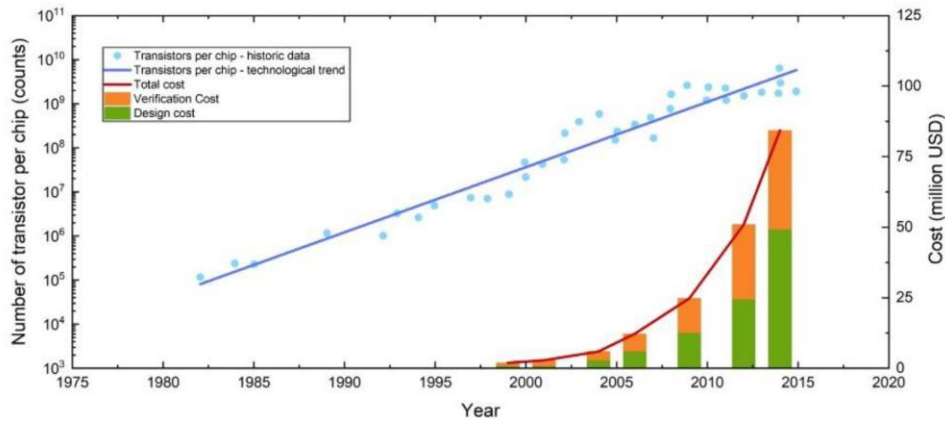
Figure 1.15 Number of transistors per chip vs. year (left axis) with cost vs. year (right axis)[81,82].

Resistive switching (RS) device is one of the potential candidates for future computing technology. RS devices are memory devices taking advantage of metal-insulator transition material and record data by different conductance (i.e. resistance) state switched by external stimuli such as voltage[85–87]. There are several types of mechanisms to switch resistance inside materials and are summarized in Figure 1.16[85]. Figure 1.16 (a) describe phase change materials that utilize phase change between crystalline and amorphous induced by temperature change due to joule heat[88–90]. Figure 1.16 (b) shows metal-insulator transition in Mott-insulator materials[91–93]. Figure 1.16 (c) exhibits conductive filament formation by conductive bridge, where metal atoms migrate from one side to the other and bridge both sides, reducing overall resistance[94,95]. Figure

19

1.16 (d) is used in spin-transfer-torque magnetic random-access memory (STT-MRAM), in which insulative tunnel barrier layer is sandwiched by soft magnet (free spin layer) and pinned magnet (fixed spin layer)[96–101]. The tunnelling magnetoresistance effect plays a role to switch the device into ON by changing magnetization orientations into parallel in soft magnet side, leading to changing probability of electrons through the insulative layer. In Figure 1.16 (e), oxygen vacancy migrates and induce phase transition of the insulator material, forming conductive filament with oxygen-vacant composition[102–104]. Basic mechanism is similar to Figure 1.16 (b) and (c) but, in this case, minor composition of the dielectric materials changes. In the case of interface-type (e), oxygen vacancies stay at the interface between metal electrode and the oxide intermediate layers, reducing activation barrier electrons and inducing current flow[87,105].

Our study, which seeks the application of battery materials to resistive switching devices, focus more on metal oxide materials forming oxygen vacancy filament during resistance change (Figure 1.16 (e)). In the battery community, those are commonly used as cathode, anode, and electrolyte materials. Therefore, we can transfer knowledge about those oxides obtained from battery field to the RS device study, especially about composition, chemistry, crystallinity, and ion behavior.
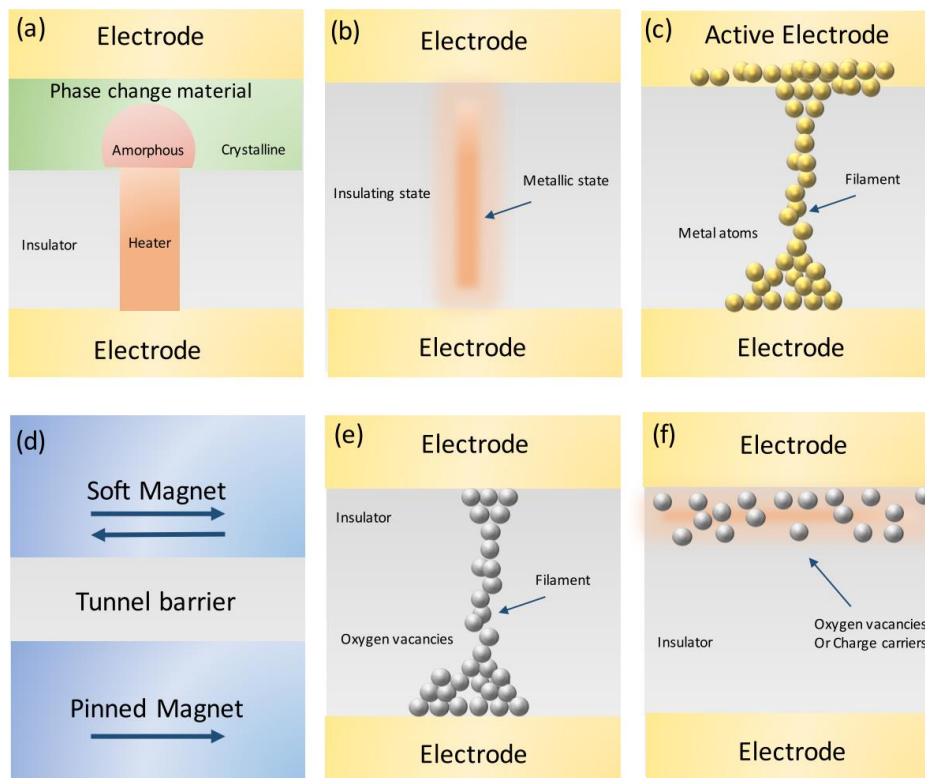
Figure 1.16 Different switching mechanisms[85]: (a) phase change materials, (b) metal-insulator transition by Mott-insulator, (c) conductive bridge random access memory, (d) spin transfer torque magnetic random-access memory, and oxygen vacancy-induced resistive switching with (e) filament growth and (f) interface-type change.

1.6.2 Potential of Li ion Battery Materials to RS Devices

Materials commonly used for batteries have great potential to be applied to resistive switching[81]. Fabrication methods and phase diagram depending on their composition have been already well developed, especially for materials that were already commercialized such as $LiCoO_2$. Furthermore, several materials demonstrated conductivity state changes from high to low upon their composition changes, which meets requirement as a resistive switching device. For example, $LiCoO_2$ (LCO), which is the most common layered cathode material, is famous for showing metal-insulator transition upon Li insertion (lithiation) to CoO_2 flamework[106]. As Li composition in its stoichiometry increases, electric conductivity of LCO drops from 10^{+2} to 10^{-4} S/cm. RS device application of LCO was studied by Moradpour et al.[107] and Fuller et al.[108], and Fuller et al.

constructed three-terminal device (source, drain, and gate) and was able to operate "write" and "read" as a device.

Spinel $Li_4Ti_5O_{12}$ (LTO), which is metal oxide anode material and famous for its "zero-strain" during lithiation[109–111] can be another candidate. Similar to LCO cathode, Young et al. have studied dependency of its electronic conductivity on its lithiation state, confirming that there is huge jump of conductivity by 7 orders[112] (Figure 1.17 (b)). This is large enough to cause distinguishable conductance change upon operation as a switching device. Furthermore, the conductivity jump occurs at the very early stage of lithiation (~5%), which suggests only tiny amount of Li migration are needed and can save huge amount of power consumption as a device. Gonzalez-Rosillo et al. have researched potential of LTO, aiming at the application to synaptic transistors[113]. They found that two-terminal system with LTO has fast resistive switching feature with zero-strain. Besides, TiO_x-based switching device has been developed and evaluated by Nguyen et al[114], while the device does not utilize spinel LTO. They have developed a three-terminal system with TiO_2 and LiPON as a channel and electrolyte insulator layer, respectively, where TiO_2 is chemically lithiated and works as a lithium source of Li_xTiO_2. While the composition and crystalline phase of Li_xTiO_2 are different from that of spinel LTO, they provided potential that titanium oxide-based device can operate as a RS device. Details about this device and future works will also be discussed in Chapter 5.

Last but not least, LLTO can be a potential candidate as a future RS device, which is discussed as a one of the main focuses in Chapter 4 in this dissertation. As mentioned in the previous section, LLTO thin film optimization was carried out by Lee et al. from our group[68]. In their optimization, they found that O_2 deposition pressure affects electronic conductivity of LLTO (Figure 1.17). This is attributed to Ti reduction from 4+ to 3+ due to the formation of O-vacancy

state inside LLTO. Whereas, upon the development of solid electrolyte, this conductivity variation is not desired symptom, it is useful phenomena for resistive switching device. As explained in the previous section, oxygen vacancy can migrate under electrical bias and may form conductive filament with O-vacant LLTO. Moreover, there is another advantage of LLTO. Since LLTO is originally developed as an electrolyte material, which requires low electric conductivity as a electrically separating layer between cathode and anode, it can minimize leakage current when it is incorporated in the circuit as a part of device.

Considering characteristics and advantages of materials mentioned above, more battery materials might have should be further investigated as both battery and RS materials. It is possible that some physical properties that is not suitable as a battery material can be advantageous over conventional metal oxide dielectric materials for RS devices.
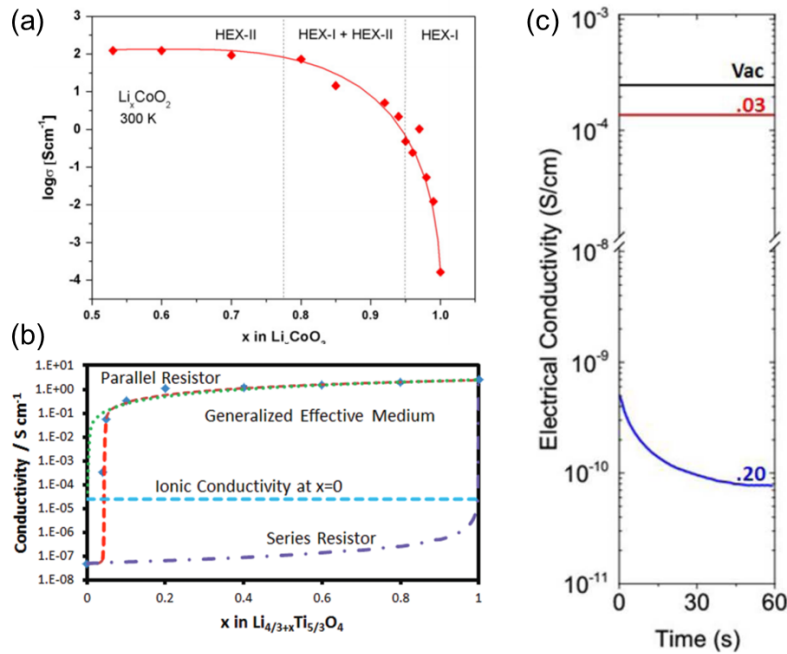
Figure 1.17 Electric conductivity of various battery materials. (a) Li_xCoO_2 conductivity vs. Li composition x[106], (b) $Li_{4/3+x}Ti_{5/3}O_4$ conductivity vs. Li composition x[112], and (c) $Li_{0.5}La_{0.5}TiO_3$ conductivity depending on O_2 deposition pressure[68].

Chapter 2 Methodologies

2.1 Thin-Film Fabrication by Various Physical Vapor Deposition (PVD) Techniques

In this chapter, I explain various physical vapor deposition techniques to fabricate thin-film batteries/devices. Other than PVD, there are variety of methods to make thin-film such as chemical vapor deposition (CVD), sol-gel deposition, and electrochemical plating. Among those techniques, considering thin-film batteries/devices that require multiple layers stacking on top of each other, PVD method might be suitable since it does not need any extra chemicals in liquid form and enables series deposition. From various PVD methods, here, I illustrate thermal evaporation, sputtering, and pulsed laser deposition, which are employed in my research.

2.1.1 Thermal Evaporation

Thermal evaporation utilizes joule heat to vaporize target (source) materials and the vaporized particles travel through vacuum and reach substrate, resulting in forming thin film on the substrate. Before and during film deposition, the chamber is pumped down to high vacuum at around 10^{-8} mbar to minimize impurity into deposited films and to maximize mean-free path of evaporated particles. The advantage of this method, compared to sputtering deposition, is low kinetic energy of evaporated particles (at 1200 K, $E = 0.1\ eV$ [115]), which enables to avoid bombardment and incorporation of evaporated particles into substrates. Besides, due to its simple system architecture, the evaporation chamber can be installed into glovebox. This helps us handle air-sensitive materials such as lithium and test fabricated film in inert conditions. On the contrary to such advantages, the drawback of this method is difficulty in controlling film stoichiometry, which limits source materials[115]. The choice of source elements is also limited to ability of the power source in equipment and vapor pressure of elements (Figure 2.1 (b)). Figure 2.1 (b) shows that lithium is relatively high vapor pressure, and its film can be made by thermal evaporation,

ensuring uniform deposition on top of solid electrolytes with intimate contact at the atomic level. The choice of crucible or boat, which works as a tray of source elements and as a resistive heater, should be made carefully as well to prevent contamination of the film from the vaporized boat material. On the left side of Figure 2.1 (b), tungsten (W) shows the lowest vapor pressure. This explains why tungsten is used for a variety of source elements. Other than tungsten, graphite, Al_2O_3, Mo, quartz, etc. are used as a boat/crucible[115].

In our study, thermal evaporation is used to deposit Li metal anode and Cu current collector on LNMO/LiPON/Li cell.
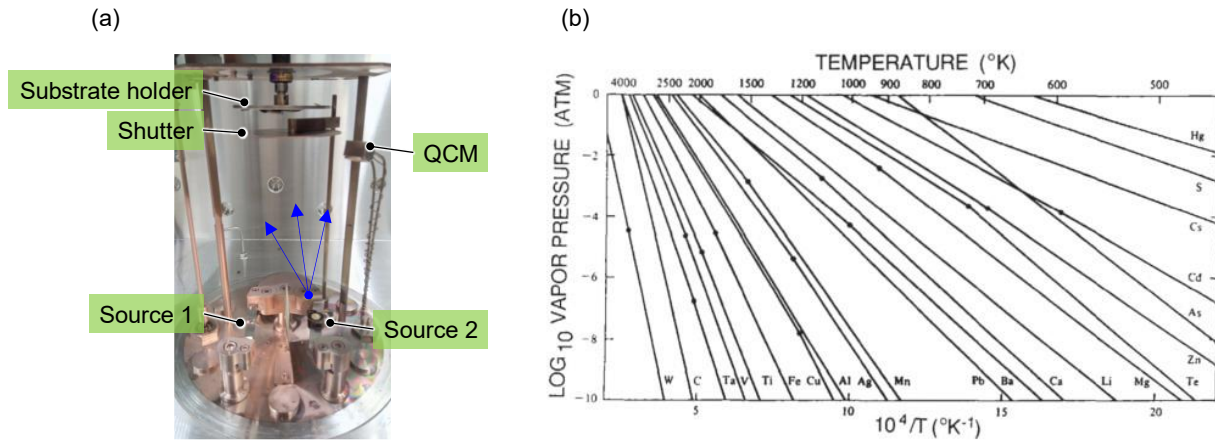
Figure 2.1 Thermal evaporation technique. (a) photograph of thermal evaporator (blue arrow represents evaporation plume). (b) Vapor pressure of various elements[116].

2.1.2 Sputtering

Sputtering method is another way of fabricating thin films. Instead of joule heat in evaporation, sputtering takes advantage of ionized gas to vaporize target materials. In the sputtering chamber, the electric field made by supplied power ionizes gas (Ar, N_2, etc.) and the gas particles are attracted to target pellet set on the negatively biased electrode, resulting in collision and vaporizing target materials with kinetic energy transferred from the gas. Vaporized materials travel through the vacuum chamber to a substrate, and forms thin film on the surface (see

Figure 2.2 (a)). In general, sputtering technique is classified into two: (1) DC (direct current) and

(2) RF (radio frequency). Unlike evaporation, sputtering has more choice of target materials and

can achieve various kinds of films as exemplified in Table 2.1 by properly selecting methods above.

Table 2.1 Examples of available sputtering targets[115]

Type	Materials
Metals	Al, Cr, Ge, Au, Fe, Ni, Pd, Pt, Ag, Ta, W
Alloys	Al-Cu, Al-Si, Al-Cu-Si, Co-Fe, Co-Ni, Fe-Tb, Fe-Ni, Co-Ni-Cr, Ni-Cr, Ti-W, Gd-Co
Oxides	Al_2O_3, $BaTiO_3$, $PbTiO_3$, CeO_2, In_2O_3-SnO_2, $LiNbO_3$, SiO_2, SiO, Ta_2O_5, TiO_2, ZrO_2, HfO_2, MgO
Fluorides	CaF_2, CeF_3, MgF_2, ThF_4, Na_3AlF_6
Borides	TiB_2, ZrB_2, LaB_6
Carbides	SiC, TiC, TaC, WC
Nitrides	Si_3N_4, TaN, TiN
Silicides	$MoSi_2$, $TaSi_2$, $TiSi_2$, WSi_2
Sulfides	CdS, MoS_2, TaS_2, ZnS
Selenides, Tellurides	CdSe, PbSe, CdTe, ZnSe, PbTe, MoTe, MoSe

Basic principle of sputtering explained above is mostly about DC sputtering, where ionized

gas particles hit target surface and knock off the target materials. However, this is applicable only

when the target is metal (conductive). In the case of an insulative target material, charged ions

accumulate on the electrode surface as the sputtering goes on, leading to decrease in deposition

efficiency. Therefore, the process to clean up charges is needed during deposition, i.e., RF

sputtering.

RF sputtering, by applying AC current to target, a thin film of its material will be deposited.

When the target side is negatively charged (negative cycle), ionized gas particles such as argon are

attracted to the target and bombard its surface (Figure 2.2 (a)). Then, atoms of target material

obtain kinetic energy and fly to the substrate fixed on the opposite side to the target. On the positive

cycle, when the target side is positively charged, positively charged ions collected on the target

26

surface are cleaned (Figure 2.2 (b)). By repeating these processes, thin film is obtained. For this mechanism, RF sputtering expands options of targets to insulative/dielectric materials. Furthermore, choice of gas species mixed with inert Ar gas can provide further variation in thin films, such as oxides, fluorides, or nitrides (Table 2.1), which is called as reactive sputtering. Common compounds that can be made by reactive sputtering are summarized in Table 2.2.[115]
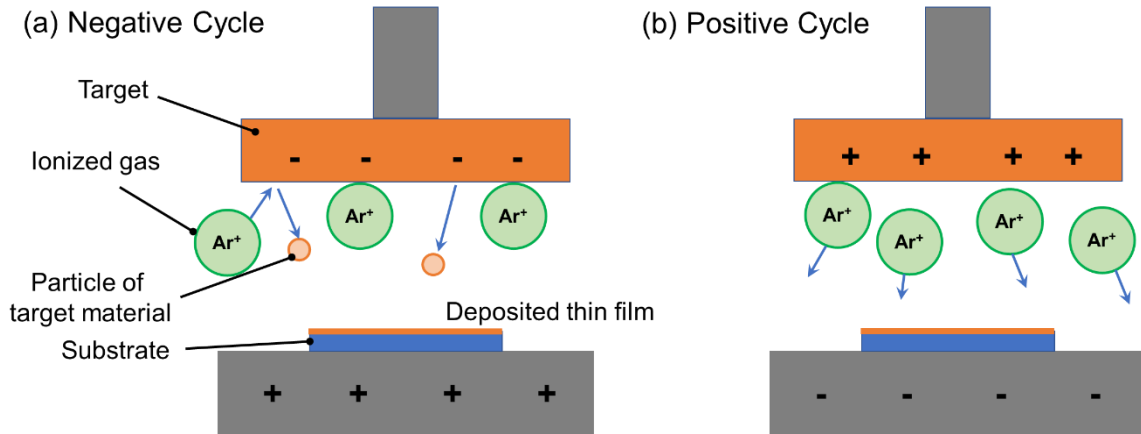
Figure 2.2 Schematic of the RF sputtering process at (a) negative cycle and (b) positive cycle. Since a target is an insulator, charged gas ions stay on the target surface after a certain amount of negative cycle time, which prevents other ions from bombarding the target and results in stopping sputtering.

With using these sputtering techniques, numerous types of thin films related to lithium-ion batteries have been optimized and prepared as well as coating or semiconductor fields. Various sputtering methods explained above have enabled not only simple elements used in an anode, such as Li and Si, but also complicated lithium metal oxide compounds. As a cathode material, deposition condition of $LiCoO_2$[117], $LiFePO_4$[118,119], spinel $LiMn_2O_4$[120,121], $LiNi_{0.5}Mn_{1.5}O_4$[122,123] and Li-Ni-Mn-Co-O[124–127] (composition varies) have been investigated and those films are utilized for both fundamental study and device application. Solid-state electrolytes also have been established by RF sputtering, such as lithium phosphorus oxynitride (LiPON)[23,45], Li-La-Ti-O[71–73,76], and Li-La-Zr-O[128]. In our study, I employ RF sputtering to fabricate LiPON film, which conformally covers LNMO surface and works as a solid-state electrolyte.

Some of films can be fabricated by both sputtering and pulsed laser deposition (PLD). However, sputtering has the following advantages over PLD (About PLD, it is explained in the next sub-chapter.) The sputtering system consists of simple parts (power supply, vacuum chamber, and gas flow controller), while PLD must need an excimer laser with specially mixed gas (e.g., Ne, F, Kr). Therefore, it has great potential to reduce production costs. Moreover, sputtering can achieve larger area deposition by using large size sputtering target whereas spot size in PLD is limited by focused laser pulse, which gives smaller plume of vaporized target materials[129]. For those reasons, although PLD can provide better quality films, sputtering is still a mainstream of thin film fabrication process.

Table 2.2 Example of gas species and products used in reactive sputtering.[115]

Compounds	Gas	Products
Oxides	Oxygen	Al_2O_3, In_2O_3, SnO_2, SiO_2, Ta_2O_5
Nitrides	Nitrogen	TaN, TiN, AlN, Si_3N_4
Carbides	Methane, Acetylene, Propane	SiC, TiC, WC
Sulfides	H_2S	CdS, CuS, ZnS

2.1.3 Pulsed Laser Deposition (PLD)

Pulsed laser deposition is a strong technique to fabricate thin films, where film stoichiometry is well preserved from target materials. This is a main advantage over sputtering method and enables to fabricate multication complex oxides, e.g. superconductive materials or battery cathode materials. In the PLD procedure, the laser beam goes into a chamber and hits a target material, and the evaporated target material is deposited on the substrate facing the target[130]. Figure 2.3 demonstrates pulsed laser deposition system that is used in our study. As a pulsed laser, ultraviolet excimer lasers are typically employed since it is strongly absorbed by a small target material. Depending on the material of a thin film, gas that is introduced into the chamber is

selected properly. For example, oxygen gas is generally chosen to compensate or control oxygen composition inside produced oxide thin films. Controlling substrate heating temperature and selecting proper substrate can tune crystallinity of deposited thin films. For example, Konishi et al. fabricated epitaxial $LiNi_{0.5}Mn_{1.5}O_4$ thin films with lattice orientations at (111), (110), and (100) by growing those films on single-crystal $SrTiO_3$ (111), (110) and (100)[42,43].

By using multiple targets, it is possible to make thin film battery only by PLD method. Kuwata, et al., for example, fabricated two thin film ion batteries and studied their performance and morphology; SnO/Li-V-Si-O (LVSO)/$LiCoO_2$ and SnO/LVSO/$LiMn_2O_4$, where SnO works as an anode, solid LVSO as an electrolyte, and layered $LiCoO_2$ and spinel $LiMn_2O_4$ as a cathode[131].

Some films can be prepared by PLD and (RF) sputtering. However, the film quality and its physical properties like lithium ionic conductivities demonstrate differently, which is exemplified by lithium lanthanum titanate (LLTO). Lee et al from our group optimized LLTO thin film and its (lithium) ion conductivity showed around 3×10^{-4} S/cm, which is close to the one in bulk LLTO[79,132,133] and the highest value among films made by PLD[69,70]. On the contrary to the PLD-made LLTO films, LLTO films made by RF sputtering demonstrates 10^{-5} S/cm orders of magnitude or lower as an ionic conductivity[71–73,76], where 5.32×10^{-5} S/cm is the maximum value achieved by Song et al[73]. This mismatch might be attributed to imperfect transfer of the target compositions by RF sputtering, showing advantages of PLD method.

In our study, PLD is employed to make LNMO and LLTO thin films. Detailed fabrication conditions are described in Chapter 3 and Chapter 4, respectively.
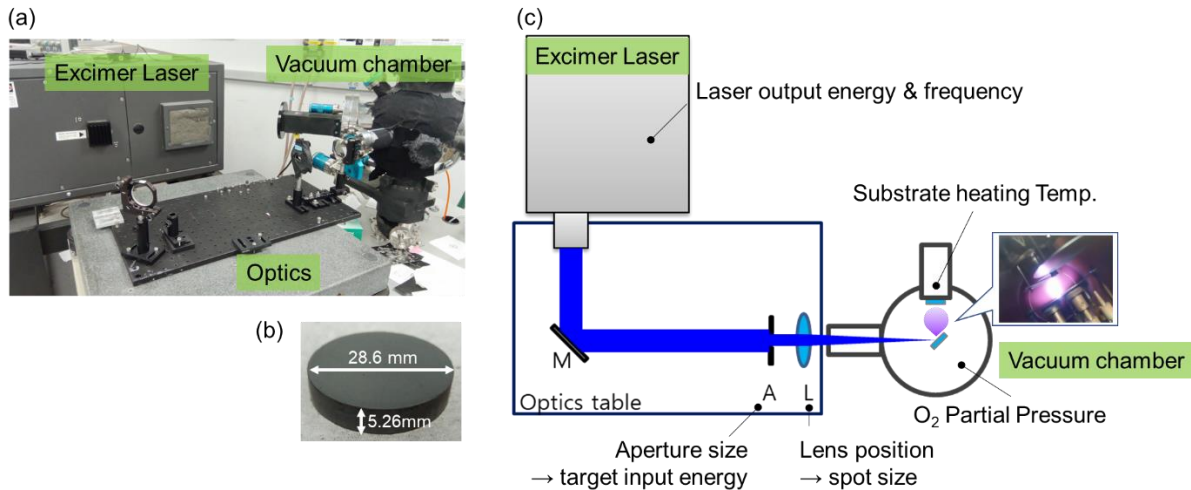
Figure 2.3 Pulsed laser deposition system and target pellet. Photograph of (a) PLD system used in our study and (b) home-made LNMO target. (c) Schematic of PLD system and parameters that affect deposited films' quality.

2.2 Advanced Characterization

2.2.1 Neutron Depth Profiling (NDP)

Neutron depth profiling is a strong technique to detect lithium atoms directly and quantitatively. Plenty of neutron techniques, such as neutron diffraction, neutron reflectometry, and neutron scattering, have been used and become popular in battery field so far, where neutrons and atoms in a sample interact as an elastic or inelastic scattering (Figure 2.4). On the contrary, NDP take advantage of nuclear reaction (i.e., absorption) of neutrons with atoms, where number of electrons and neutrons changes before and after the reaction. This has not often been used for battery studies and is still under development. Hence, in this chapter, I illustrate basic principles of NDP and its application.
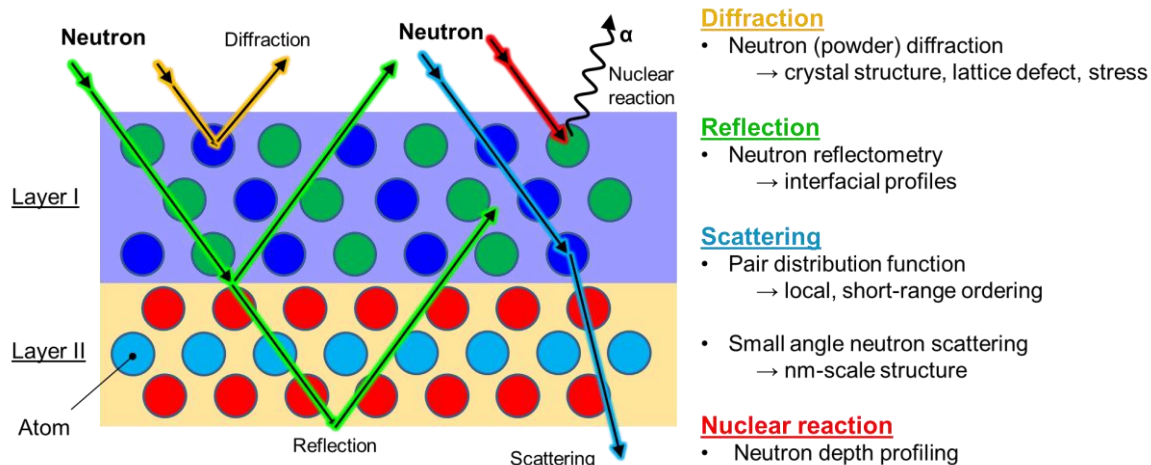
Figure 2.4 Examples of various characterization techniques using neutron.

Neutron vs. X-ray

As the investigation of battery goes on, direct observation of carrier ions in a battery, i.e., lithium atom/ion, becomes important. X-ray has historically been used for materials characterization to observe structure (short- and long-range ordering), morphology, and chemistry. However, these technics are mostly indirect observation, e.g., through crystal structure with transition metal cations. This is because it is intrinsically difficult to directly observe lithium ion via x-ray due to its small x-ray cross-sections[134]. X-ray is electromagnetic wave with 0.03 to 3 nm in wavelength, and, thus, its interaction with atoms is proportionally stronger, as Z number increases (Figure 2.5 top). In contrast, neutron cross section does not show such tendency on atoms, and this is why neutron is suitable for tracking light elements like hydrogen (deuterium) and lithium (Figure 2.5 bottom).
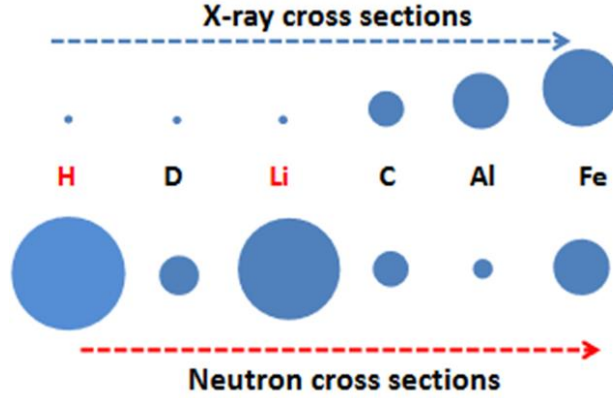
Figure 2.5 Schematic image of x-ray (top) and neutron cross sections (bottom)[134].

Fundamentals and workflow

Here, in this subchapter, fundamental mechanism, experimental setup, and common workflow of analysis in NDP are explained. In NDP experiments, as Figure 2.6 (a), a sample is set inside vacuum chamber and neutron beam shines from top of the sample[135]. Inside the sample, one neutron reacts with one ^{6}Li atom and generates ^{4}He^{2+} and ^{3}H$^+$ atoms in the following equation:

$$^6Li + n \rightarrow\ ^4He^{2+} +\ ^3H^+$$
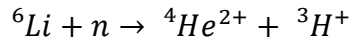
^{4}He^{2+} and ^{3}H$^+$ are generally called alpha and triton particles, respectively. Generated ^{3}H$^+$ are captured by the Si detector, giving intensity and count as shown in Figure 2.6 (b). Based on this nuclear reaction, NDP allows us to measure Li amount quantitatively by counting charged. Then raw data plots (signal counts vs. channel) will be converted to the final output, that is, Li concentration vs. depth plot. From the reaction formula above, the number of Li atoms can be estimated from triton signals count. Areal concentration of lithium is calculated from the following equation with using boron standard sample:

$$D_{Li}\ [atoms/cm^2] = \frac{D_{10B}\ [atoms/cm^2] \times \sigma_{10B}\ [barn]}{A_{6Li} \times C_{10B}\ [counts/sec] \times \sigma_{6Li}\ [barn]} \times C_{6Li}\ [counts/sec]$$

Here, D_i, σ_i, C_i, and A_i are areal concentrations, reaction cross sections, signal count rates, and natural abundance of each element ($i = {}^{6}Li, {}^{10}B$), respectively. In this equation, σ_i and A_{6Li} are physical constant ($\sigma_{10B} = 3842\ barn$, $\sigma_{6Li} = 939\ barn$, and $A_{6Li}=0.075$), and D_{10B} and C_{10B} are known or measurable values. Thus, the signal rate of lithium can be simply converted to lithium areal concentration[136].

Inside a detector, particles with different kinetic energy are separately detected in different channels, and, thus, the channels and particle kinetic energies have one-by-one correlation. Besides, particle kinetic energies are further correlated with depth of Li in the samples. When the nuclear reaction happens deep inside the sample, the generated ${}^{3}H^{+}$ particles are required to travel though to its surface. On the way to surface, particles lose their kinetic energy by interacting with atoms (electron and nuclei) and lose a part of the energy. Therefore, the deeper the triton particles are generated, the smaller their kinetic energy is, as exemplified in Figure 2.6 (d).
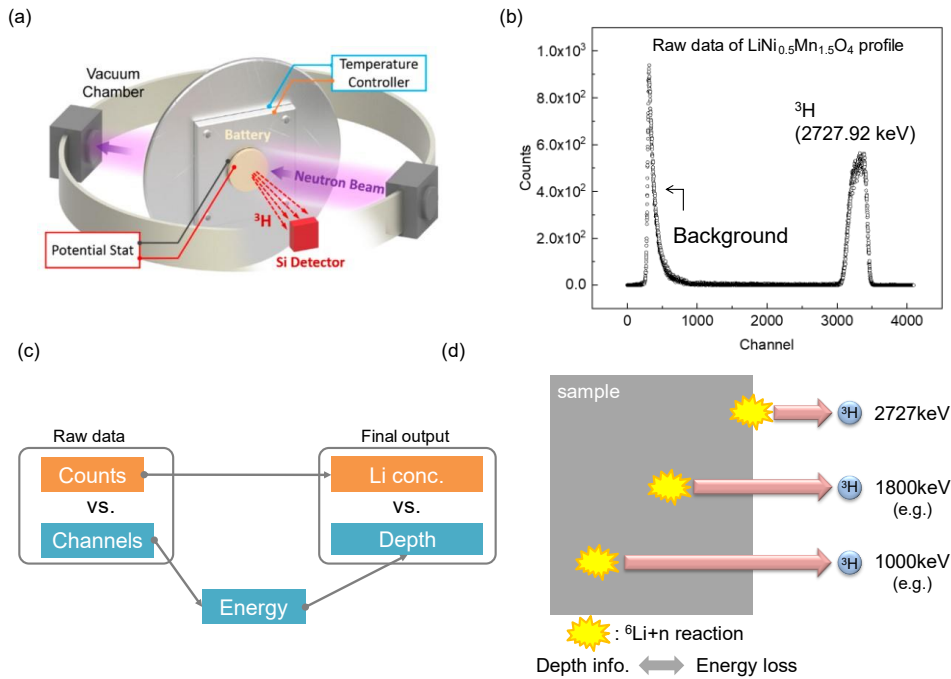
Figure 2.6 NDP fundamentals and workflow. (a) experimental setup of NDP inside vacuum chamber[135]. (b) example of raw NDP spectra from $LiNi_{0.5}Mn_{1.5}O_4$. Here 4He is filtered out by applying Kapton tape on sample surface. (c) common workflow in NDP from raw data to depth profile. (d) schematic illustrating the correlation between energy loss and depth of the sample.

Advantages, Disadvantages, and Limitations

As shown in the previous subchapter, quantitative, non-destructive characterization of lithium in sample's depth is one of the advantages of NDP over other characterization methods for Li detection like Time-of-Flight Secondary Ion Mass Spectrometry (ToF-SIMS) and X-ray Photoelectron Spectroscopy (XPS) depth profiling. NDP is not only applicable to Li but also to He, B, or N elements due to their large enough cross-sections, which are listed in Table 2.3[137]. Furthermore, NDP is compatible with *in-situ* or *operando* measurement by combining with potentiostat and/or temperature controller (Figure 2.6 (a)). On the contrary to those advantages, depth resolution of NDP is limited to about 30 nm, which is attributed to energy resolution of the detector and stopping power of the materials. Besides, NDP profiles are affected by sample surface flatness and/or smoothness. The obtained depth profiles are average information from the area neutron shines, and, therefore, signals at the rough interfaces of two different layers tend to be mixed and profiles look smeared. To obtain a good enough signal/noise ratio, isotope of interest should also be sufficient in concentration.

Table 2.3 Major elements detectable in NDP measurements[137]

Elements	Reaction	Target Cross Section (barns)
He	^{3}He(n,p)^{3}H	5333
Li	^{6}Li(n,α)^{3}H	940
B	^{10}B(n,α)^{7}Li	3837
N	^{14}N(n,p)^{14}C	1.83

There are some limitations in NDP upon measurement. Unlike x-ray, neutron beam cannot be focused so the minimum lateral area is limited to around 3 mm in diameter. The generated triton particles lose their kinetic energy while they go through the sample materials due to their coulombic interaction. Hence, the depth limit of NDP is determined by the distance that the triton particles can fly to the detector without losing all the original kinetic energy, i.e., 2727 keV. This

value strongly depends on materials, and the lighter the elements are, the longer the triton can fly, meaning deeper elements can be detected. Figure 2.7 represents penetration depth of triton particles against materials used in batteries[138], which is calculated by Monte-Carlo simulation in SRIM[139]. This demonstrates that tritons in materials consisting of light elements such as Li metal and Li_3PO_4 can travel longer while the penetration depth is short in heavy metals such as Pt and Cu.
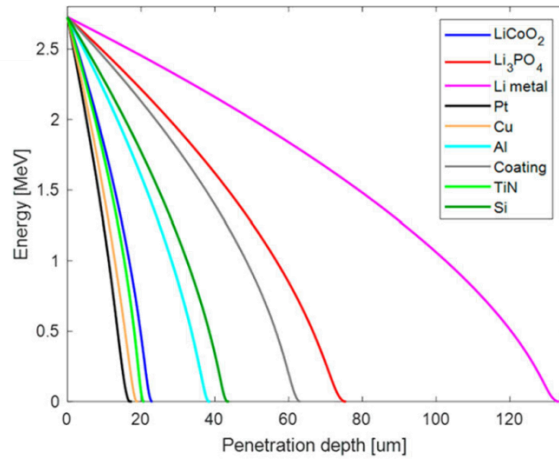
Figure 2.7 Simulated energy loss of charged triton particles against typical battery materials.[138]

In the reaction, neutron and lithium generate alpha ($^4He^{2+}$) and triton ($^3H^+$) particles. In general, alpha particles are filtered out by Kapton tape on surface, to avoid merging two signals, and only triton particles are used in NDP measurement. This is because the triton particles have more kinetic energy when generated, enabling us to seek deeper in samples (Figure 2.8 (a))[140]. However, it is potentially possible to improve NDP measurement by properly selecting particles. As mentioned above, compared to triton particles, alpha particles have shorter traveling path due to its original kinetic energy when two particles travel in the same material (Figure 2.8 (b)[138]). Besides, alpha particles are charged as divalent while tritons are charged as monovalent. This leads to higher stopping power against alpha particles due to coulombic interaction, which can be seen as steeper slope in the dash lines in Figure 2.8 (b). For those reasons, triton particles are suitable

to investigate deep inside of the sample. On the other hand, alpha particles are preferred in terms of depth resolution. As can be seen in Figure 2.8 (b), alpha particles have smaller depth range for same energy resolution, which is independent from choice of particles. Therefore, this exhibits alpha particles have better depth resolution than triton particles. In Figure 2.8 (c), two characteristics, depth, and resolution, for each particle are summarized.

In this chapter, I have explained basic principles and working mechanisms of NDP. In our study, NDP is used to explore Li distribution at LNMO/LiPON interface and further experimental aspect of NDP is explained in the 0.
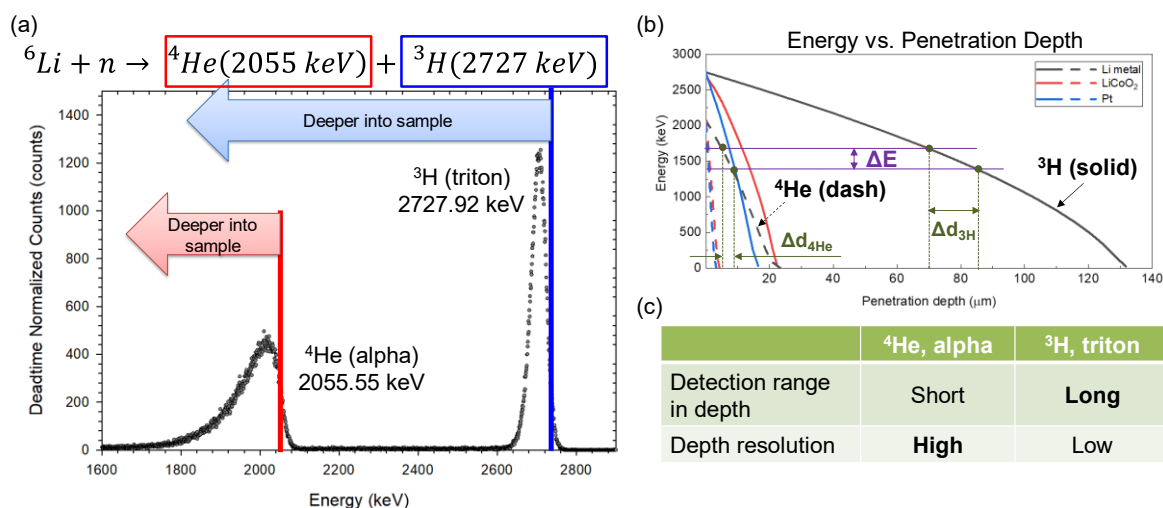
Figure 2.8 Comparison of two particles that can be used in NDP measurement. (a) spectra of alpha and triton particles[140], (b) energy vs. penetration depth (solid line: triton, and dash line: alpha) in some battery materials. (Data extracted from Danilov et al.[138]) (c) Pros and cons for triton and alpha particles.

2.2.2 Focused Ion Beam and *in-situ* Biasing Experiment

Nowadays, focused ion beam (FIB) is a necessary tool to study battery materials. The major use of the FIB is to investigate thickness of electrode and electrolyte particles, and morphologies in cross-sectional direction. In particular, FIB is suitable to explore thin film samples, since their total thickness is typically within a few microns. Furthermore, FIB can connect material characterization to advanced tools and techniques. For example, FIB enables us to prepare lamella

samples for transmission electron microscope (TEM) by milling bulk materials via ion beam and carrying the milled lamella to a TEM grid. Also, FIB has the potential to achieve in-situ biasing experiment by applying current or voltage onto a probe and a stage. Here in this subchapter, I describe general instrumentation of FIB first and then illustrate in-situ biasing experiment.

Focused-Ion Beam

FIB columns are generally equipped with scanning electron microscopy (SEM), transmission electron microscopy (TEM), Auger electron spectroscopy (AES), or secondary ion mass spectrometry (SIMS). Among them, the most common one is FIB/SEM as a dual beam system, where electron beam column is set vertically against a sample stage and ion beam column is set at some angles[141]. In such a system, electron beam works to image a sample surface without damaging it while ion beam works to sputter or mill materials on surface. In addition, the electron beam can also deposit metals, enabling low energy deposition. This can minimize sputtering damage on surface, compared to the deposition by the ion beam.

Whereas various ion source species are available, e.g. Al, Au, B, Be, Cu, Ga, Ge, Fr, In, Li, P, Pb, and Si, Ga is most widely selected due to its low melting temperature (30°C), low volatility and low vapor pressure[142]. Figure 2.9 (a) depict similarities and differences between electron beam and ion beam. In the case of the ion beam, electrostatic lenses are used while magnetic lenses are used for the electron beam. This is because ion is heavier and slower, resulting in lower Lorentz force affecting on ions[143]. Detailed schematics in Figure 2.9 (b) shows Ga ion source, where the minimum beam size is determined as ~5 nm and, thus, defines a resolution of patterns made by the ion beam. In FIB milling process, an ion collision removes one to five atoms depending on the substrate and applied energies. In addition to that, similarly to e-beam imaging, (ion-induced) secondary electrons are ejected because of the ion collision to sample materials,

37

which can be used for ion beam imaging but also potentially induce chemical reaction between ion beam and target materials. The milling feature varies by elemental mass consisting of the sample, angle of the ion beam, and crystal structure, which also affects ion beam imaging. Figure 2.10 (a) and (b) describes that different crystal structure gives different ion milling pathways, where Ga ions in (b) has more probability to collide with sample atoms and more electrons are ejected. Between heavy atoms and light atoms, Ga ion pathway and ejected secondary electrons contrast are also different due to atomic mass and the number of electrons (Figure 2.10).
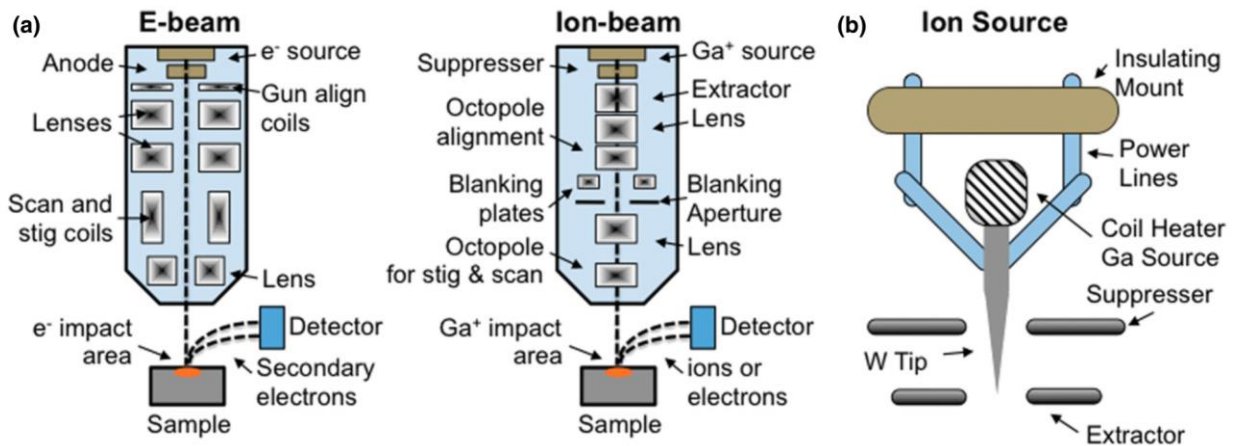
Figure 2.9 Schematic illustration of FIB/SEM systems. (a) Comparison of e-beam and ion-beam and (b) detailed image of Ga ion source.

As well as injected Ga ions affected by sample feature, other factors, such as Ga incorporation and redeposition of sputtered materials, should be considered when FIB processing, especially cross-section milling and TEM sample preparation. These potentially trigger inefficient milling rate and damage and/or contamination on TEM samples. First, redeposition of sputtered materials causes a decrease in milling rate. This is also a reason why perfectly vertical cross-section cannot be made. To prevent such redeposition, second milling with lower ion energy and with different incident angles are needed. Second, sample contamination is given by Ga ion incorporation. After the ions are injected and mill sample surface, Ga ions stay on surface and

cause Ga incorporation. Volkert and Minor estimated that 1 at.% to 50 at.% of Ga are expected to remain near sample surface[143]. Not only Ga implantation, which can be regarded as "chemical" contamination, but "physical" damage is also given by ion beam injection. Mayer et al. claimed that ion beam injection to sample materials cause amorphization, in semiconductor materials, and defect formation, phase formation, or atomic displacement in some metals[144]. This may cause misinterpretation especially when microstructure of the specimen materials is investigated. As discussed above so far, in summary, FIB is a stronger technique than any other in terms of engineering and manipulating micro- or nano-scale samples for their characterization, guiding us to further understanding in TEM or other nano-, atomic-scale characterization. However, drawbacks including contamination and damage due to the ion beam injection needs to be taken into account when its operation.
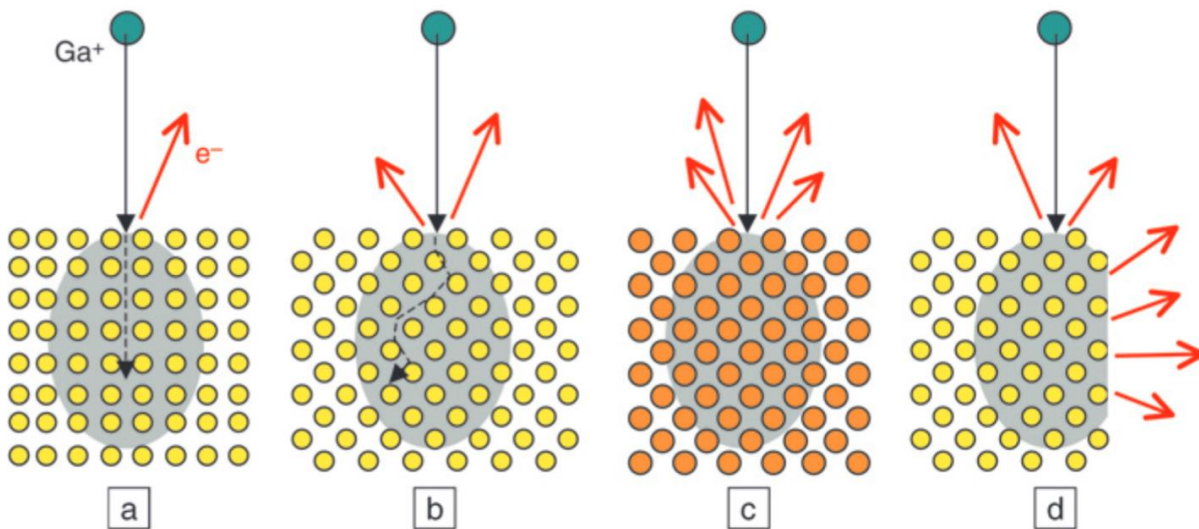
Figure 2.10 Various factors influencing on 30 keV Ga+ collision and ion-induced secondary electron (ISE) generation. (a) and (b) compare difference in crystal orientation, affecting milling ion pathway and amount of emitted ISE. Orange-colored atoms in (c) represent heavier atomic mass than ones in (a) and (b), where heavier atoms in (c) give more secondary electron. (d) Different surface geometry also gives different contrast in ion beam imaging[143].

In-situ biasing experiment in FIB/SEM

Currently FIB/SEM system is commonly used in the battery field to investigate cross-sectional morphology of samples and to fabricate lamellas for further microstructure study in TEM. Furthermore, coupling electrical feedthrough and a needle probe with the system, it can enable in-situ biasing experiments without air exposure. Simple schematic in Figure 2.11 (a) illustrates electrical connections. The positive side of the cable is connected to the needle probe, which is used for lamella liftout in TEM sample preparation. The negative side of cable is connected to feedthrough outside of the SEM chamber, which is wired to bottom of a special stub. Specially made stub are used to mount ample (power or thin film) and biasing chip (e.g. from Protochips) and to make electrical connection to the negative side by sandwiching electrical cable (See Figure 2.11 (b) and (c)). The biasing chip is electrically bonded by Ag paste to bias. On the bottom side of the stub, there is ceramic bond layer that works as insulation to prevent current flow from going to SEM ground.

One of issues in this setup is Ag paste, which should be sticky enough to keep electrical connection between the stub and the chip but, at the same time, should be removed without any residue on the chip surface. This requirement is to bring the biasing chip to TEM biasing holder for further *in-situ* characterization. The TEM biasing holder achieves electrical connection with tiny needles on the chip surface (Figure 2.11 (d)), and, therefore, any debris on the chip leads to bad electrical connection and/or gives noise in acquired signal. To solve this issue, the Cu sacrificing layer is deposited onto negatively biased side of the chip by thermal evaporation. As explained in 2.1.1, while thermally evaporated metal layer can make atomic contact to the deposited layer, it has relatively weak adhesion. Utilizing such characteristics, the Cu layer works

as a sacrificing layer, where Cu protects chip surface from the direct contact of the Ag paste, as demonstrated in Figure 2.11 (e)-(g). The Cu layer is easily peeled off by Kapton tape when needed.

Biasing lamella sample preparation is quite similar process to TEM sample preparation like Mayer et al[144]. Lamella are milled out of the original sample by ion beam and liftout through a needle probe. The lamella sample lifted to the biasing chip and is mounted as it bridges between two electrodes (Figure 2.12 (a)-(c)), enabling to apply electrical bias on the lamella. Then, the mounted lamella is further cleaned and thinned by the ion beam to remove redeposited materials and to be thin enough for TEM observation. Mechanical and electrical connection of lamella with chip surface is established by Pt deposition in FIB. Once lamella is ready to be biased, constant current or constant voltage is applied to the lamella and electrical response is measured. At the same time or after the biasing, lamella sample morphology is also inspected by electron beam imaging. These are the general setup and experimental procedure to run *in-situ* biasing testing in FIB/SEM. Further details which is specific for our sample (LLTO) will be explained in the following chapter.
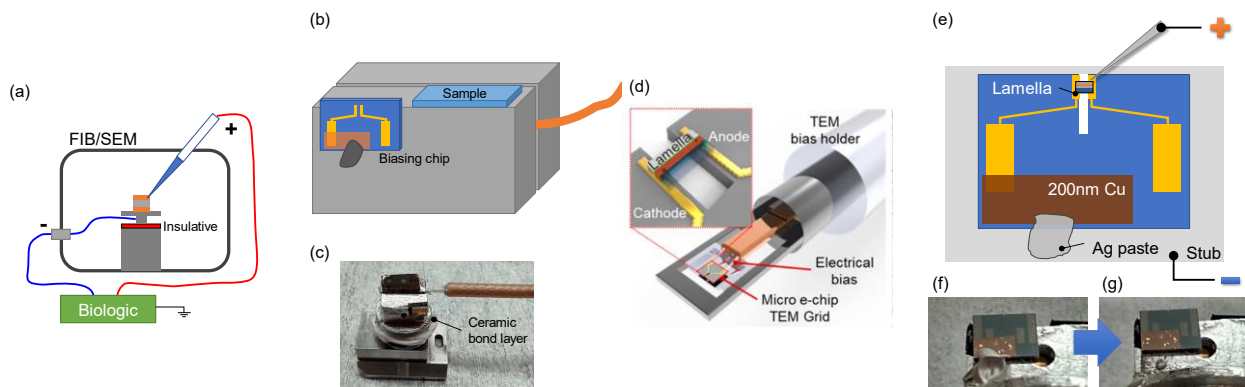
Figure 2.11 Schematic images of experimental setup for *in-situ* biasing in FIB/SEM. (a) schematic illustration of in-situ biasing configuration. (b) chip and sample mounted on special stub and (c) photograph of special stub with wire. (d) Schematic of in-situ experiment in TEM, combined with micro e-chip and TEM bias holder[145]. The biasing chip and TEM holders are from Protochips. TEM sample and (e) Schematics of chip configuration with lamella sample on the center gap and Ag paste on chip (f) after applied and (g) removed.
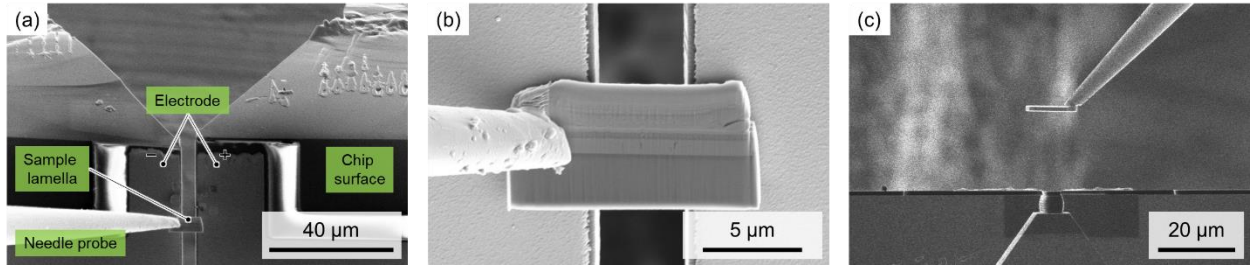
Figure 2.12 SEM images of biasing sample preparation. Electron image of lamella mounting at (a) zoom-out and (b) zoom-in. (c) Ion beam image of lamella mounting at the different angle.

Chapter 3 Interface analysis between high voltage cathode material and solid-state electrolyte

3.1 Introduction

Li-ion batteries (LIBs) are dominant battery technologies for portable electronic devices and electrical vehicles due to their high energy density, thermal stability, and long cycle life[146–149]. However, a wider adoption of LIBs requires gravimetric energy densities in excess of 350 Wh kg^{-1} (1 Wh = 3,600 Joules) at the cell level, and up to 500 Wh kg^{-1} for more than 1000 cycles[150,151]. At present, the energy densities of mass-produced LIBs are limited to 200 Wh kg^{-1} - 250 Wh kg^{-1} at the cell level[152–155]. The cathode is regarded as a critical component in improving the capacity of commercial cells. With a high operating voltage (4.7 V vs. Li$^+$/Li^0)[156–159], a spinel-type cathode material LiNi$_{0.5}$Mn$_{1.5}$O$_4$ (LNMO) could potentially empower industrial producers to achieve these high energy density goals. Recently, the strong desire to eliminate cobalt in cathode materials has sparked a renewed interest in this class of oxides[160]. Various attempts to fabricate LNMO/graphite batteries that exhibit high voltage, relatively high energy density, and fast charging capabilities using organic liquid electrolyte have been carried out worldwide[161–171], but they all suffered from excessive degradation and limited cycle life, especially when stored or cycled at a highly charged state[7]. The primary reason is that most common liquid electrolytes (e.g., carbonic ester solvent combinations with lithium hexafluorophosphate (LiPF$_6$) solute) are prone to oxidization and subsequent decomposition on the cathode surface as a cell's voltage rises over 4.5 V during charging. This is caused by a lack of an effective passivation layer[7–11], which helps prevent decomposition of the liquid electrolyte, and can cause a cell to continuously degrade.

All-solid-state batteries (ASSBs) may provide a viable pathway to use LNMO and achieve the desired high energy density and cycling stability. ASSBs have received enormous attention over the last few decades as they have good intrinsic safety, high packing density, and a relatively

large electrochemical stability window with the potential to enable both high voltage cathodes and metallic lithium anodes[16,55]. A key factor in successful integration of LNMO in ASSBs will be pairing the electrode material with a compatible electrolyte. Solid state electrolytes (SSEs) prevent catalytic dissolution of transition metals from the cathode into the electrolyte[8,12], which leads to capacity loss and graphite anode degradation when liquid electrolytes are used[8,12–14,172]. Lithium phosphorus oxynitride (LiPON) is one of the most promising candidates for this application as it has a wide electrochemical stability window up to 5.5 V[45], a modest ionic conductivity ($\approx 10^{-6}$ S cm^{-1})[45], suitable mechanical properties[173,174], and has demonstrated cycling stability against LNMO cathodes and lithium metal anodes[44,54]. The prevailing form of LiPON material as a thin film synthesized by physical vapor deposition provides an ideal platform for investigating interfaces against highly oxidative/reductive electrodes.

LiPON as a solid-state electrolyte has been studied with various types of cathode materials, including LiCoO$_2$ (LCO)[48–50], LiMn$_2$O$_4$[51,52], and LiNi$_{0.6}$Mn$_{0.2}$Co$_{0.2}$O$_2$ (NMC622)[53]. Santhanagopalan et al. observed a lithium accumulation between LCO and LiPON upon repeated cycling, which impacts the ion transport at the interface and counts for irreversible capacity loss[48]. Later Wang et al. identified the cause of lithium accumulation as a disordered LCO formation at the LCO/LiPON interface, which continues to grow at an elevated temperature and leads to a further performance degradation[49,50]. Phillip et al. reported that NMC622/LiPON interface is stable at high voltage (4.5 V vs. Li$^+$/Li^0), but the cell suffers from degradation of the bulk cathode due to amorphization, resulting in severe capacity loss[53]. All these research efforts shed light on possible degradation modes at the cathode/electrolyte interface. However, most of these effects are caused by structural change(s) within the cathode and not from LiPON decomposition. This contrasts starkly with the degradation mechanisms occurring in liquid analogues. In the case of LNMO

system, Li et al. demonstrated a LNMO/LiPON/Li thin-film full cell that cycled over 10,000 cycles with 90.6% capacity retention[54]. This exemplary cycling performance between 3.5 V and 5.1 V suggests a stable interface between LiPON and the high voltage cathode. Nevertheless, the underlying mechanism that provides such exceptional stability remains elusive, largely due to a lack of available characterization tools that can access the buried interfaces and tackle the air-/beam-sensitivity of LiPON[61].

Meanwhile, tremendous research efforts have also been invested in the study of the cathode electrolyte interface (CEI) in liquid electrolyte systems, which may hint at the potential origin of the LNMO/LiPON interface stability. The interfacial phenomena in liquid electrolyte systems have been widely characterized through spectroscopic and microscopic methods. X-ray photoelectron spectroscopy (XPS)[7,165–169] and attenuated total reflectance Fourier transform infrared spectroscopy (ATR-FTIR)[7,167] were employed to identify the chemistry of the CEIs. After cycling with a carbonate-based electrolyte, a CEI layer forms on the LNMO surface which includes decomposition products of $LiPF_6$ solute and the organic solvents LiF, Li_2CO_3, $Li_xPO_yF_z$ and polymerized ethylene carbonate (PEC). Continuous electrolyte decomposition occurrs due to the non-uniformity of the CEIs and an insufficient passivation effect. Cryogenic electron microscopy (cryo-EM) has shown that an uneven CEI layer can form after 50 cycles within a conventional carbonate electrolyte. Improved cycling and a uniform CEI was observed by the same technique but for a sulfone-based electrolyte[171]. Another factor to be considered is the addition of binders and conductive agents in composite cathodes for liquid electrolyte systems. These additives result in parasitic reactions with an electrolyte and can make deconvolution of interfacial reactions between active materials and electrolytes challenging. As such, an ideal interface between LNMO

and LiPON must limit electrolyte decomposition, result in conformal CEI formation, minimize cathode structural change, and be free of conductive agents.

An all-solid-state thin film format was employed in this study to examine the origin of the stable interface between LNMO and LiPON. The samples consisted of dense electrode layers without binder, conductive carbon, or coating materials. NDP was utilized to delineate the lithium concentration profile across the LNMO/LiPON interface. Results from this measurement were coupled with first-principles computation and cryogenic electron microscopy (cryo-EM) to investigate interfacial chemistries and textures. Based on these findings, crucial characteristics of the solid electrolyte that impact the interfacial stability are discussed and a proposal is made of key factors that facilitate the design of stable, high voltage cells by rational interface engineering.

3.2 Experimental Methods

3.2.1 Thin film sample preparation

LNMO thin-films were deposited on platinum-coated alumina substrate (Valley Design) by pulsed laser deposition (PLD) system (Excel Instruments PLD STD-12 chamber and 248 nm KrF Lambda Physik-Pro 210 excimer laser) with a laser energy fluence of ≈ 2.0 J cm^{-2} and 24000 pulses at a frequency of 10 Hz. The substrate temperature was heated to 600 °C, and partial pressure of O_2 was controlled at 200 mTorr (1 mTorr = 133.322 Pa, SI unit) during the deposition. The LNMO target used for PLD was prepared using LNMO powder (NEI corporation, USA). 12 g of LNMO powder and 0.47 g of LiOH (Sigma-Aldrich) were used to achieve a 30% Li excess LNMO target. The materials were ball milled and pelletized onto a 28.6 mm dye press at a pressure of 10 Mg for 10 min. Following this step, the pellet was sintered at 900 °C for 2 h with a heating

ramp rate of 3 °C min⁻¹. The resulting target surface was polished by sandpaper (Grit 320 and 600, Aluminum oxide, Norton abrasives) before every deposition.

LiPON thin films were deposited by radio-frequency (RF) sputtering. A Li_3PO_4 target that was ≈ 50 mm in diameter (Plasmaterials, Inc.) was used as a sputtering target. The sputtering power was set at 50 kg·m²·s⁻³ (W). Nitrogen gas (Matheson, ultra-high purity grade) and the partial pressure at 15 mTorr for deposition.

LNMO was deposited to a thickness of ≈ 650 nm and an active area of 4.9 mm², corresponding to an active material loading of 0.03 mAh cm⁻² for the full cell fabrication. LiPON was then sputtered on LNMO to a thickness of 1 μm. A Li metal anode and Cu current collector were then deposited on to the LiPON by thermal evaporation (LC Technology Solutions Inc.) under a base pressure below 3×10⁻¹¹ mTorr. The average deposition rate of Cu and Li were controlled at 0.1 nm s⁻¹ and 0.15 nm s⁻¹, respectively. Deposition was monitored by a quartz crystal microbalance. The thickness of Li metal anode was 570 nm and corresponds to a 203% excess capacity compared to that of the cathode. The thickness of the LNMO and LiPON were controlled at 2.6 μm and 2.2 μm thick, respectively, for the NDP measured samples.

3.2.2 Grazing incidence angle X-ray diffraction (GIXRD)

XRD pattern of the fabricated thin film was taken by Rigaku Smartlab X-ray diffractometer with Cu Kα source ($\lambda = 1.5406$ Å; 1 Å = 0.1 nm, SI Units) with a working voltage and current of 40 kV and 44 mA, respectively, and a scan step size of 0.04°. The scan speed was 0.12° min⁻¹, and the scan range was from 15° to 80°.

3.2.3 Liquid cell fabrication

The LNMO thin films were also tested with liquid electrolyte in a coin cell. An LNMO thin film deposited on a Pt-coated alumina substrate (1 cm² surface area, cathode) was coupled

with ≈ 100 μL of 1M LiPF$_6$ in EC:EMC (3:7 wt%) electrolyte and a Li metal chip as an anode. The coin cell consisted of a CR2032 type casing and one piece of a Celard 2325 separator. The cell was cycled between 3.5 V and 4.85 V with a 10 μA constant current.

3.2.4 Electrochemical measurement

Two LNMO/LiPON/Li full cells were cycled with a Biologic SP-200 potentiostat. For the first cell, the voltage range of the cycling was set at 3.5 V - 5.1 V and the applied current was 150 nA and 3.0 μA. This is equivalent to a ≈ C/10 and ≈ 5C charging rate, respectively. The cell was cycled at C/10 during the first 2 cycles and the last 3 cycles (1st, 2nd, and 533rd to 535th cycle) and cycled at 5C for the remaining cycles. The electrochemical cycling data of this cell has already been published in our past study[61] and its characterization by (S)TEM were conducted, shown in this paper. The other full cell was cycled for 600 cycles in the same voltage range with the current at 100 nA for 1st, 2nd, and 600th cycles and 1.7 μA for the remaining cycles, which are almost equivalent to ≈ C/7 and ≈ 4C charging rate, respectively. The second cell was fabricated for the purpose of confirming reproducibility of the cell performance, demonstrated in this paper. The areal capacity of the cells was calculated based on the assumption that only part of LNMO above Pt current collector (≈ 3 mm in diameter) was involved in the electrochemical reaction.

3.2.5 Neutron depth profiling and fitting

Neutron depth profiling (NDP) data was collected at the National Institute of Standards and Technology (NIST) Center for Neutron Research (NCNR) at the end position of the cold Neutron Guide 5. The ^{6}Li atoms in the sample were of interest for these experiments and measured through detection of the ^{3}H$^+$ (triton) charged particle products from the n,^{6}Li reaction:

$$^6Li + n_{cold} \rightarrow {}^4He^{2+}(\alpha, 2055.55 \; keV) + {}^3H^+({}^3H, 2727.92 \; keV) \qquad \text{Equation 1}$$
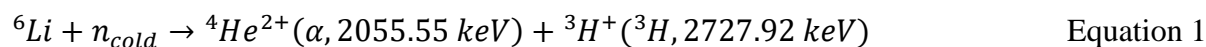
Following reaction $^4\text{He}^{2+}$ and $^3\text{H}^+$ particles are promptly produced and immediately begin to lose energy due their interactions with the nuclear and electronic properties of the sample material. However, the ^4He particles were blocked from the detector in this experiment by the polyimide cover that was added to the surface of the sample to protect the battery material from the ambient atmosphere. Only the $^3\text{H}^+$ particles were analyzed for all the samples measured.

The sample was mounted behind a 0.5 mm thick Teflon sheet with a $\approx$ 3.0 mm circular aperture. This aperture was fixed to an Al support frame and placed facing the primary transmission-type silicon surface barrier detector (Ametek) inside the NDP chamber. The energy spectra of the detected particles were collected and transmitted to a Lynx$^{\text{TM}}$ Digital Signal Analyzer (Canberra) with a setting of 4092 channels. Data were acquired for $\approx$ 5 h per sample. Each sample area was irradiated at a neutron fluence rate of $\approx 1.2\times10^9$ neutrons cm^{-1} sec^{-1}. A high-vacuum chamber was used for the measurements of the sample, background profiles (Teflon, Si wafer), and a ^{10}B concentration reference material (in house). Li atom concentrations were calculated using the natural abundance of ^6Li for sample and ^{10}B as a reference. Li concentration was calculated by the following equation:

$$D_{Li} = \frac{D_{10B}\times\sigma_{10B}[barns]}{n_{6Li}\times C_{10B}[counts\ sec^{-1}]\times\sigma_{6Li}[barns]} \times C_{6Li}[counts\ sec^{-1}] \qquad \text{Equation 2}$$

D_i is the areal concentration of ^{10}B, ^6Li, or Li (i) in i atoms cm^{-2}, σ_i is the thermal neutron cross-section for the isotope i (1 barn = 1×10^{-28} m^2), n_{6Li} is the natural abundance of ^6Li, and C_i is the normalized particle counts detected in the measurement. The calculated data was binned according to energy resolution of the NIST NDP system ($\approx$ 22 keV for a ^3H at 2727 keV). More details of the data processing can be found in the sub-chapter 3.5.

The uncertainties of both LNMO/LiPON and LNMO are <6% and reported to 1 sigma, which are estimated from the propagation of the experimental counting statistics from the sample, reference, and background materials.

3.2.6 First-principles calculations

LNMO at various charged/discharged states were studied by density functional theory (DFT) with the Vienna *Ab initio* Simulation Package (VASP). Periodic plane-wave DFT+U static calculations were performed for the LNMO bulk structure. Supercell models, $Li_8Ni_4Mn_{24}O_{32}$, were used as $Li_xNi_{0.5}Mn_{1.5}O_4$ at $x = 1$. To simulate Li removal from $x = 1$ to 0 a corresponding number of Li atoms were removed at each state. Li atoms were inserted into tetrahedral sites between octahedral sites containing Ni or Mn atoms to simulate the overlithiation of the cathode material. A 3×3×3 k-point mesh and an energy cutoff of 520 eV were employed at the calculation. U_{eff} values were chosen as 5.96 eV and 4.5 eV for the +U augmented treatment of Mn and Ni 3d orbitals, respectively. The initial MAGMOM parameters were set as follows: Li*(0), Ni*(-2), Mn*(+4), O*(0). Partial density of states (PDOS) at pristine state ($x =1$) and Overlithiated state ($x = 2$) were extracted from DOSCAR and analyzed by wxDragon software. PDOS plots were smoothed by a 10-point adjacent average function.

3.2.7 Cryogenic focused ion beam/scanning electron microscopy (cryo-FIB/SEM)

A FEI Scios DualBeam FIB/SEM with a cooling stage was used to prepare the TEM samples of pristine LNMO/LiPON and cycled LNMO/LiPON/Li samples. The operating voltage of the electron beam was 5 kV and emission current of the beam was 50 pA. These setting were used to mitigate potential beam damage on Li and LiPON. A Ga ion beam source was used to mill and thin the sample with an operating ion beam voltage of 30 kV. Emission currents of the ion beam were selected depending on purposes: 10 pA for ion beam imaging, 0.1 nA for cross-section

surface cleaning and lamella thinning, and 3 nA for pattern milling. The sample stage temperature was maintained at -185 °C during pattern milling, cross-section cleaning, and lamella thinning processes to preserve the Li metal and LiPON components. A cryo-liftout methodology was applied for the TEM sample lift-out process where sample materials were redeposited between the lamella and the probe for connection. Detailed procedures with illustration were described in our past study[61].

3.2.8 Cryogenic transmission electron microscopy (cryo-TEM)

The prepared lamellas were transferred from the FIB chamber though an air-free quick loader and stored in an Ar-filled glovebox. Cryo-HRTEM images were collected on a JEOL JEM-2100F TEM at 200 kV with a Gatan Oneview camera. Cryo-STEM/ EELS results were collected on a JEOL JEM-ARM300CF TEM at 300 kV. A TEM cryo-holder (Gatan 626 cryo-transfer holder) was used to load the samples where TEM grids were immersed in liquid nitrogen and then mounted onto the holder via a cryo-transfer workstation[61]. Uncertainty of the energy loss in EELS spectra are 1 eV, which is attributed to the energy resolution of the detector.

3.3 Results and discussion

3.3.1 Electrochemical behavior of LNMO/LiPON/Li full cell over long-term cycling

The presence of a stable interface was first demonstrated by a thin film battery consisting of a high-voltage spinel LNMO cathode, a LiPON solid electrolyte, and a lithium metal anode. The detailed architecture of the cell is shown in Figure 3.1, where the deposited LNMO thin film displays a well crystallized structure with (111)-plane-orientated texture in Figure 3.2 (a). This is in good agreement with the films produced by Xia et al.[40,41] Figure 3.3 illustrates the cycling performance of the full cell. As shown in Figure 3.3 (a), the 1st cycle charge profile displays an

excess capacity compared with the subsequent cycles, while the voltage profiles at the 2nd cycle and 600th cycle resemble each other, implying an irreversible reaction during the 1st cycle and a superior cyclability afterwards. The cycling stability is further demonstrated by a Coulombic efficiency of $\approx$ 99.6% for 600 cycles in Figure 3.3 (b). Compared with the LNMO cathode performance in liquid electrolyte such as Figure 3.2 (b), two characteristic features are observed in the thin film battery with the LiPON solid electrolyte: *i*) an excess capacity during the first charge and *ii*) cycling stability observed for the course of 600 cycles. Note: 1 mAh is equal to 3.6 C (SI units).
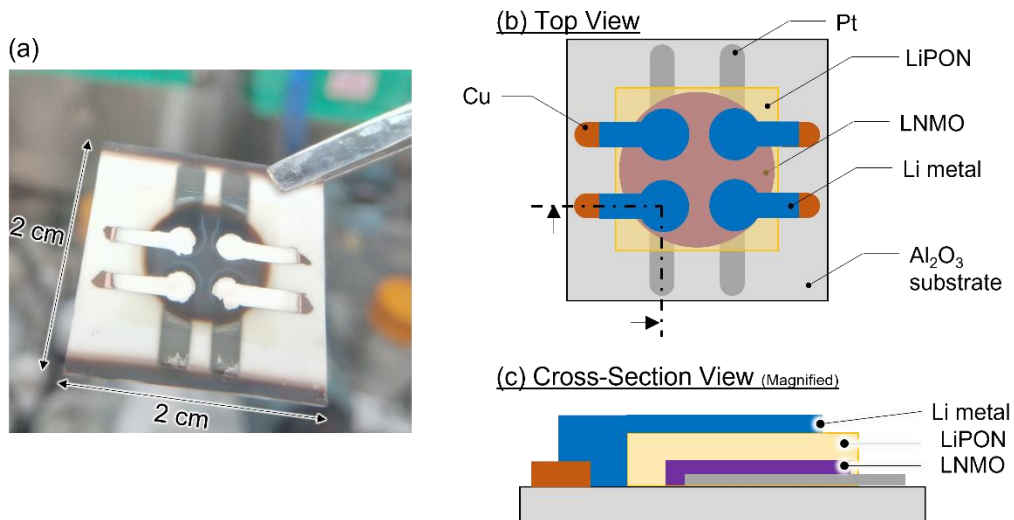
Figure 3.1 LNMO/LiPON/Li full cell configuration. (a) Photo image of LNMO/LiPON/Li thin film full cell and (b, c) schematic of the cell configuration
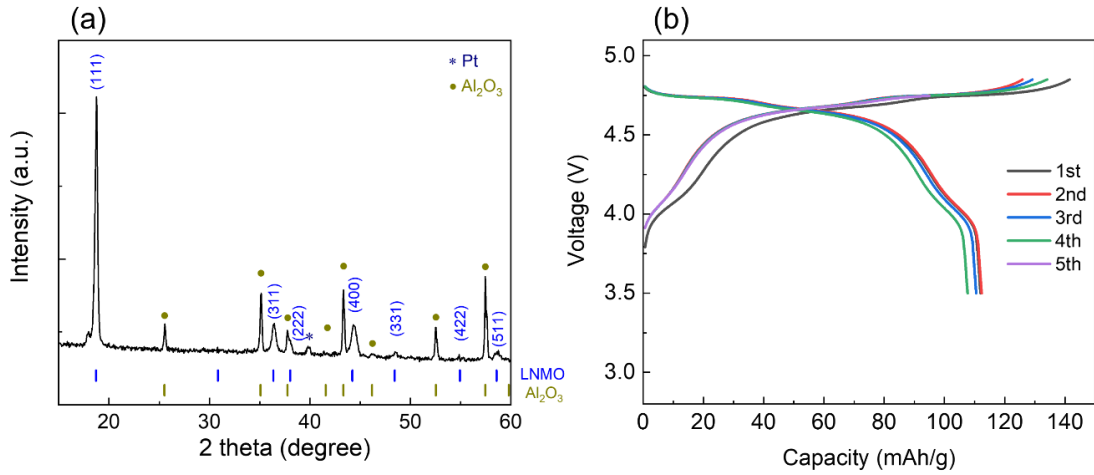
Figure 3.2 Properties of bare LNMO thin film. (a) XRD pattern of LNMO deposited on Pt-coated alumina substrate. (b) Voltage profiles of LNMO/Li half-cell with carbonate-based electrolyte. Uncertainty of the capacity is about 25%, which comes from the estimation of LNMO active mass.

The voltage profiles indicate that the dominant redox reactions in the LNMO cathode are 4.7 V vs. Li^+/Li^0 (shown as plateau region III in Figure 3.3 (a)) and correspond to the Ni^{2+}/Ni^{3+} and Ni^{3+}/Ni^{4+} redox couples during the initial charging process[175,176]. A small amount of Mn^{3+}/Mn^{4+} redox couple occurring near 4 V (plateau region II in Figure 3.3 (a)) contributes to the nominal capacity when part of the Mn species in a pristine LNMO thin film has an oxidation state lower than 4+. The LNMO thin film is likely overlithiated chemically during the full cell fabrication, which leads to a lower Mn oxidation state in the surface region of LNMO. This is apparent in regions I and II (Figure 3.3 (a)), where an excess of charge capacity during the first cycle is caused by a plateau at 2.9 V and 4 V. Note that the pristine LNMO thin film cycled in liquid electrolyte does not exhibit an overlithiated feature as indicated by Figure 3.2 (b) and previous studies[40,41]. The overlithiation of LNMO is proposed to be caused by LiPON deposition and chemical reactions between LNMO and LiPON during or after the deposition.

53
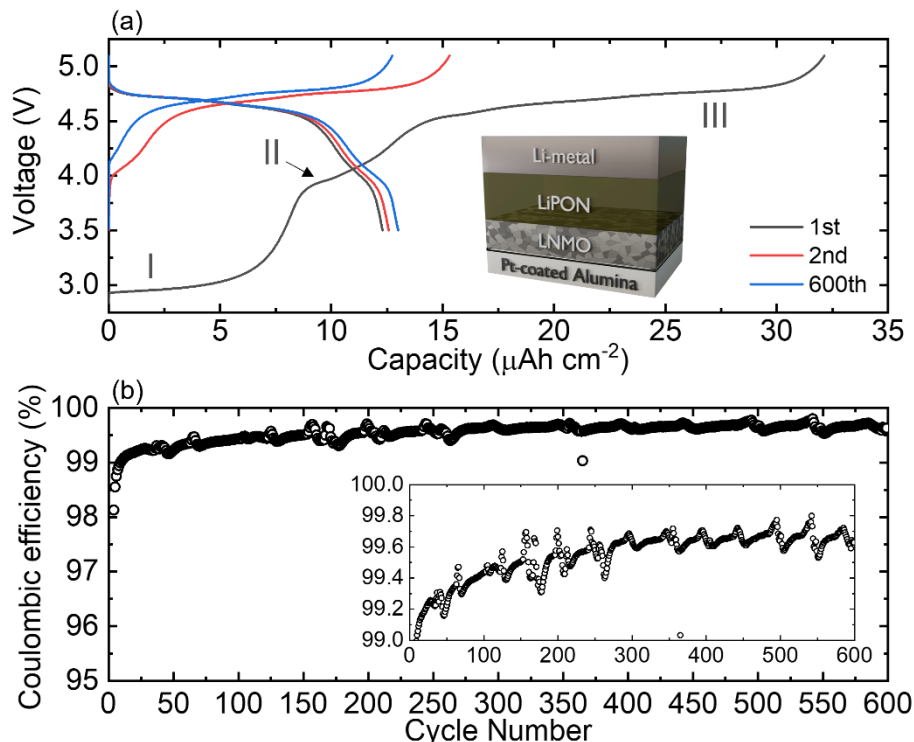
Figure 3.3 Electrochemical performance of LNMO/LiPON/Li full cell. (a) Voltage profiles of LNMO/LiPON/Li thin film full cell at 3.5 V - 5.1 V at the 1st, 2nd, and 600th cycle. (b) Coulombic efficiency of the cycled cell, which was charged/discharged at a about C/7 for the 1st and 2nd cycles, and 4C for the rest of cycles. The C rate was set back to C/7 at the 600th cycle. Uncertainty of the areal capacity in the voltage profile is ~3%, attributed to the estimation of the cell active area. Periodic fluctuation of the Coulombic efficiency comes from temperature change in a day during the measurement.

3.3.2 Li concentration gradient across LNMO/LiPON interface

Neutron depth profiling (NDP), is a robust method by which select light elements (e.g., Li) can be quantified[177]. Unlike XPS depth profiling technique, NDP is a nondestructive approach,[137,178] which enables the quantification of the average Li concentration through the sample along the thickness direction. There have been numerous studies over the last several years, where NDP has been applied to the study of Li-ion battery materials[135,177,179–181]. In this study, NDP was utilized to examine the Li concentration profile of a pristine LNMO/LiPON sample to investigate the possibility of LNMO overlithiation.

Figure 3.4 (a) is a schematic of NDP measurement setup, where samples are mounted in a vacuum chamber and cold neutrons are directed at a sample. Along the pathway, neutron may react with ^{6}Li and generates charged particles, ^{4}He^{2+} (alpha) and ^{3}H$^+$ (triton), with characteristic kinetic energies. Note that alpha particles are filtered out by the thin polyamide film cover and only the triton particles are detected. The energy loss of the charged particles as they pass through the material is due to the stopping power of the material. Li concentration as function of depth is obtained by plotting the detected number of triton particles as a function of final kinetic energy. During this experiment, a LNMO/LiPON thin film sample was measured by NDP, with a LNMO thin film measured as a reference for the interface sample. Figure 3.4 (b) exhibits triton-based Li areal concentration depth profiles from the LNMO/LiPON sample (black), LNMO sample (red), and their subtraction (blue) in Li atoms cm^{-2}. The subtracted profile represents variations in Li across the bulk and interface regions of sample after the LiPON layer is added to the LNMO.

To estimate the contributions from the bulk LiPON and interface regions, the subtracted curve (blue dots in Figure 3.4 (b) and (c)) is fit with a Weibull function (details explained in supporting information and Table S1)[182] in the energy range between 2551 keV and 2358 keV, where bulk LiPON is dominant in the LNMO/LiPON sample. The fit model is then extrapolated to the lower energy region to estimate the Li concentration contributed from pure LiPON (magenta curve in Figure 3.4 (c)). Lastly, the subtraction of the extrapolated model (magenta curve in Figure 3.4 (c)) from the calculated curve (blue curve in Figure 3.4 (c)) is plotted as a green line in Figure 3.4 (c), which represents the interfacial effect from the LNMO/LiPON sample. As shown in the inset of Figure 3.4 (c), a noticeable difference in Li concentration between the subtracted (blue) and the extrapolated curve (magenta) can be observed. The positive difference (green) suggests a slight increase of Li concentration at the interface between LNMO and LiPON. Such Li

concentration increase (atoms cm^{-3}) in LNMO is further estimated by integrating areal Li concentration in atoms cm^{-2} from the energy range between 2358 keV to 2200 keV, which falls into LNMO region. The integration gives a Li concentration increase of $\approx 4.00 \times 10^{20}$ atoms cm^{-3} at the LiPON/LNMO interface, which is ca. 3% of the concentration compared with the designed stoichiometry of $LiNi_{0.5}Mn_{1.5}O_4$ cathode. It is worth noting that there is a difference on the amount of overlithiation between NDP and electrochemical testing. This comes from the different quantities that are measured in each characterization – NDP detects all the Li in the film while electrochemical testing solely measures the activated Li ions. It should be emphasized that NDP measures Li concentration across open aperture area centered on the film and demonstrates a 3% Li increase relative to all the cathode materials in the thin film sample. In contrast, the difference between 1st and 2nd charge capacity measured by electrochemical testing only represents how much activated Li in the first cycle is reversible. Considering a higher discharge voltage cutoff (3.5 V) than the open circuit voltage of pristine $Li_{1.0}NMO$ (≈ 2.8 V) is used, the difference is attributed to the sum of overlithiated Li and irreversible capacity during cycling. Furthermore, electrochemical testing does not necessarily activate all the materials inside the sample, suggesting the observed capacity would not always match actual Li amount in cathode[183].

NDP results indicate an increased Li concentration at the LNMO/LiPON interface. One possible source of this increase is overlithiation of the LNMO surface. Different lithiation states of LNMO were therefore investigated with first-principles calculations to further understand the impact of overlithiation on LNMO material. The L_xNMO modeling structure was altered from $x = 0$ to $x = 2$ to represent the delithiated state and overlithiated state of LNMO, respectively. (Figure 3.4 (d)). Figure 3.4 (e) displays the average magnetizations of Mn and Ni species calculated at each lithiation state; this can be used as an indicator of the oxidation state(s) of transition

metals[184,185]. The magnetization number of Ni decreases from 1.7 μ_B to 0.5 μ_B (1 μ_B = 9.274×10^{-24} J T^{-1}, SI units) during the delithiation (charging) process (x = 1 to 0). This indicates that the Ni redox changes from Ni^{2+} to Ni^{4+} for the charging process[184,185]. The magnetization number of Ni does not vary due to overlithiation (x = 1 to 2). In contrast, Mn magnetization changes from 3.2 μ_B to 3.7 μ_B when the structure is overlithiated, suggesting a Mn reduction as more Li is inserted into LNMO.
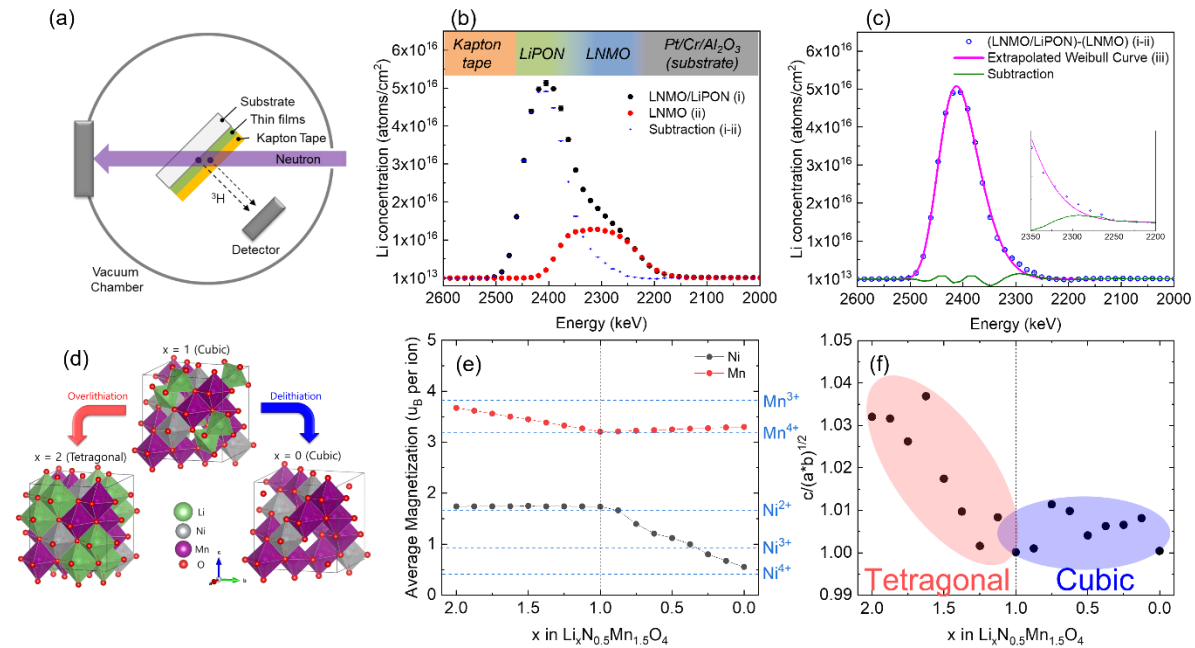
Figure 3.4 Li concentration across LNMO/LiPON interface. (a) Schematic image of neutron depth profiling (NDP) setup. (b) Li concentration profile (atoms/cm^2) of LNMO/LiPON (black), bare LNMO (red), and subtraction of bare LNMO from LNMO/LiPON as a function of detected triton energy. (c) Li concentration profile of subtraction of bare LNMO from LNMO/LiPON (blue, same data in (b)), Li concentration of bare LiPON simulated with Weibull function (magenta), and subtraction of simulated curve from (LNMO/LiPON)-(LNMO) curve (green). (d) Structures of Li$_x$Ni$_{0.5}$Mn$_{1.5}$O$_4$, which are used for DFT calculation, at x = 1 (pristine), x = 0 (delithiated), and x = 2 (overlithiated). (e) Averaged magnetization of Ni (black) and Mn (red) at each lithiated state of LNMO. (f) Relative c length of the supercell at each lithiation state from x = 0 to x = 2 in L$_x$NMO.

Along with the change in magnetization numbers, the relative lattice parameter evolution of the supercell at each lithiation state is plotted in Figure 3.4 (f). When x in the L$_x$NMO structure exceeds 1, the lattice parameter in c direction becomes relatively longer than the a and b directions.

This leads to a distortion of the lattice in the *c* direction and, consequently, a phase transformation to a tetragonal phase. Such Jahn-Teller (J-T) distortion is attributed to the presence of Mn^{3+}. The Mn cation is normally located at octahedral site bonded with O anions. This causes the classical ligand field splitting (crystal field splitting) and, as a result, d-electron states can be split into triplet (t_{2g}) and doublet (e_g) states, which stabilizes the Mn-O bonding configuration. In the case of Mn^{3+}, three of the four 3d electrons are in d_{xy}, d_{yz} and d_{zx} orbitals of the t_{2g} state and leaves one d_{z2} electron in e_g state (high spin state). The Mn-O octahedral structure becomes elongated in the *c* direction to minimize Coulombic repulsion between the electrons in Mn d_{z2} orbital and the electrons in O 2p orbital as the d_{z2} electron orbitals are parallel to the *c* direction of the octahedron. Therefore, the presence of J-T distortion when $x > 1$ implies the reduction of Mn from 4+ to 3+. This matches with the average magnetization results in Figure 3.4 (e).

3.3.3 Mn oxidation state evolution at LNMO/LiPON interface

Scanning transmission electron microscopy/electron energy loss spectroscopy (STEM/EELS) were then conducted to experimentally verify the oxidation state of Mn across the LNMO/LiPON interface. Cryogenic protection was applied on the TEM specimens during STEM measurements, given the beam sensitivity of LiPON as reported in the past study[61]. Figure 3.5 (a) displays the cryo-STEM high-angle annular dark field (HAADF) image of the pristine LNMO/LiPON interface, where LNMO and LiPON regions can be identified based on differences in contrast. The highlighted spots represent the region where EELS spectra were extracted. Mn L-edge spectra are plotted in Figure 3.5 (b). The low signal intensity detected in the Mn L-edge spectrum at spot 0 indicates the absence of Mn in this region and that the major component is LiPON. The characteristic peaks of Mn L-edge appear in the spectrum from spot 1 to spot 5, suggesting the range of the LNMO/LiPON interface region. The L_3 and L_2 peaks of Mn L-edge

correspond to electron transition from $2p_{3/2}$ and from $2p_{1/2}$ to unoccupied d orbitals, respectively[186]. The oxidation states of the transition metal species can be identified by analyzing the intensity ratio between L_3 and L_2 peaks and comparing it to the values collected on standard Mn compounds in which the oxidation states of Mn are known. A step function is commonly used to fit these spectra so that the intensity ratio of L_3 peak to L_2 peak can be calculated and plotted[186], as shown in Figure 3.5 (c). In Figure 3.5 (c), Mn at spot 1 shows a L_3/L_2 intensity ratio ≈ 2.9, while the ratio decreases to ≈ 2.4 for the Mn from spot 2 to spot 5. According to Wang et al., L_3/L_2 intensity ratio of 3.85, 2.6, and 2.0 corresponds to Mn^{2+}, Mn^{3+}, and Mn^{4+} oxidation states[186], respectively. Therefore, the oxidation state of Mn at the starting of the LNMO/LiPON interface is likely to be between Mn^{3+} and Mn^{2+}. This Mn oxidation state at the interface was more reduced than the one found within the LNMO bulk, which is comparable with a bare LNMO thin-film sample. The computational results reveal that Mn oxidation state is reduced from 4+ to 3+ when LNMO is overlithiated and form L_xNMO ($x > 1$), as shown in Figure 3.4 (d). The combination of Mn L-edge intensity ratios, computational results and electrochemistry indicate that Mn at LNMO/LiPON interface (spot 1) shows an oxidation state of 3+, which is likely attributed to the overlithiation of LNMO, while bulk LNMO shown at spot 2 to spot 5 has mixed states of Mn^{3+} and Mn^{4+}. Another possible cause of Mn reduction is the bombardment of LiPON during sputtering. Song et al.[175] has shown that oxygen vacancy can trigger Mn^{3+} generation from Mn^{4+} for charge compensation, and cathodes with more oxygen vacancy can deliver a longer plateau at 4.0 V in the voltage profile. The Mn^{3+} ions should be oxidized to Mn^{4+} during the charge in the 1st cycle and remain above 3+ after the discharge to 3.5 V as the electrochemical lithiation voltage corresponding to $Mn^{4+} \rightarrow Mn^{3+}$ is at 2.8 V[33,176].

Figure 3.5 (d)-(f) shows the Mn oxidation states at LNMO/LiPON interface after 500 cycles. As can be seen in Figure 3.5 (e), the absence of Mn signal at spot 0 in the STEM image (Figure 3.5 (d)) demonstrates there is no Mn migration from LNMO to LiPON region, in stark contrast to the Mn dissolution phenomena in liquid electrolyte system. Compared to the pristine interface (Figure 3.5 (c)), the cycled interface has much decreased L_3/L_2 intensity ratio at spot 1 in Figure 3.5 (f), indicating a less reduced Mn environment. During the charging process in the 1st cycle, excess lithium atoms that caused overlithiation of the LNMO are extracted, a process manifests as a plateau at 2.9 V in the electrochemical measurement. Reduced Mn (Mn^{3+}) due to overlithiation and LiPON deposition is also oxidized in the 1st charge, rationalizing the measured increased Mn oxidation state in subsequent cycles.
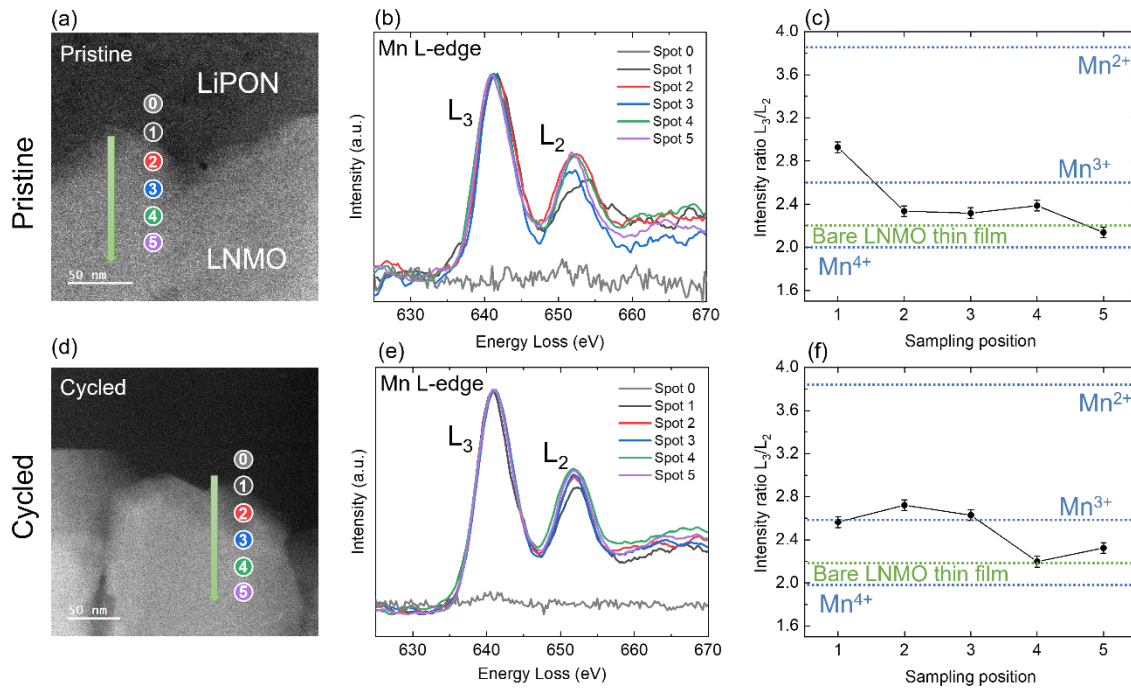
Figure 3.5 Mn oxidation state changes across the pristine and cycled interface. (a-c) Analysis of pristine LNMO/LiPON interface and (d-f) cycled LNMO/LiPON interface. Cryo-STEM image (a) at pristine interface and (d) at cycled interface. (b) Mn L-edge EELS spectra at each point of pristine interface and (e) cycled interface. Intensity ratio of Mn L_3 peak to L_2 peak with error bars (c) for pristine interface and (f) cycled interface. Details of the intensity integration method are illustrated in Figure S3.

3.3.4 Nanostructure and morphology at LNMO/LiPON interface

The nanostructure and morphology of the layers were additionally characterized to elucidate the interfacial stability and to compliment the above discussed chemical analyses. Cryo-TEM images at the LNMO/LiPON interface before and after cycling were obtained and summarized in Figure 3.6. Figure 3.6 (a) shows the high-resolution TEM (HRTEM) image of pristine LNMO/LiPON interface. No voids or cracks are formed when LiPON is deposited on LNMO. Detailed nanostructure was also inspected and shown in Figure 3.6 (b) and (c). Lattice fringes observed in these images match well with (111) lattice plane of LNMO[187,188] and indicates that LNMO maintains its crystal structure after the full cell preparation. Note that LNMO structure should be slightly distorted due to the lithiation and Mn reduction as aforementioned, while the lattice spacing change due to distortion is significantly small and was not detectable with HRTEM. More details about the calculation on lattice spacing change are included in the Supporting Information. A cycled LNMO/LiPON interface is shown in Figure 3.6 (d). It displays surprisingly intimate contact between the LNMO and LiPON layers and an absence of voids or cracks, even after 500 cycles. Figure 3.6 (e) and (f) demonstrate that the crystal structure of LNMO is maintained in both the bulk and interface regions. Although the cell was cycled at a rate of 5 C, which can be considered as fast cycling and results in the cell having 40% of its original capacity, the LNMO/LiPON interface remains intact and shows no signs of structural change or defect formation. In Figure 3.6 (g)-(k), a clear difference between crystalline region and amorphous region is highlighted by the yellow curve along the cycled LNMO/LiPON interface. Very little CEI is observed in this region. These observations provide good evidence for the long-term structural stability of the LNMO/LiPON interface.

An interesting phenomenon was observed in the LiPON after 500 cycles. Cryo-HRTEM imaging of the LiPON in a pristine LNMO/LiPON sample (Figure 3.7 (a)) indicates nanocrystal formation in areas highlighted by the yellow dot lines. These nanocrystalline species are identified as Li_3PO_4 and Li_2PO_2N through the features in Fast Fourier transform (FFT) patterns shown in Figure 3.7 (b) and (c). These are likely to be decomposition products of LiPON based on past computational results[19]. Such partial decomposition occurs only at a small portion of the interface. Similar phenomenon is observed at the cycled LNMO/LiPON interface (Figure 3.8 with lattice patterns displayed in (a) and FFT analysis displayed in (c)-(e)). The presence of LiPON partial decomposition in both pristine and cycled LNMO/LiPON interfaces implies that such decomposition is driven chemically instead of electrochemically. This is discussed further in the following section.
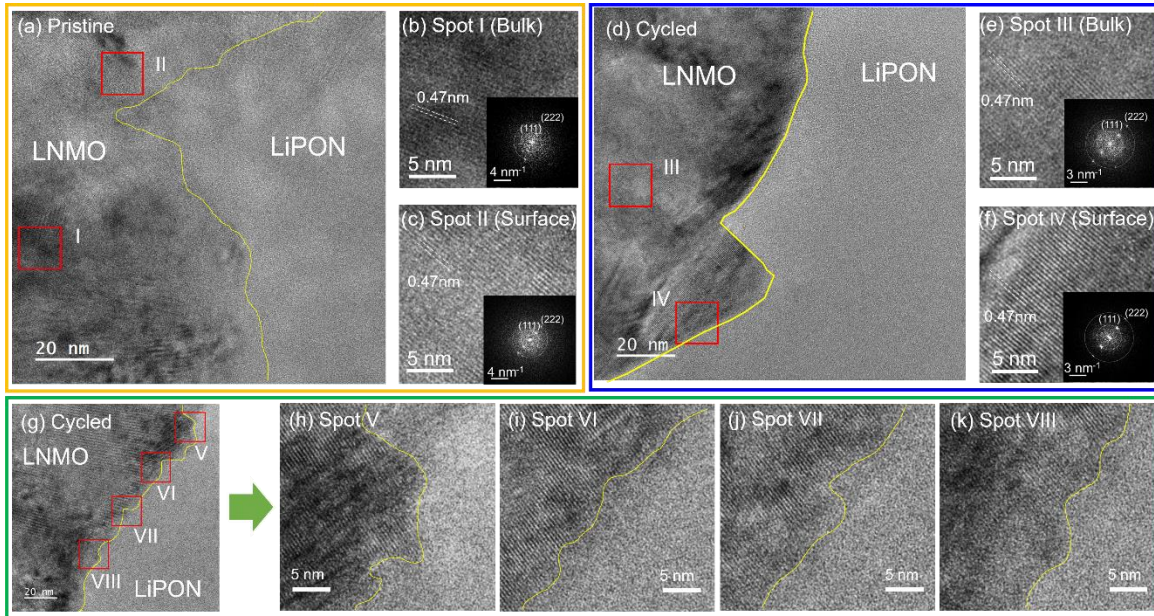
Figure 3.6 Interfacial nanostructure and morphology at the LNMO/LiPON interface(a) Cryo-TEM image of pristine LNMO/LiPON interface and (b) zoomed LNMO images of bulk (inset; FFT image) and (c) surface (inset; FFT image). (d) Cryo-TEM image of cycled LNMO/LiPON interface and (e) zoomed LNMO images of bulk (inset; FFT image) and (f) surface (inset; FFT image). (g) Another cryo-TEM image of cycled LNMO/LiPON interface and (h-k) zoomed interface images at different spots
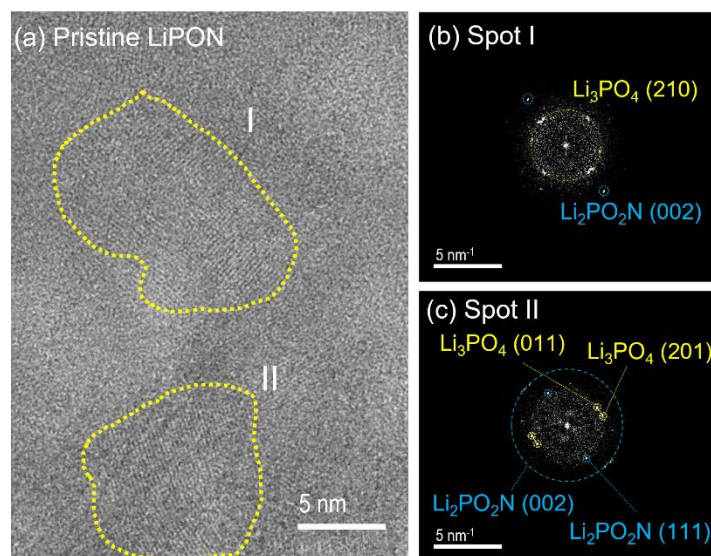
Figure 3.7 Cryo-TEM of pristine LNMO/LiPON. (a) Cryo-TEM image of LiPON in pristine LNMO/LiPON. FFT images of (b) spot I and (c) spot II.
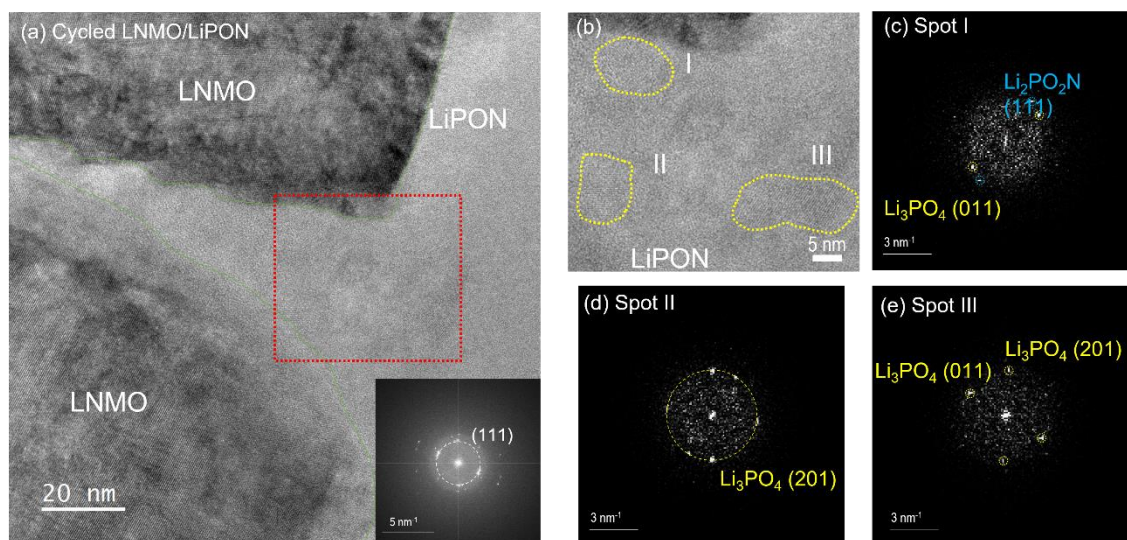
Figure 3.8 Cryo-TEM of cycled LNMO/LiPON. (a) Cryo-TEM image of cycled LNMO/LiPON and (b) magnified image of the area surrounded by red dot lines in (a). FFT images of (c) spot I, (d) spot II, and (e) spot III.

3.3.5 An electrochemically stable and mechanically compatible solid-solid interface

The stability at LNMO/LiPON interface stems from two separate perspectives: *i*) the intrinsic structural resilience of LNMO, and *ii*) the unique characteristics of LiPON. The LNMO material's spinel crystal structure determines its ability to accommodate excess Li. Upon

overlithiation, LNMO experiences a phase transformation from cubic to tetragonal structure while it homes extra Li in the structure without sabotaging the cyclability and interface stability. Spinel analogue anode material, $Li_4Ti_5O_{12}$ (LTO), undergoes a similar phase transformation when extra Li is inserted into the structure while maintaining LTO's highly reversible cycling performance.[189] Contrary to spinel oxides, layered oxides are prone to unfavorable changes with excess Li. LCO suffers from the formation of a disordered phase that comprise of a mixture of Li_2O and CoO between ordered LCO and LiPON during sputtering process. This results in an extra interfacial impedance and can inhibit cycling performance.[48–50] $Li_xNi_{0.8}Mn_{0.1}Co_{0.1}O_2$ (NMC811), another layered cathode material, experiences a 45.5% capacity loss in subsequent cycles after deep discharging to 0.8 V vs. Li/Li^+ in the initial cycle in the liquid electrolyte system.[190] The ability of spinel oxides to withstand surface overlithiation renders LNMO suitable for coupling with LiPON electrolyte, and serves to increase the surface Li chemical potential of the cathode for better interfacing with solid electrolytes.

Three aspects can be considered regarding the uniqueness of LiPON material. The overarching factor is the electrochemical stability of LiPON. Partial decomposition of LiPON is observed after its deposition onto LNMO surface. This indicates a certain extent of chemical incompatibility. However, long-term cycling does not result in additional decomposition of LiPON. Rather, most of the LiPON remains amorphous along the interface. This implies that LiPON is electrochemical stable against a high voltage LNMO cathode. Further EELS analysis at the cycled LNMO/LiPON interface shows no noticeable changes in the P and N chemical environments, which suggests the stability of LiPON's chemistry against highly oxidative potential (Figure 3.9). Such electrochemical stability could be influenced by the increased Li concentration estimated from the NDP results. The ascending Li content across the interface from

LNMO to LiPON region represents a gradually ramping chemical potential, which mitigates the oxidative potential from high voltage LNMO and protects LiPON from further decomposition[55]. Coupling with the analogous chemical gradient feature observed at Li/LiPON interface elsewhere[61], the presence of gradient interfaces, which exhibits exemplary electrochemical stability, hint on the plausibility of engineering solid-solid interfaces so that drastic chemical potential differences between electrode and electrolyte can be diminished to achieve desired stability. Such features also serve to eliminate the possible effect from space charge at the interface, even though the impact from Li deficient layer in SSE, as proposed in space charge theory, on interfacial transport properties remain inconclusive[58,59,191,192].
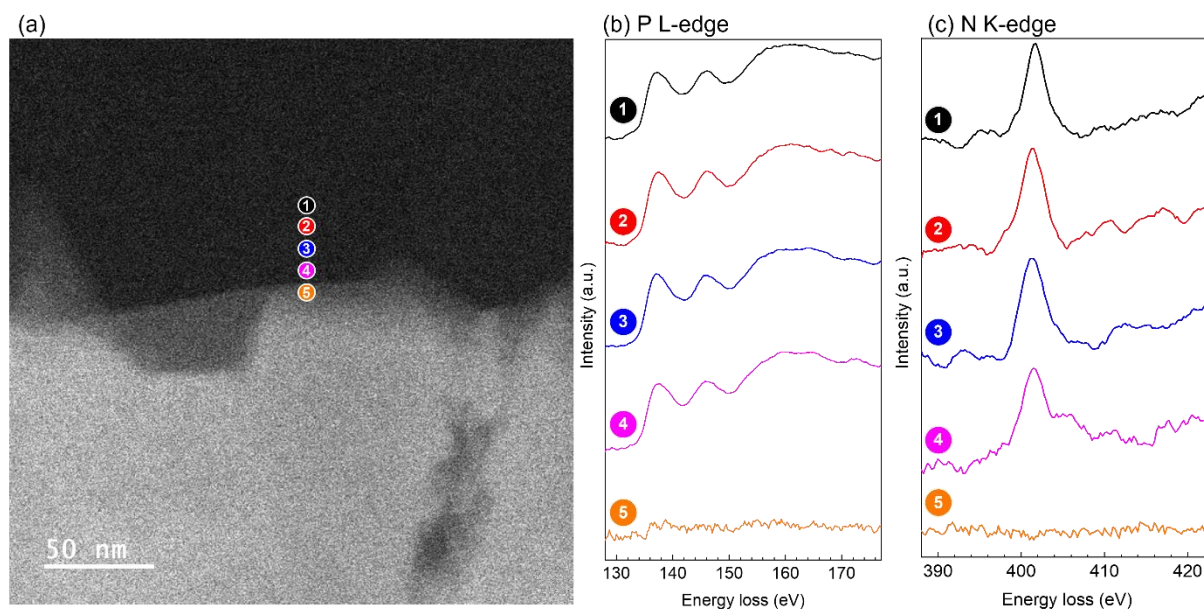
Figure 3.9 Compositional analysis of the cycled LNMO/LiPON interface by EELS. (a) STEM HAADF image of cycled LNMO/LiPON interface. (b) P K-edge and (c) N K-edge EELS spectra at each spot as highlight at the cycled interface in (a).

Another aspect of LiPON being stable against LNMO ties into its mechanical characteristics. Herbert et al. measured the Young's modulus of LiPON by nanoindentation and

obtained a value of 77 GPa[173]. This high modulus provides LiPON a rigid characteristic. However, Lee et al. reports a 11% - 13% volume change of L_xNMO cathode upon lithiation from x = 0 to x =2.[176] Given the polycrystalline feature of LNMO cathode, anisotropic stress generated at the interface during such repeated volumetric changes can cause catastrophic impact on LiPON's bulk structural integrity such as cracking or delamination, while none of these issues were observed to occur at the LNMO/LiPON interface. The fact that LiPON retains an intact contact with LNMO after long-term cycling suggests that the LiPON in this study may be a relatively soft material. This is consistent with some observations on the flexibility of LiPON in literature[174,193], yet further experimental validation is needed.

The last aspect of LiPON's stability against LNMO correlates with its morphological characteristics. LiPON is known for its amorphous structure and dense, pinhole-free feature. Such merits of LiPON give rise to its even coverage over LNMO after deposition and facilitates a uniform overlithiation on an LNMO surface, namely a conformal interface. In the case of a liquid electrolyte system, the CEI tends to be non-uniform in both composition and thickness, due to the hardly controllable mass transfer in a liquid environment, which diminishes the passivation effect of such interfaces. Compared to studies with other solid electrolytes (i.e., $Li_7La_3Zr_2O_{12}$ and Li_6PS_5Cl, etc.), roughness at the pelletized cathode/electrolyte interface can incur inhomogeneity in terms of contact and pressure, resulting in interface non-uniformity[194,195]. Given the compatibility of LiPON against varieties of cathodes, an artificial LiPON layer deposited on a cathode surface could serve as a simple protection strategy to alleviate the interfacial reaction between a less electrochemically stable solid electrolyte and highly oxidative cathode material. Alternatively, employing methodologies for producing glassy material (e.g., via fast quenching)

to amorphize conventionally crystalline solid electrolytes through the creation of defects could well steer the morphological features and enhance interfacial stability.

It should be noted that the absence of a carbon conductive agent also helps to achieve the stable cycling performance. Although carbon additives improve electronic conductivity of a cathode or an anode composite electrode, past researches has indicated that carbon additives can accelerate the decomposition of an electrolyte and form CEI on a cathode's surface[196,197] and SEI on an anode's surface[198], causing capacity degradation of cells. The high electronic conductivity of the carbon also creates an electronic pathway for electrolyte redox reactions to occur. Therefore, it is critical to avoid carbon or minimize its surface area to suppress the kinetics of the electrolyte decomposition.

To better illustrate the interface configuration between LNMO and LiPON, a schematic is shown in Figure 3.10. Examinations of an LNMO/LiPON interface using NDP, DFT and cryo-EM yields intriguing results that are closely related to the stability of the materials' interface. An ideal cathode electrolyte interface requires the electrolyte to remain either chemically or electrochemically stable against the cathode and mechanically robust. An as-formed CEI ought to be uniform and conformal, consisting of species that are electronical insulating and ionically conductive to prevent further decomposition of electrolyte. Finally, the cathode should be able to retain the crystal structure after extended cycling.
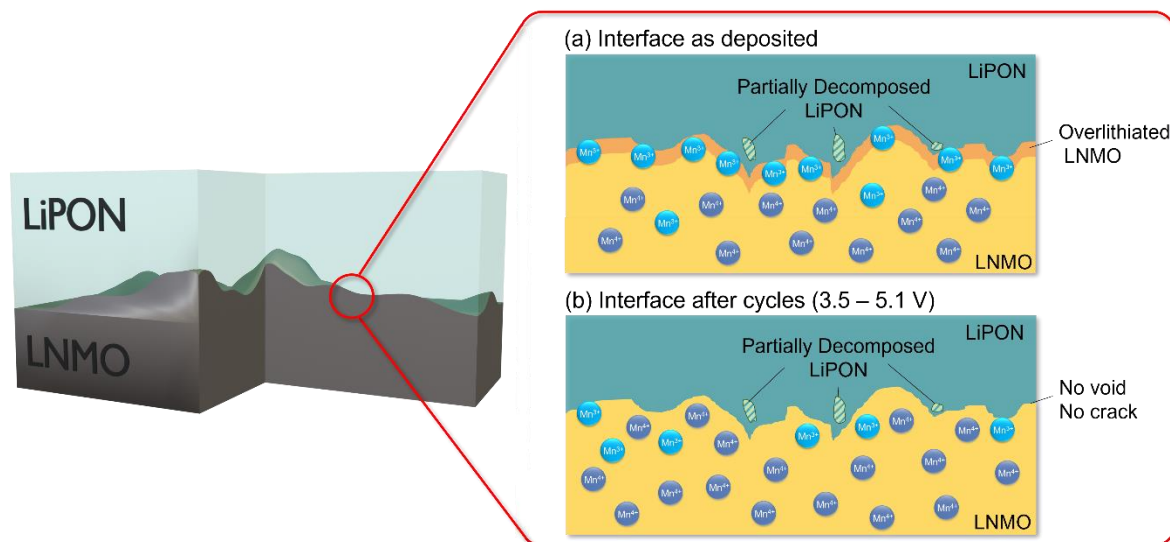
Figure 3.10 Schematic illustration of microscopic LNMO/LiPON interface At the LNMO/LiPON interface (left), microscopically LNMO/LiPON contact without void and cracks both (a) as deposited and (b) after cycling between 3.5 V - 5.1 V. As deposited interface in (a), overlithiated regions is likely to exist in LNMO, where Mn oxidation state is reduced to 3+. After cycling (b), such area disappears and Mn^{4+} is dominant in overall LNMO. In both interface, partial decomposition of LiPON is observed. Not to scale.

3.4 Conclusions

New insights into the interface between LNMO cathode and LiPON solid electrolyte have been gained by combining targeted spectroscopic, microscopic, and computational tools. An overlithiation layer of LNMO at the LNMO/LiPON interface due to LiPON deposition is revealed by NDP, which accounts for the excess capacity during the 1st charge of LNMO. Overlithiated LNMO exhibits a Mn oxidation state change from 4+ to 3+ as confirmed by both DFT prediction and cryo-STEM/EELS examination. The cathode structure is intact under the overlithiation and is not significantly impacted after electrochemical activation. Cryo-TEM further shows a LNMO/LiPON interface with intimate contact that is free of voids and cracks over the course of 500 cycles. STEM/EELS demonstrates that major elements across the interface keep their original chemical bonding environment. The observed conformal and stable interface contributes to the electrochemical stability of LiPON against LNMO. The knowledge gained from additive-free electrodes and its close contact to mechanically and electrochemically compatible SSE

demonstrate that the long-term cycling stability of 5 V-class cathode materials is achievable with dedicated interface engineering.

3.5 Supplementary Information about Neutron depth profiling (NDP)

3.5.1 NDP fitting

Subtracted NDP profiles Figure 3.4 (c, blue) in the range between 2551 and 2358 keV were fitted with the following Weibull function:

$$y = a_0 \left(\frac{a_3 - 1}{a_3}\right)^{\frac{1-a_3}{a_3}} \left(\frac{x - a_1}{a_2} + \left(\frac{a_3 - 1}{a_3}\right)^{\frac{1}{a_3}}\right)^{a_3 - 1} \exp\left[-\left(\frac{x - a_1}{a_2} + \left(\frac{a_3 - 1}{a_3}\right)^{\frac{1}{a_3}}\right)^{a_3} + \frac{a_3 - 1}{a_3}\right]$$

Here, a_0, a_1, a_2, and a_3 are amplitude, center, width (> 0), and shape (>1.01). The fitting results are summarized in the Table 3.1 below. The quality of the fitting is estimated from the R^2 value and is calculated to be 0.9993. The Weibull curve with using the parameters below is extrapolated down to 2140 keV (Figure 3.4 (c, magenta)). Further details of this analysis method can be found in this literature[182].

Table 3.1 Fitting results of subtracted NDP profile by Weibull function

Parameters	Fit results	Errors
a_0	5.08103×10^{16}	$\pm 3.75795 \times 10^{14}$
a_1	2412.46	± 0.72979
a_2	279.079	± 73.2746
a_3	7.79389	± 1.96886
R^2	0.9993	-

3.5.2 NDP depth profiling analysis

69

Measured triton energy can be converted to depth information by using the Transport of Ions in Matter (TRIM) software[139], which can estimate kinetic energy loss of ions passing through various matters based on Monte Carlo simulation. In the calculation, the following parameters in Table 3.2 are used as a materials stoichiometry with varied thickness value to simulate the energy loss at each depth. Thickness of each layer is quantified by FIB-SEM image in Figure 3.11 (a) that shows LNMO and LiPON are 2.74 µm and 2.24 µm, respectively. The initial kinetic energy of $^3\text{H}^+$ ion is set at 2727.92 keV and its mass is set at 3.016 amu ($\approx 5.008 \times 10^{-24}$ g). Obtained energies at each depth are average of $\approx 9,999$ particles of simulation.

Table 3.3 summarizes input depth, where the particles are generated with the initial energy, and calculated energy after tritons passing through the matters. Actual depth used in the simulation is the total depth in Table 3.3 plus thickness of the polyimide tape (≈ 7.6 µm). Simulated energy is plotted in Figure 3.11 (b) as calibration curves. Note that there are two different particles having different pathways: LNMO/LiPON/polyimide tape and LiPON/polyimide tape. The tritons generated from ^7Li in LNMO travel through LNMO, LiPON and polyimide tape while those generated in LiPON travel through only LiPON and polyimide tape. Hence, two calibration curves are needed. The deep side of the curve (red in Figure 3.11 (b)) is fitted by:

$$d(LNMO/LiPON/PI) = -1.650E^2 - 0.006E + 25.18$$

Here d and E represents depth and kinetic energy, respectively, and PI denotes polyimide tape covering surface. The shallow side of the curve (blue in Figure 3.11 (b)) is fitted by:

$$d(LiPON/PI) = -6.844E^2 - 0.019E + 50.33$$

In both fitting calculations, R^2 is 1.000, meaning quality of fitting is satisfactory.

Figure 3.11 (c) is depth profile of Li concentration converted from Figure 3.4 (b) by the calibration curves above. To convert from 2D concentration (atoms cm^{-2}) to 3D concentration

(atoms cm^{-3}), each 2D concentration is integrated by each depth step. In Figure 3.11 (c), it is apparent that Li depth profiles in LiPON and LNMO layer clearly match the observed cross-section in Figure 3.11 (a). Furthermore, Li concentration in atoms cm^{-3} is in accordance with each theoretical value, in which $L_{1.0}Ni_{0.5}Mn_{1.5}O_4$ and $Li_{2.84}P_{1.0}O_{3.35}N_{0.38}$ are 1.33×10^{22} and 3.11×10^{22} atoms cm^{-3}, respectively. At the LNMO/Pt interface around 4 µm in depth, the long slope is observed. This might be ascribed to the interdiffusion of LNMO and Pt layers, which was reported by Kim et al.[199]

As can be seen, NDP measurement clearly visualizes Li concentration in each layer and have good agreement with the results done by other characterization. At the interface between LiPON and LNMO, in contrast, an increase in Li is observed and that reached ≈ 1.5 µm deep into the LNMO layer (black in Figure 3.11 (c)). The depth range of this increase is larger than the resolution of the NDP detector (≈ 50 nm) and the roughness of the LNMO/LiPON interface (≈ 100 nm, see (S)TEM images in Figure 3.5, Figure 3.6, Figure 3.8, Figure 3.9, and Figure 3.11). The LNMO was also observed to not be porous, thus excluding the possibility of LiPON being deposited deep into the LNMO layer during cell fabrication. It is possible that this increase is a sign of overlithiation.

The profiles presented in the manuscript body are reported in units of areal concentration (Li atoms cm^{-2}) vs. energy (keV). This was done as there is known chemical and structural variability of the interface, which can cause an inaccurate conversion calculation of the profiles' scales into Li atoms cm^{-3} vs. depth (µm), respectively[183].

Table 3.2 Stoichiometry of stopping matters used in TRIM simulation[61]

LNMO (0 – 2.74 µm)		LiPON (0 – 2.24 µm)		Polyimide tape (7.6 µm)	
Li	1	Li	2.84	H	2.63
Ni	0.5	P	1	C	69.1
Mn	1.5	O	3.35	N	7.3
O	4	N	0.38	O	20.92

Table 3.3 Thickness input value and corresponding simulated energy

LNMO thickness (µm)	LiPON thickness (µm)	Total depth (µm)	Simulated energy (keV)
2.74	2.24	4.98	2159.03
2	2.24	4.24	2216.07
1	2.24	3.24	2291.43
0.5	2.24	2.74	2328.82
0.1	2.24	2.34	2358.33
0.05	2.24	2.29	2362.13
0.01	2.24	2.25	2365.16
0	2.24	2.24	2365.58
0	2	2	2376.61
0	1	1	2421.96
0	0.5	0.5	2444.73
0	0.1	0.1	2462.96
0	0.05	0.05	2465.08
0	0.01	0.01	2466.88
0	0	0	2467.28
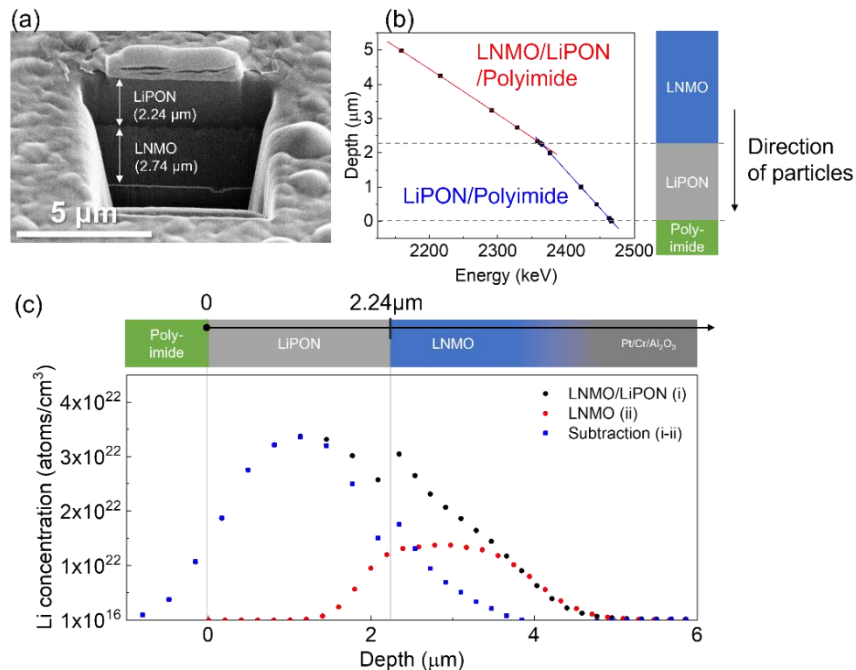
Figure 3.11 Li concentration profile analysis. (a) Cross-sectioned image of LNMO/LiPON by FIB-SEM. (b) Calibration curves for LNMO/LiPON/Polyimide tape (red) and LiPON/Polyimide tape (blue), which are used to convert the observed energy to the sample depth. (c) Li concentration profiles as a function of depth, converted from Figure 2 (b), for LNMO/LiPON (black) and LNMO (red). Uncertainty in (b) is < 2% and is based on the (1σ) standard deviations of the average energy value calculated for the particle transmitted from the defined depth position. Uncertainty bars in (c) may be smaller than the data points, is reported to 1σ, and is calculated from experimental counting statistics and known uncertainties for parameters used in the counts-to-atom concentration calculation.

3.6 Acknowledgements

Chapter 4 Elucidating Dynamic Conductive State Changes in amorphous Lithium Lanthanum Titanate for Resistive Switching Devices

4.1 Introduction

Neuromorphic device, which aims to mimic human brain and facilitate a revolutionary computing system, has attracted interests in the field, as a demand of artificial intelligence (AI) has been growing[87,200,201]. To emulate synaptic behavior, resistive random-access memory (ReRAM) is one of the promising memory devices owing to its simple metal-insulator-metal (MIM) structure, non-volatility, and low power consumption[87]. In ReRAM devices, the resistance of the material changes under an external electric field. In general, insulative materials used are high resistance state (HRS), or OFF state, at the beginning, which are switched to low resistance state (LRS), or ON state, when electrical stimuli is applied. So far, various simple oxide materials such as binary oxides (e.g. HfO_x, AlO_x, NiO, TiO_x, and SiO_x) and perovskite oxides (e.g. $SrTiO_3$) have been explored as a ReRAM device. The underlying mechanisms are proposed to be the formation of conductive filaments inside insulator, resulting in reduced resistance of the whole device[87,102,103]. However, a more comprehensive understanding of the resistive switching mechanisms is lacking for emerging smart materials.

On the contrary to fundamental study of ReRAM, all solid-state thin-film batteries are another intriguing field for both fundamental interface studies and application for micropower source[23,50,54,59–61,202]. Those battery studies share common features such as dynamic ion/defect migration (Li^+ and oxygen vacancy)[18,203,204], phase transformation under their operation[108,112,205,206], and similar architecture (electrode-electrolyte-electrode)[87,202]. Those similarities are expected to enable us to have synergetic effect on their investigation, leading to deeper understanding on both fields. Indeed, these days, knowledges acquired through battery

studies are transferred to develop new resistive switching devices. For example, Fuller et al. explored $LiCoO_2$, a popular cathode material as a potential materials for neuromorphic computing device[108]. This is ascribed to nonmetal-metal transition of Li_xCoO_2 ($0 \leq x \leq 1$) that changes its electronic conductivity by the factor of 10^6 depending on lithiation state[106]. Young et al. reported that Li-ion battery anode material, $Li_xTi_5O_{12}$ ($4 \leq x \leq 7$), exhibits significant increase in electronic conductivity by a factor of ~10^6 upon only a few percent of lithiation[112]. Not only those electrode materials, but solid electrolyte materials also has a strong potential to be a resistive switching device since it is designed to be electronically insulative at pristine state as one of the requirements.

Recently, our group has developed amorphous lithium lanthanum titanate ($Li_{3x}La_{2/3-x}TiO_3$, LLTO) thin film as a solid-state electrolyte for all solid-state thin-film batteries by using pulsed laser deposition[68], which has higher ionic conductivity ($\approx 10^{-3}$ S/cm) than a conventional thin film solid state electrolyte, such as lithium phosphorous oxynitride (LiPON, $\approx 10^{-6}$ S/cm) has. In the study, we optimized thin film deposition pressure and temperature to maximize its ionic conductivity with sufficiently low electronic conductivity. Amorphous feature facilitates ionic conduction by reducing grain boundary factor in its resistance, which had been limited LLTO with the value below 10^{-5} S/cm as a material ionic conductivity.

Beyond its application to energy storage devices, recent work on amorphous LLTO (a-LLTO) done by Shi et al. has demonstrated a memristive switching response under the stimuli of an external electric field, indicating the potential of integrating a-LLTO as a neuromorphic material for the future generation of memristors[207]. Deng et al. recently reported that LLTO shows switching behavior by the order of 10^2 and the different type of contact at the top electrode/LLTO interface and LLTO/bottom electrode cause rectifying effect in Pt/LLTO/Pt device[208]. However, composition of thin film LLTO is quite far from the original design (about 10%) and there is little

of the direct evidence about such differences at the interfaces. In their study, they tested the Pt/LLTO/Pt device up to 6 V, which is too high voltage to make it stably cycles. Therefore, despite its unique feature, the resistive switching mechanism of a-LLTO is yet to be interpreted well. Although the resistive switching mechanism might be explained by the formation of conductive pathway inside a-LLTO, lack of characterization method to identify the growth of such conductive pathway makes it difficult to elucidate the mechanism in detail due to its amorphous feature of a-LLTO (no crystalline feature) and nanoscale filament growth (too small to observe).

In this work, we demonstrate successful observation of LLTO resistive switching behavior and optimization of voltage range to achieve both restive switching and cycling stability. Furthermore, electronic conductivity changes that provoke the LLTO switching are investigated through experimental approach and the first-principles analysis. Based on the experimental and computational results obtained so far, switching mechanisms are discussed with a simplified LLTO model. At last, *in-situ* testing of LLTO nano device under focused ion beam (FIB) setup and biasing holder are demonstrated, which aims for scanning transmission electron microscopy (STEM)-electron energy loss spectroscopy (EELS) and conductive atomic force microscopy (c-AFM) to fully elucidate the switching mechanisms of LLTO.

4.2 Experimental method

4.2.1 LLTO target synthesis

$Li_{0.5}La_{0.5}TiO_3$ was synthesized through solid-state reaction, based on past study[68]. A stoichiometric amount of Li_2CO_3 (Sigma Aldrich), La_2O_3 (Sigma Aldrich), and TiO_2 (anatase, Aldrich) powders were thoroughly mixed by a high energy ball mill (Emax, Retsch) in ethanol. Before mixing powders, La_2O_3 was dehydrated at 900°C for 4 hours with a ramping and cooling

rate at 5 °C/min in a box furnace. After ball-milling and removing ethanol, the mixed powder was calcinated in an alumina crucible in a box furnace. This calcination was conducted at 1200°C for 6 hours with a ramping and cooling rate at 5°C/min. The calcinated powder was grounded in a mortar and pestle and pelletized into a 1-1/8-inch die at 10 tons for 5 minutes. The pellet was sintered at 1300°C for 5 hours with the ramping and cooling rates at 5 °C/min. After sintering, the pellet surface was polished with sandpaper.

The molar ratio of Ti to La in the synthesized target was studied by electron energy-dispersive X-ray spectroscopy (EDS) equipped with FEI Quanta FEG 250, showing 2.12±0.37 (Designed value: 2). The target was fixed on the holder for pulsed laser deposition (PLD) processing.

4.2.2 LLTO thin-film deposition and device fabrication

With the synthesized target, LLTO thin film was deposited by PLD. The deposition was conducted by 248 nm KrF Lambda Physik LPX-Pro 210 excimer laser in an Excel Instruments PLD-STD-12 chamber. The laser was set at an energy fluence ~2 J/cm^2 and 4 Hz frequency for 5000 shots during the deposition. Ni-coated SiO_2/Si wafer (MTI corporation) was used as a substrate, and the LLTO film was grown at 400°C substrate temperature under 200 mTorr of O_2 pressure. On top of the LLTO film, 9 spots of Ni current collector (~ϕ1 mm) were deposited by DC sputtering (Denton Discovery 18 sputter system, National Nanotechnology Coordinated Infrastructure).

4.2.3 Electrochemical testing

The electrochemical property of the deposited Ni/LLTO/Ni device was tested by a potentiostat with ultra-low current option, Biologic SP-200. Switching property was measured through the swept voltage at the rate of 0.04 V/sec with different voltage windows. Electronic

conductivities of the films were also measured, where current was measured by applying constant voltage at 10 mV. Then, the electronic conductivity, σ_e, were calculated through the following equation:

$$\sigma_e = \frac{\ell I}{AV}$$

Here, $\ell, A, V,$ and I are thickness of the film, area of top Ni current collector, the applied voltage (10 mV), and measured current after relaxation, respectively.

4.2.4 First-principles calculation

In order to explain the effect of ions (Li and O) on LLTO, the electronic structure of LLTO was investigated in the spin polarized GGA+U approximation to Density Functional Theory (DFT)[209]. Projector augmented-wave method (PAW) pseudopotentials were employed as implemented in the Vienna Ab initio Simulation Package (VASP). The Perdew-Bruke-Ernzerhof (PBE) exchange correlation and a plane-wave representation for the wavefunction[210] were used, where a cut-off energy was set at 600 eV. The Brillouin zone was sampled with a k-points mesh of 3×3×3 for density of states (DOS) calculations. Effective U values used through all the calculations were 5 for Ti. Cubic spinel structure (space group: $Pm\bar{3}m$), $Li_4La_4Ti_8O_{24}$, drawn by VESTA[211] was used as an initial structure and the electronic structures of LLTO with different Li and O compositions were studied to simulate each point inside biased LLTO.

4.3 Results and Discussion

4.3.1 Switching behavior of Ni/a-LLTO/Ni device

LLTO thin film was prepared by pulsed laser deposition (PLD) under the condition that our group previously optimized. Details are illustrated in 4.2.2. Then switching behavior of a-LLTO with Ni electrodes were tested and demonstrates switching behaviors when it is cycled at 0

V→ 3.5 V→ -3.5 V→ 0 V, where the device becomes HRS to LRS from 0 V to 3.5 V and becomes

LRS to HRS from 3.5 V to 0 V (Figure 4.1 (a) and inset). The corresponding current difference at

1.0 V, for instance, is three orders of magnitude, which is large enough as a resistive switching

device. Figure 4.1 (b) shows resistance vs. voltage plot, also suggesting resistance decreases during

the sweep 0 V→ 3.5 V, i.e., ON, and increases during the sweep 0 V→ 3.5 V, i.e., OFF. To figure

out the optimal voltage range, different voltage ranges are explored and compared in Figure 4.1

(c), where the ratio of end-point current to current at 1.0 V as a reference point. Here end-point

current is defined as the current value at highest voltage in each voltage range. For example, when

the device was cycled at the range of -3.5 V $\leq$ V $\leq$ 3.5 V, end-point current is the one at 3.5 V. As

can be seen, when the voltage range is -3.0 V $\leq$ V $\leq$ 3.0 V or smaller, the current ratio is 10^2 order

of magnitude while the current ratio become 10^3 when the voltage range is -3.5 V $\leq$ V $\leq$ 3.5 V or

larger. In Figure 4.2 and Figure 4.3, I-V curves at different voltage range are demonstrated as

linear-linear and log-linear plot, respectively. At lower voltage range (e.g. -2.5 V $\leq$ V $\leq$ 2.5 V), its

I-V curve is like "butterfly-shape" and different from the one at higher voltage range shown in

Figure 4.1 (a). Similar I-V behavior was observed in the study by Deng et al.[208] and Kim et al.[212],

implying the resistive switching is not activated at this lower voltage range. Thus, these results

show that the device needs certain amount of voltage to turn on the resistive switching, i.e. around

3.5 V in above case.
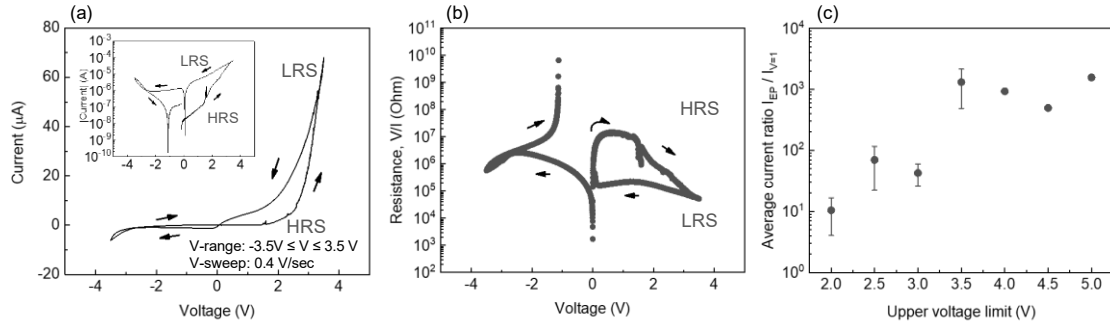
Figure 4.1 Electrical response of Ni/LLTO/Ni thin film. (a) Linear I-V plot of LLTO, where voltage is swept between -3.5 and 3.5 V (a-inset) log |I|-V plot. The voltage is swept at the rate of 0.4 V/sec. (b) Resistance (V/I) vs. V plot. (c) Average ratio of current at the highest voltage in the different voltage range, I^{EP} (EP: end-point), to current at V = 1.0 [V] in the first cycle. For example, when voltage is swept between -3.5 and 3.5 V, upper voltage limit is 3.5 V and I^{EP} is the current value at 3.5 V.
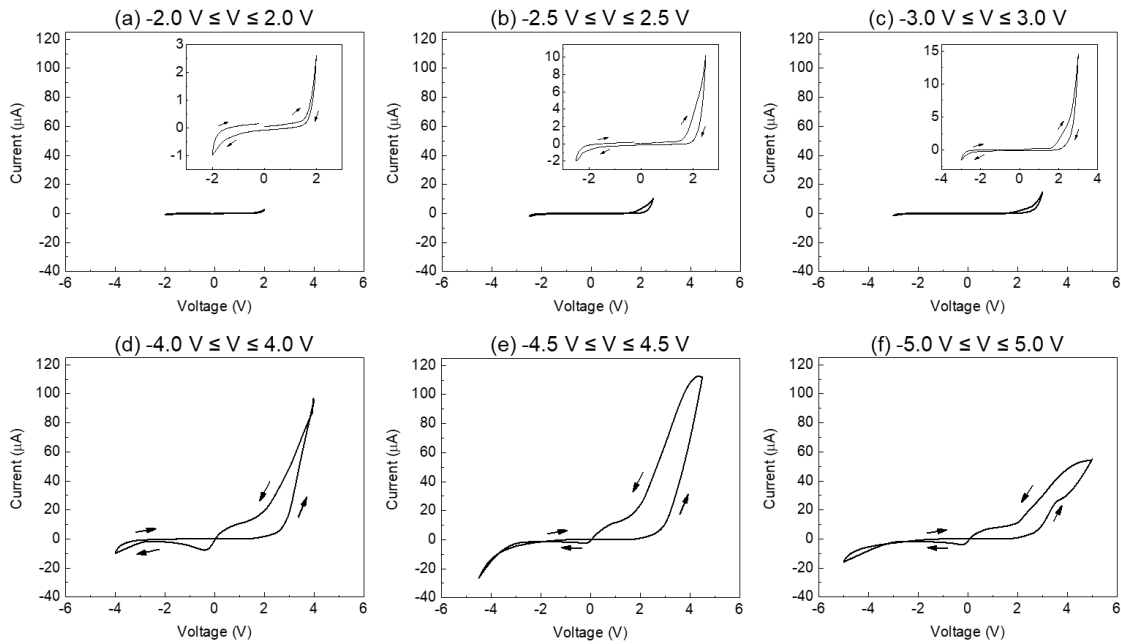
Figure 4.2 Linear I-V plot in different voltage range. (a) $-2.0\ V \leq V \leq 2.0\ V$, (b) $-2.5\ V \leq V \leq 2.5\ V$, (c) $-3.0\ V \leq V \leq 3.0\ V$, (d) $-4.0\ V \leq V \leq 4.0\ V$, (e) $-4.5\ V \leq V \leq 4.5\ V$, and (f) $-5.0\ V \leq V \leq 5.0\ V$. Inset figures in (a), (b), and (c) are magnified images of respective plots.

80
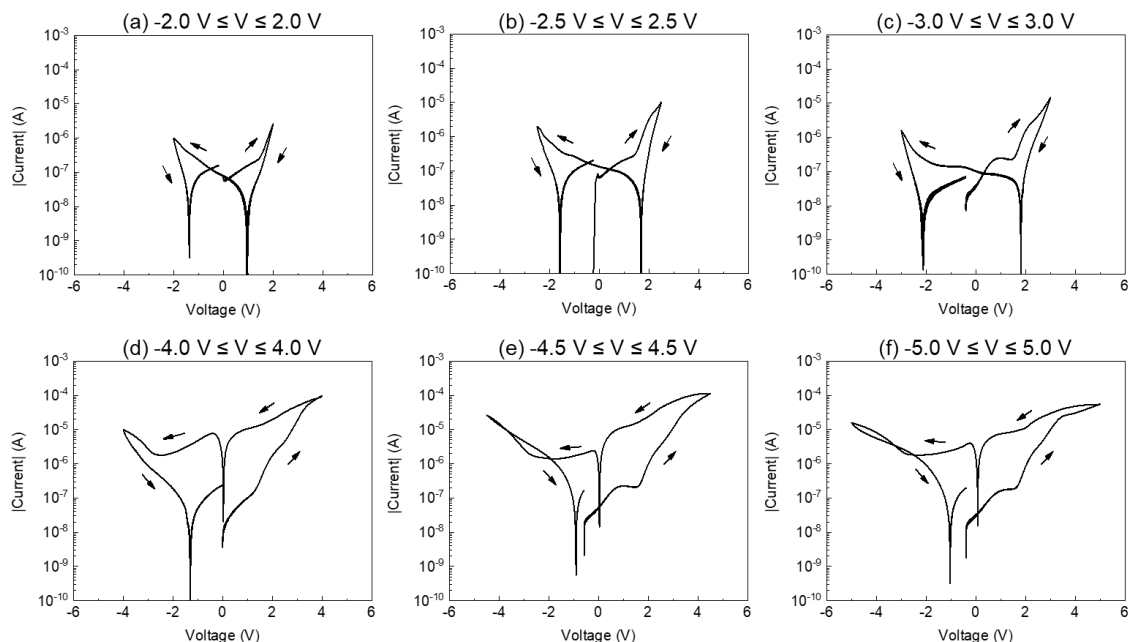
Figure 4.3 Log |I|-V plot in different voltage range. (a) -2.0 V $\leq$ V $\leq$ 2.0 V, (b) -2.5 V $\leq$ V $\leq$ 2.5 V, (c) -3.0 V $\leq$ V $\leq$ 3.0 V, (d) -4.0 V $\leq$ V $\leq$ 4.0 V, (e) -4.5 V $\leq$ V $\leq$ 4.5 V, and (f) -5.0 V $\leq$ V $\leq$ 5.0 V. These are log |I| plot from Figure 4.2. The absolute value of the current in Figure 4.2 are used to make these plots.

The durability of the devices cycled at different voltage ranges are studied as well. In Figure 4.4, responding end-point current are plotted as a function of cycling numbers. Figure 4.4 shows that when the device is cycled at high voltage range such as 4.5 V and 5.0 V, the current change over cycling is significant. This is because the voltage range goes above the voltage stability window of LLTO. Zhu et al. has calculated the electrochemical window by density functional theory (DFT) that is within 1.8 - 3.7 V[55]. Therefore, the device is not stably cycled at high voltage range, even though it shows resistive switching behavior. In Figure 4.5, TEM images of a-LLTO before and after biasing to 5.0 V are displayed. While pristine a-LLTO shows amorphous feature in the magnified image and its FFT pattern (Figure 4.5 (c) and its inset), in the a-LLTO after biasing, a periodic feature is partially observed, as shown in Figure 4.5 (e). FFT analysis tells that this feature has 2.98 Å spacing and equivalent to the crystalline of $La_2Ti_2O_7$ [213], which might be a sign that too high voltage causes the decomposition of a-LLTO.

In summary of the discussion on lowest and highest limit of the voltage range, within the voltage stability window of a-LLTO, the higher voltage than 3.0 V should be selected to make the difference of the current at HRS and LRS as distinguishable as possible. If the voltage is too small, the device does not show switching behavior, as we discussed above. If the operating voltage is too high, such as 4.5 V or higher, a-LLTO is decomposed. As such, in order to retain distinguishable resistive switching and relatively good cycling stability of the device, a voltage range of -3.5 V $\leq$ V $\leq$ 3.5 V should be used for the a-LLTO device.
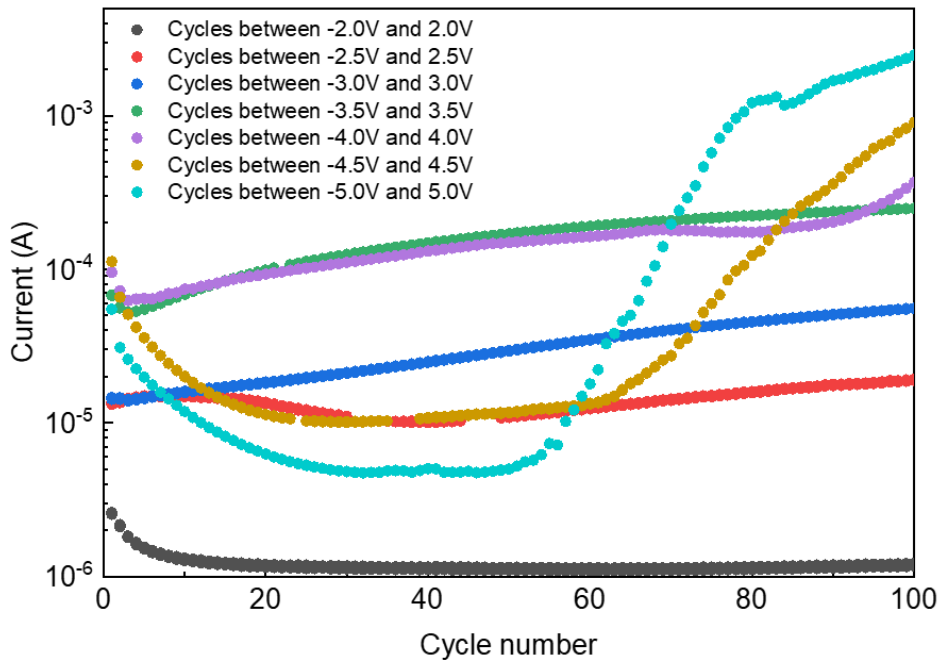
Figure 4.4 Cycling stability of Ni/LLTO/Ni system. End point current vs. cycle number. For example, current at 3.5 V when voltage is swept between -3.5 and 3.5 V (= end-point current) is used as a current value in the plot.
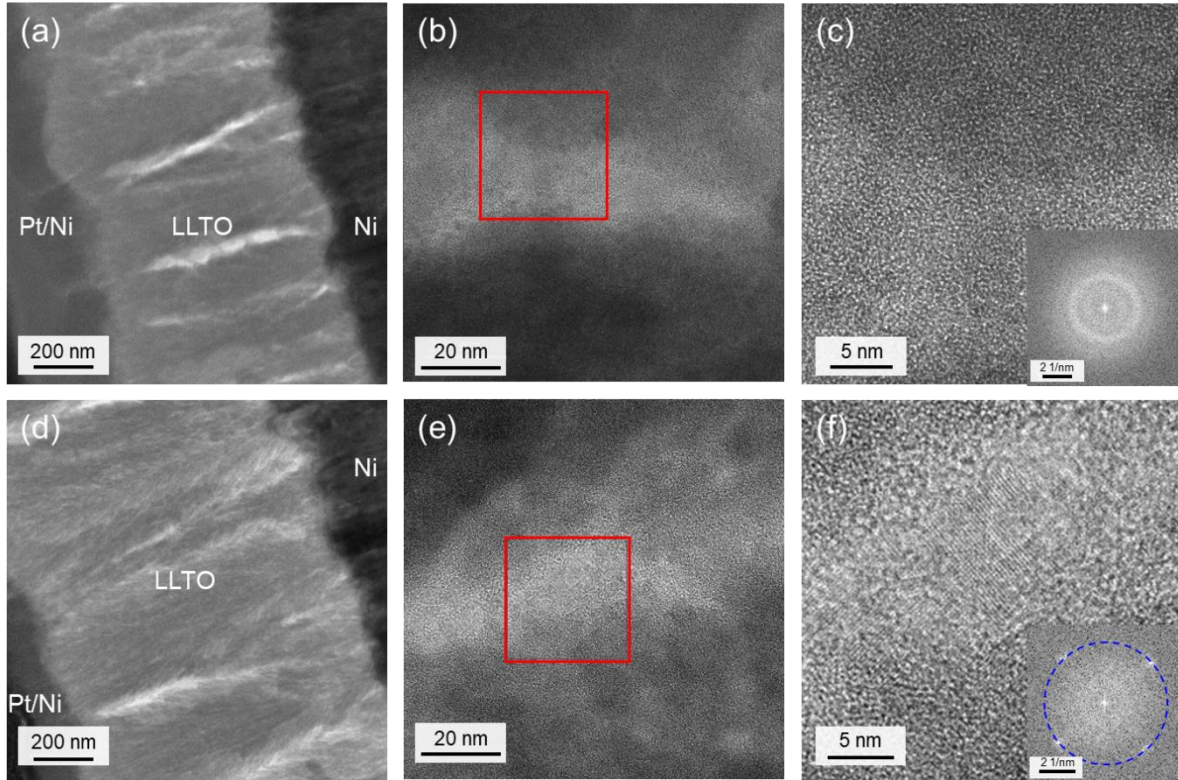
Figure 4.5 TEM images of pristine and after-biasing state of LLTO. (a) Zoom-out and (b) magnified TEM images of pristine LLTO. (c) Further magnified images of the area surrounded by red square in (b) with (inset) FFT image. (d) Zoom-out and (e) magnified TEM images of LLTO after biasing up to 5 V. (c) Further magnified images of the area surrounded by red square in (e) with (inset) FFT image. Periodic pattern is found in its FFT image, which is equivalent to the structure with d-spacing at 2.98 Å.

4.3.2 Effect of O vacancy on electronic conductivity

When a-LLTO is under electrical biasing, O^{2-} ions are migrated to positive side due to Coulombic attraction. The microscopic composition of LLTO under biasing is speculated to show gradational changes across the thickness direction, in which LLTO becomes O-rich on positive side and O-poor on negative side (Figure 4.6 (a) left). To explore the effect of the different oxygen composition on the electronic conductivity, a-LLTO thin films were deposited at various O_2 partial pressures during PLD process. Figure 4.6 (b) shows the change of electronic conductivity with O_2 pressures. There appears to be a critical O_2 pressure around 0.08 mbar, where the electronic conductivity of a-LLTO film changes drastically by more than 5 orders of magnitude. LLTO films

deposited above the critical O_2 pressure are insulative while the films under this point are much more conductive, which is attributed to the introduction of O-vacancy into a-LLTO (O-poor LLTO). Our past study by Lee et al. discussed that when O-vacancies form in LLTO, Ti^{4+} cations are reduced to Ti^{3+} for the charge compensation, and, consequently, electron conduction pathway is formed[68].
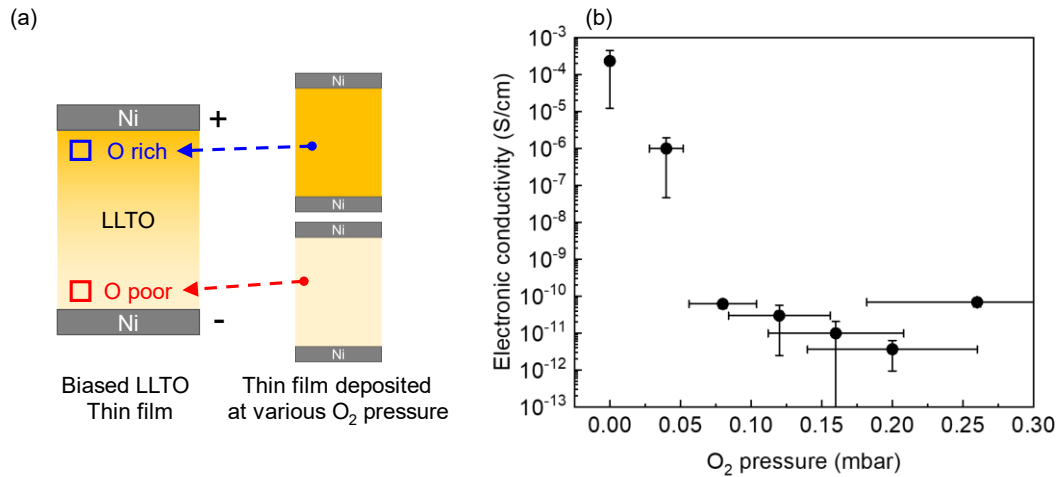
Figure 4.6 Electrical conductivity dependency of a-LLTO. (a) schematic illustration of (left) biased a-LLTO and (right) thin film deposited at various O2 partial pressure to demonstrate local composition in biased LLTO film. (b) Electronic conductivity vs. O_2 deposition pressure during PLD. The horizontal error bar is attributed to the accuracy of the pressure gauge, which is $\pm 30\%$. The vertical error bar is from statistics of multiple measuring points on one sample.

As Li^+ migrates to the negative side when O^{2-} migrates to the positive side upon biasing in a-LLTO, DFT calculation is employed to interpret its electronic structure at different composition to further simulate the effect of both Li and O across LLTO composition. Here we employ crystalline LLTO to simplify calculations. Starting with cubic LLTO structure with 4 Li atoms, 4 La atoms, 8 Ti atoms, and 24 O atoms (Figure 4.7 (a)), LLTO composition is changed to simulate when various Li and O contents are present. In the electronic structure calculation, three different O compositions that contain 24 O atoms, 23 O atoms and 22 O atoms were simulated, corresponding to 0%, ~4.2 %, and ~8.3 % of O vacancy, respectively. Similarly, the number of Li

atoms were changed from 1 to 4 in the LLTO structure. Figure 4.6 (c) summarizes the band gap values of LLTO with different compositions obtained from each electronic structure (e.g., Figure 4.7 (b)), where LLTO shows two major categories – the conductive phase (green) and insulative phase (red). In the structures where Li content is stoichiometric or deficient, LLTO band gaps decrease, indicating the increase of electronic conductivity with more O-vacancies. This has a good agreement with the results of the electronic conductivities of LLTO film deposited at different O_2 pressures, suggesting that O-vacancy could serve as the key to induce conductivity change and the resistive switching. In the structure that contains 23 O atoms, the band gaps experience an increase and subsequent decrease as Li content is reduced, implying that not only O but also Li composition influences the electronic structure of LLTO. As exemplified TiO_2, TiO_{2-x}, and Ti_2O_3[214–216], presence of oxygen vacancy triggers Ti reduction, leading smaller bandgap. In TiO_2, all Ti is theoretically Ti^{4+} ($3d^0$) and bandgap forms between filled O 2p orbital and empty Ti 3d orbitals. Once oxygen vacancy introduced to the system, TiO_{2-x} forms oxygen vacancy state between the valence and conduction band and bandgap becomes smaller. When Ti is fully reduced to Ti^{3+} ($3d^1$) in Ti_2O_3, Ti 3d orbitals are partially occupied and its bandgap appear between Ti 3d orbitals with 0.1 eV gap. As experimentally shown in the results in Figure 4.6 and the past studies[68,217], oxygen vacancy can be a trigger to cause Ti reduction. In contrast to oxygen vacancies, many researches aiming for LLTO as an electrolyte materials in contact with Li metal anode prove that Li insertion into LLTO can be the other cause that induces Ti reduction[218–220]. Such study shows once LLTO is in contact with Li metal, Ti is spontaneously reduced from Ti^{4+} to Ti^{3+} and changes its electrical properties.
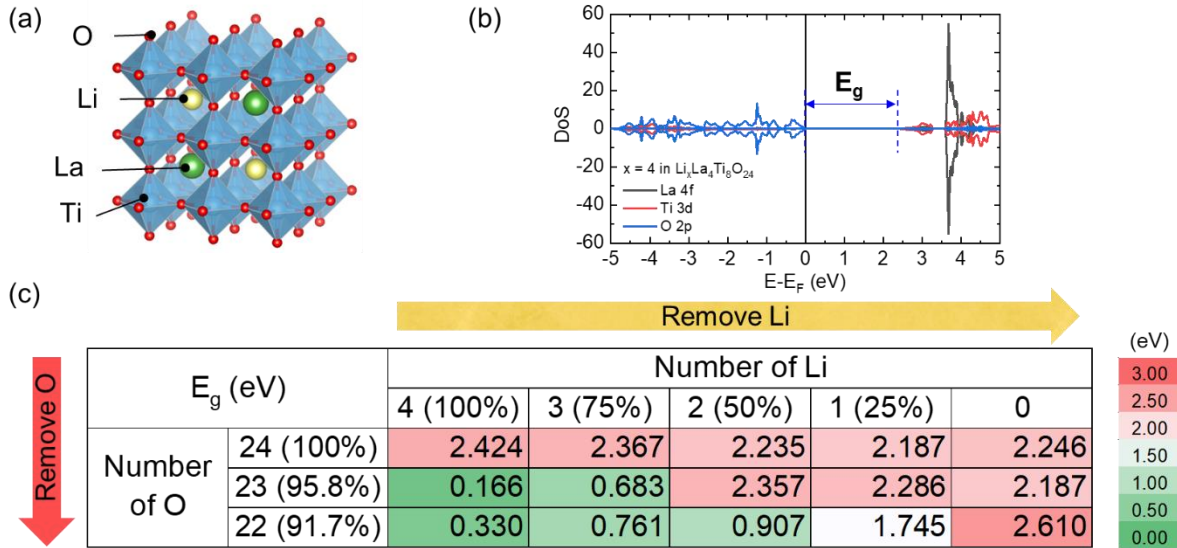
Figure 4.7 Computational analysis on bandgap of LLTO with different Li and O composition. (a) Structure of $Li_4La_4Ti_8O_{24}$ that is used for DFT calculation. (b) Electronic structure of pristine LLTO ($Li_4La_4Ti_8O_{24}$). (c) Summary of LLTO bandgap with different Li and O compositions, in which green represents zero (conductive) and red represents three (semi-conductive or insulative)

4.3.3 Discussion - Switching mechanism of a-LLTO

Through experimental and computational approaches, LLTO could have two states (conductive and insulative states) with different conductivities that trigger several orders of resistance change in the device during biasing. Here we discuss how those two states are anticipated to be distributed to affect conductivity changes, using macroscopic, simplified binary system. Figure 4.8 displays the electronic conductivity change with the portion variations of two states in LLTO. Schematics in Figure 4.8 depict two different scenarios: a series and parallel connections of resistors. If the conductive and insulative states are separately distributed across the thickness such as Figure 4.8 (a), which is equivalent to a series connection, dramatical conductivity change cannot occur unless the conductive layer become over 95% of the whole film. In contrast, Figure 4.8 (b) simulates conductive state that forms filament, bridging one electrode to the other side. In such configuration, several orders of magnitude differences can be easily achieved. In order to have more than 10^2 order difference in conductivity under biasing, conductive

filament growth is therefore necessary. According to Figure 4.8 (b), filament diameter (in total) is expected to be ~10 μm in diameter to have 10^2 order difference in the conductivity, assuming total area of the top electrode is 1 mm in diameter. This simple calculation offers guidance towards an experimental approach to identify filament growth for the next-stage investigation.
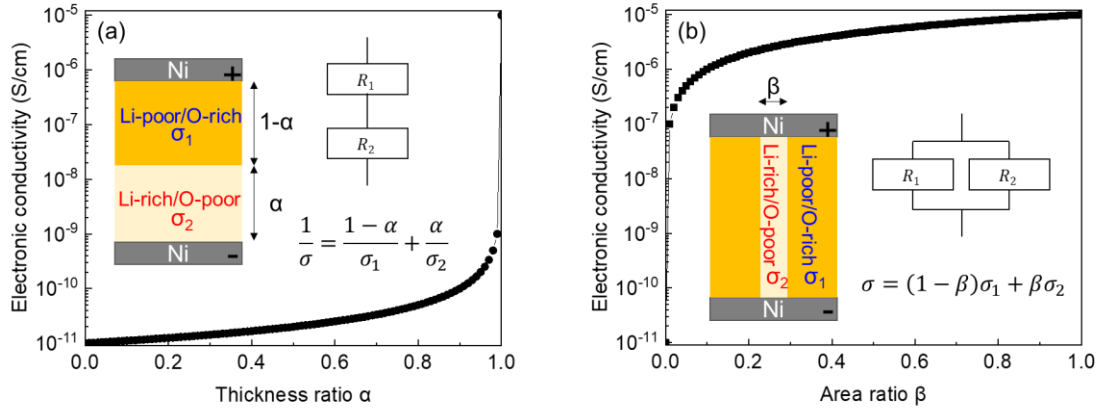
Figure 4.8 Thought experiment to explain resistive switching mechanism with simple binary system. (a) Scenario 1: two LLTO states exist as serial circuit, where α represents thickness ratio of conductive (Li-rich/O-poor) state to the whole thickness. (b) Scenario 2: two LLTO states exist as parallel circuit, where β represents cross-sectional area ratio of conductive (Li-rich/O-poor) state to the whole cross-section area. (inset for each figure) schematic illustration of assumed system, equivalent circuit, and formula of combined conductivity. Here, electronic conductivity of Li-poor/O-rich state σ_1 and that of Li-rich/O-poor state σ_2 are 1×10^{-11} S/cm and 1×10^{-5} S/cm, respectively, which is based on experimental data in Figure 4.6.

With simplified calculation, it is found that the filament growth is critical to cause resistance jump by several orders of magnitudes under electrical biasing. Herein, we further investigate how such filament grows inside LLTO. When LLTO is biased, charged mobile ions, i.e. lithium and oxygen vacancies, migrate to the negative side. The migrated oxygen vacancies might be accumulated there like Figure 4.9 (b) and change local composition to form conductive state of LLTO, in which electrons can freely move inside, as shown in Figure 4.9 (d). At the tip, electron from conductive LLTO and oxygen vacancy from insulative LLTO form another oxygen vacant LLTO under the reaction (Figure 4.9 (d) right), where LLTO lose some oxygen and Ti is partially reduced from 4+ to 3+ due to charge compensation. Thus, a new conductive layer of

LLTO forms. By repeating this reaction, conductive filament reaches to the other side of the electrode Figure 4.9 (c)). Repulsion force from negative electrode to oxygen vacancy ions are the strongest when the filament is about to reach the other side of electrode. Therefore, there needs to be enough external driving force, that is voltage, to migrate positively charged oxygen vacancy. Otherwise, switching is not achieved. Oxygen vacancy formation energy calculation in Figure 4.10 suggests that this O-deficient LLTO should not be energetically favorable. Furthermore, as demonstrated in Figure 4.11, DC bias testing implies that ON state is spontaneously relaxed after releasing switching voltage. These explain that the filament does not remain after releasing voltage because of ion relaxation.

As battery materials, electrolyte has been developed as electronic insulator and ionic conductor while cathode and anode materials has been as mixed ionic-electronic conductor (MIEC). Thus, these materials have a strong potential to be applied to resistive switching active materials, which is triggered by ion migration. Based on the discussion so far, some guidelines for battery materials application to future resistive switching device can be proposed. First, materials should have electronic conductivity change by ion composition change such as lithium or oxygen vacancy. Ionic conductivity plays a role here to determine switching speed. Another point is stability. The material should have meta-stable state or another phase to keep the conductive filament long even after removing external stimuli to make non-volatile device.
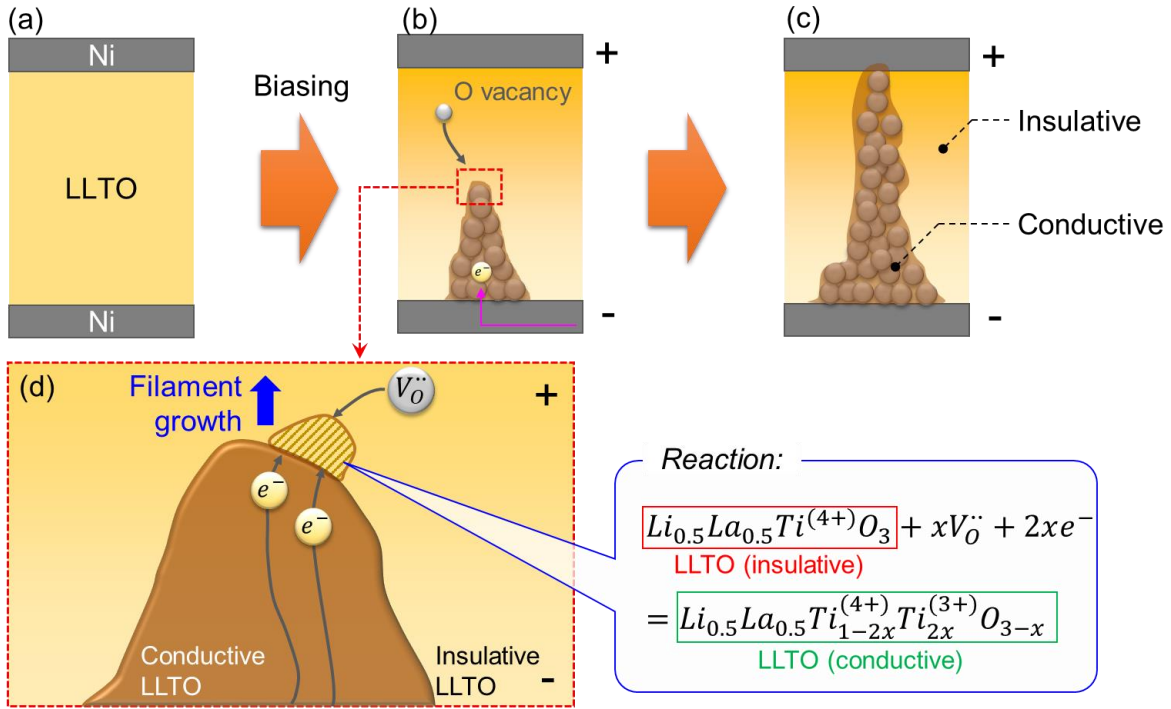
Figure 4.9 Schematic illustration of filament growth inside LLTO. (a) Pristine LLTO where all the mobile ion components (Li and O vacancy) are equally distributed. (b) Initial state of biased LLTO, where conductive filament start to grow from negative electrode. (c) Biased LLTO, where conductive filament connect from negative to positive side of electrodes and lower the total conductivity. (d) Magnified image of conductive filament tip in (b). On the tip of the filament, electrons can reach through the filament and O vacancies are collected through the insulative LLTO state. The reaction happens as expected (right) to form conductive LLTO, leading to growth of the filament.

$$E_{Ov}^F = E\left(Li_{x/8}La_{0.5}TiO_{3-y/8}\right) + \frac{y}{16}E(O_2)$$
$$- E\left(Li_{x/8}La_{0.5}TiO_3\right) - \frac{y}{16} * 1.36$$
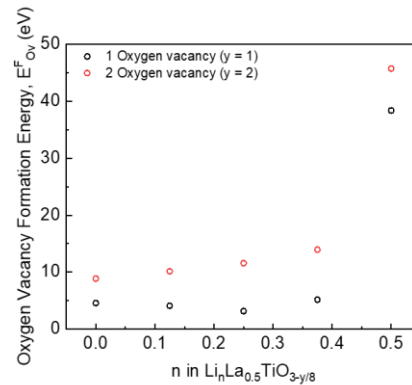
Figure 4.10 Oxygen vacancy formation energy. (a) Formula to calculate oxygen vacancy formation energy per unit formula. Here x and y represents number of lithium and oxygen atoms in supercells, respectively, that are used in DFT calculation.
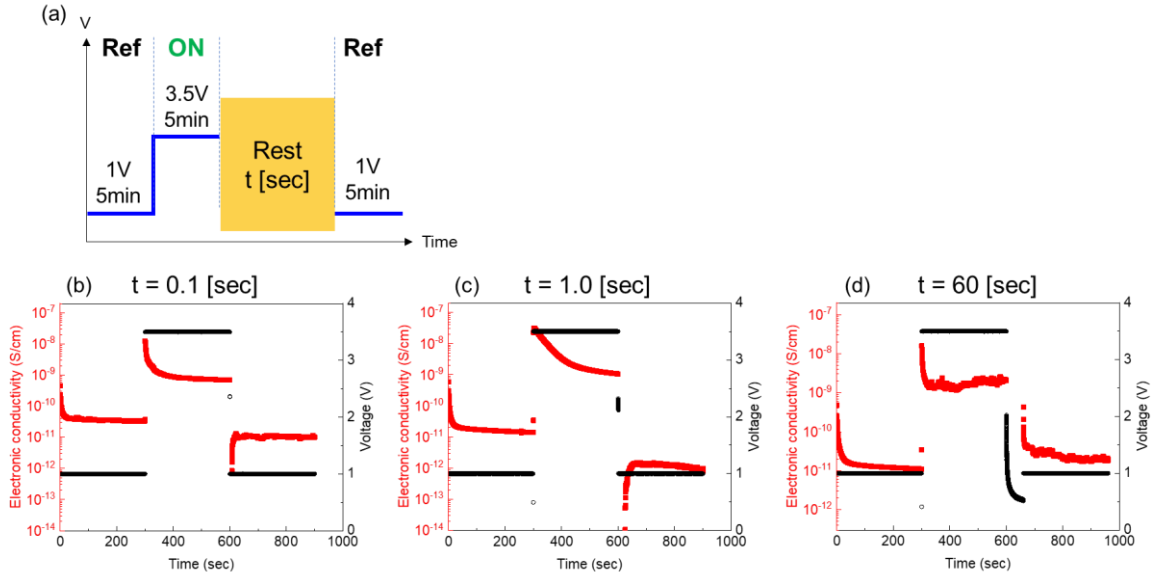
Figure 4.11 DC polarization test of Ni/LLTO/Ni. (a) Testing protocol of the device. DC polarization results with different rest time: (b) t = 0.1 [sec], (b) t = 1.0 [sec], and (c) t = 60 [sec]. Here cross-section area and thickness are ≈ 0.01 cm^2. The thickness of sample used in (b), (c), and (d) are measured as 355, 309, and 426 nm, respectively.

4.4 Conclusion

In this work, we have confirmed that Ni/LLTO/Ni demonstrates the resistive switching behavior, where significant current changes happen during voltage sweeping. To have an optimal switching, the voltage range needs to be considered. Too high voltage causes LLTO decomposition, resulting in the degradation of the device after long term cycling. In contrast, too low current cannot turn on the switching. The electronic conductivity increase might be attributed to the gradational composition difference inside LLTO. Oxygen vacancy plays an important role in terms of electronic conductivity, according to the experimental result that O-deficient LLTO become highly conductive due to the reduction of Ti^{4+} to Ti^{3+}. Computational study exploring electronic structure of LLTO with different Li/O compositions well supports the experimental results. The thought experiment to calculate the combined electronic conductivity of conductive and insulative LLTO states with two scenarios, series and parallel connection. This study shed

light on the presence of "filament growth" inside the resistive switching device to cause several orders of magnitude change in resistance under biasing.

4.5 Future Work

In this chapter, resistance change of a-LLTO under biasing and its mechanism due to filament growth have been discussed. To enable a direct observation of the conductive filaments, we have fabricated nanodevice on a chip that is specially designed for *in-situ* transmission electron microscopy (TEM) under electrical biasing and tested its electrical response inside a focused ion beam scanning electron microscopy (FIB-SEM). Nanodevice preparation is depicted in Figure 4.12 (a). A lamella consisting of Ni/LLTO/Ni layers was lifted out from thin film device and mounted onto the biasing chip, where Pt was used to bond the lamella for the physical contact to the chip and serve as the top conducting layer for the electrical contact. Then parts of top and bottom electrodes were cut off to isolate negative and positive electrode and guide the current flow through LLTO (Figure 4.12 (a)). Figure 4.12 (b) demonstrates the final configuration after nanodevice preparation. Once the nanodevice is prepared, it is tested inside FIB-SEM without air or any inert gas exposure, where a potentiostat is connected to the SEM chamber for the electrical biasing purpose. Since the cross section of current pathway is significantly small in the nanodevice, Pt and Ni layers are subjected to melting and bubbling due to the joule heat generated by abrupt electrical stimuli (Figure 4.12 (b) inset image). Therefore, to avoid such breakdown, a constant current flow is accurately controlled in the nanodevice testing. Figure 4.12 (c) shows voltage response of the device under each constant current. The voltage response of the nanodevice is similar to the bulk device results obtained by voltage sweeping (Figure 4.12 (c) inset image). Furthermore, to visualize resistance change, differential resistance is calculated and plotted as a

91

function of the voltage in Figure 4.12 (d), which shows that the resistance of the device experiences a dramatic decrease between 0.1V and 1V. This clearly implies that the device turns onto a "ON" state by applied high current/voltage. For future work, we bring the fabricated nanodevice into TEM to observe filament growth under electrical biasing by microscopic and/or spectroscopic method.
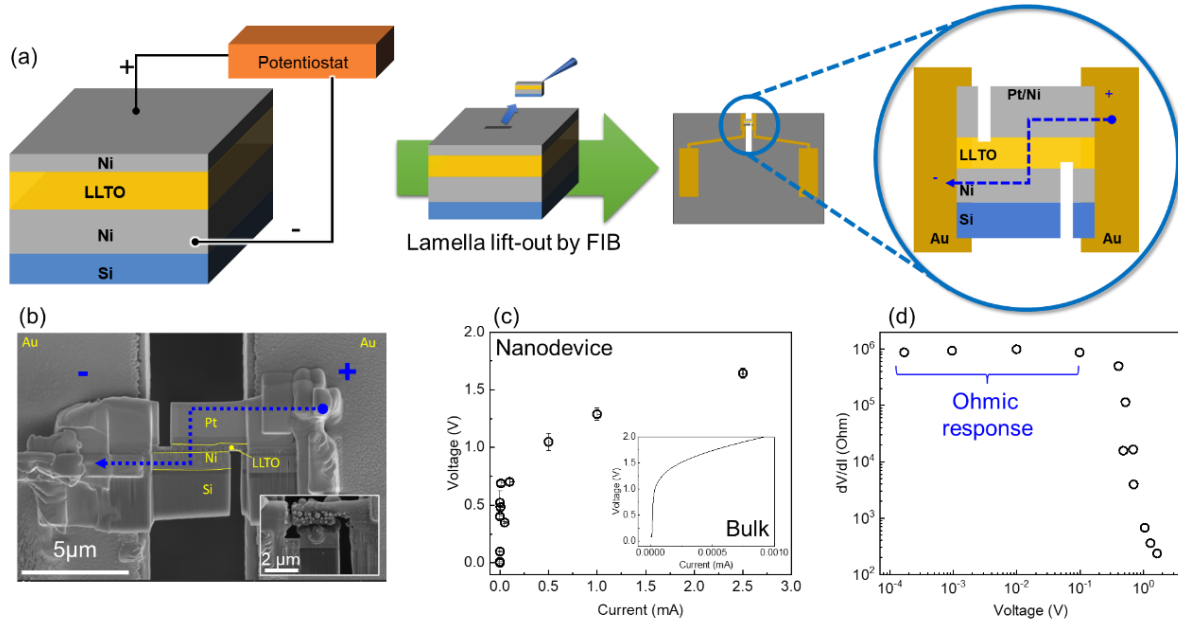
Figure 4.12 *In-situ* biasing design in FIB-SEM and testing results. (a) Experimental configuration of bulk Ni/LLTO/Ni device and nanodevice fabrication inside FIB-SEM on a biasing chip. (b) SEM image of the fabricated nanodevice, where Pt is deposited in FIB as an additional conductive layer and bond for lamella to chip. (b inset) SEM image of nanodevice with breakdown of Pt layer due to abrupt current flow. (c) V-I plot of constant current bias testing with comparison to the bulk device result (inset). (d) Differential resistance, dV/dI, vs. measured voltage, calculated from (c).

4.6 Acknowledgements

Chapter 5 Future Perspectives

In the chapters above, thin film format is proven to be a strong platform to deepen understanding of materials' properties in batteries and beyond. This is because thin film materials can be additive-free and have a flat uniform surface, compared to conventional cast bulk electrodes. Furthermore, multiple layers of thin films can achieve atomic level contacts and demonstrate distinct interfaces, which helps us to interpret morphology and chemistry at the interface. Finally, such thin film platforms have more potential to be transported to or combined to other fields such as resistive switching devices. In this chapter, the future of thin film study will be discussed with some examples. Based on its characteristics, there are three stages for the use of thin film, as shown in Figure 5.1: (1) for fundamental study as a pure material; (2) for interface study between multiple layers; (3) beyond lithium-ion batteries.
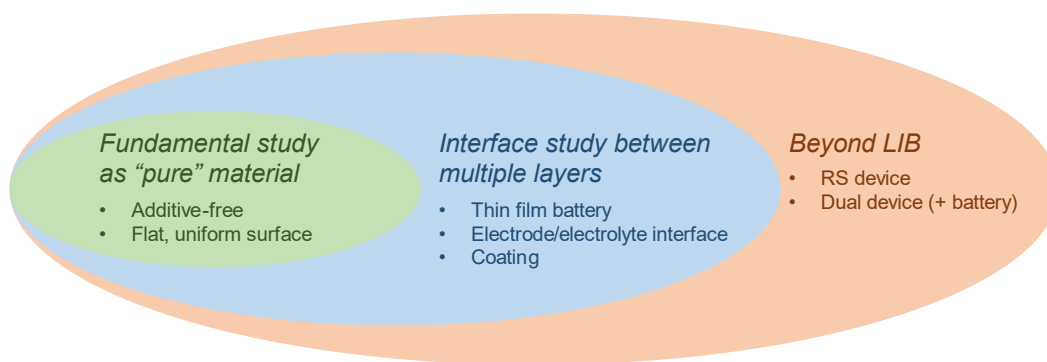
Figure 5.1 Schematic image of use of thin film materials: from material level to system level. From left to right categories, it represents more complexity or more types of materials in their systems.

5.1 Thin film as a "pure" material for its fundamental study

To fully understand reactions inside a battery, it is necessary to study electrode or electrolyte level after disassembling cycled coin cells or pouch cells. However, electrodes consist of not only active materials but also binder and conductive carbon as additives[221,222], which support active materials, such as cathode powder, with more conductivity and adhesion onto current collector. They are not involved in battery reactions but may cause side reactions that reduce

battery capacity and negatively affect the performance[196,197,223]. For instance, composite electrode including high voltage cathode material LNMO suffers from the decomposition of electrolyte due to its highly oxidative environment, forming cathode electrolyte interphase (CEI) involving Li and Mn in its layer. Thus, it is important to identify surface chemistry of the CEI layer and to find where it comes from (cathode, carbon, binder, etc.) by comparing thin film pure material and cathode composite so as to figure out degradation mechanism of high voltage system. Additive-free feature also helps characterization. Typical polymer binder, polyvinylidene fluoride (PVDF) gives signal at 688 eV in the F1s spectrum in x-ray photoelectron spectroscopy (XPS), which overlaps with signals from reaction products with electrolyte salt $LiPF_6$. This makes it complicated to quantitatively characterize chemistry of cycled electrode surface[224]. As demonstrated in Figure 5.2, comparison between thin film (additive-free) and composite electrode (with additives) provide clear difference in spectra deconvolution, enabling quantitative identification of surface chemistry. This method should be universally powerful to analyze surface chemistry of the composite electrodes, in particular, in the case of electrolytes containing fluorine. Recently researchers reported that fluorinated electrolyte or additive is effective to stabilize high voltage system due to its high reduction potential than conventional carbonate-based electrolyte[225–232], where reaction from fluorinated molecules and its biproduct must be distinguished from F from PVDF. As discussed above, thin film format is significantly useful as a single pure material and applicable regardless of cathode or anode components.
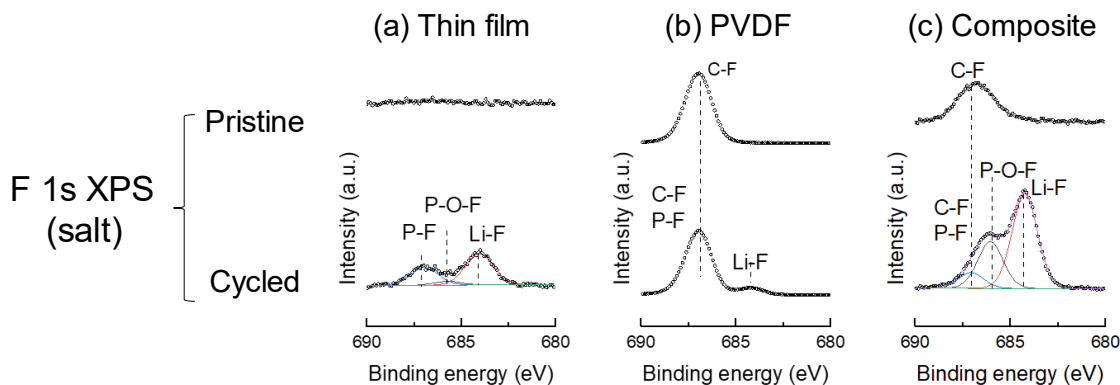
Figure 5.2 F1s XPS spectra of (a) LNMO thin film, (b) PVDF and (c) composite electrode. All the components cycled in EC: EMC = 3: 7 wt% with 1 mol L 1 LiPF$_6$ coupled with Li metal, representing as "Cycled" in the figure. Composite electrode consists of 90% LNMO, 5% conductive agent, and 5% binder. Thin film sample preparation and electrochemical cycling are done by the dissertation author. The other samples preparation, electrochemical cycling, XPS data collection, and spectral analysis are credited to Weikang Li.

5.2 Thin films for interface study

As one more step further from single material thin film, multilayered thin films have more variety of usage. The simplest model is a two-layer system, where chemistry and morphology change due to contact with each other can be studied. In the case of battery, this is equivalent to pristine electrode/electrolyte interface or interface between coating material and coated electrode particles. Thin film is a useful format to study coating/coated materials since, in the actual system, coating is not conformally achieved due to random shape of coated particles. If there are more than three layers stacked, battery or electrical device can be made, exemplified as Pt/LNMO/LiPON/Li/Cu in Chapter 3 and as Ni/LLTO/Ni in Chapter 4. With those samples, it is possible to investigate electrochemical reaction at the interface by *ex-situ*, *in-situ* or *operando,* compared with chemical reactions. In the following paragraphs, specific examples (Li/LiPON interface) and methods (in-situ biasing) that are benefitted by thin film plat form will be discussed.

5.2.1 Li/LiPON interface

In Chapter 3, LNMO/LiPON/Li cell have been tested for long-term cycling (Figure 3.3) and, its Coulombic efficiency was around 99.8% on average, which represent good, stable feature

of the system but also means that active lithium has been slightly lost every cycle. As LNMO/LiPON interface does not show any sign of degradation and CEI formation over 500 cycles, the reaction involving Li might happen on the other side, i.e. Li/LiPON interface. Indeed, Li and LiPON are reported to chemically interact and form an intermixed layer as an interphase. Cheng et al. from our group has observed that at the pristine Li/LiPON interface (i.e., no electrochemical reaction), 76-nm-thick interphase layer forms, consisting of Li_2O, Li_3N, Li_3PO_4.[61] Hood et al. also confirmed similar result that interphase layer with around 60 nm thick develops on LiPON surface when in contact with Li metal[233]. Although the development of cryo technique protected LiPON, which is beam-sensitive material[45,234], and enabled to observe pristine Li/LiPON interface as listed above, little research has been done to explore what Li, LiPON and its interphase experience under electrochemical testing. One of the challenges to obtain the cycled Li/LiPON interface is thought to be complexity of the cell fabrication. In the case of our LNMO/LiPON/Li cell, multiple deposition methods are needed: Pt was deposited by DC sputtering, LNMO was by PLD, LiPON was by RF sputtering, and Li was by thermal evaporation. The more layers and methods have in the system, the more risk of air exposure and short-circuit increases, leading to a low success rate of the cell.
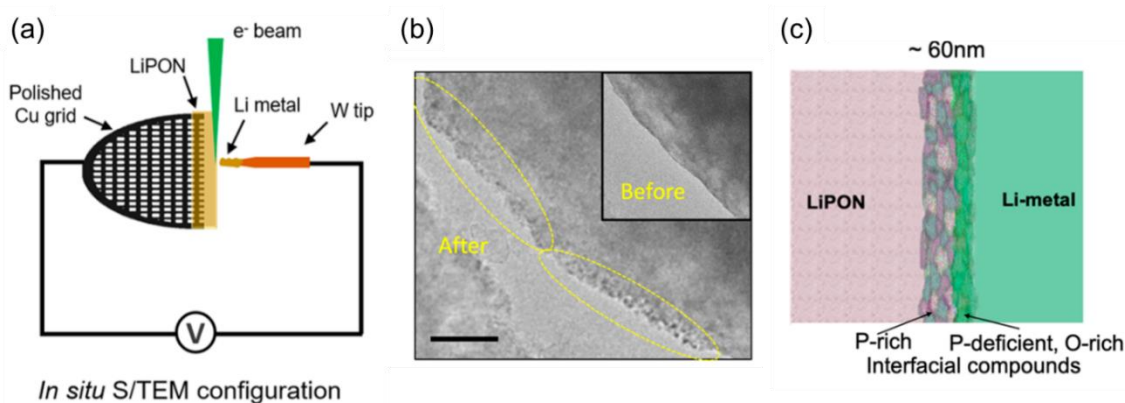
Figure 5.3 Interphase formation at Li/LiPON interface. (a) Experimental setup, (b) TEM images of LiPON surface in contact with Li, and (c) schematic representation of the interphase formation at the interface[233].

To address such an issue, a new thin film cell and its cycling apparatus are proposed and invented, which are simpler than ones conventionally used in past research. Figure 5.4 explains a new cell, in which Cu, LiPON, and Li are deposited on Al_2O_3 substrate, and its experimental setup, which has demonstrated stable plating and stripping reaction with current density at 1.0 mA/cm^2 at maximum without soft short circuit. Absence of complex oxide cathode layer makes sample preparation easy and free from concern about proper composition transfer in the cathode.
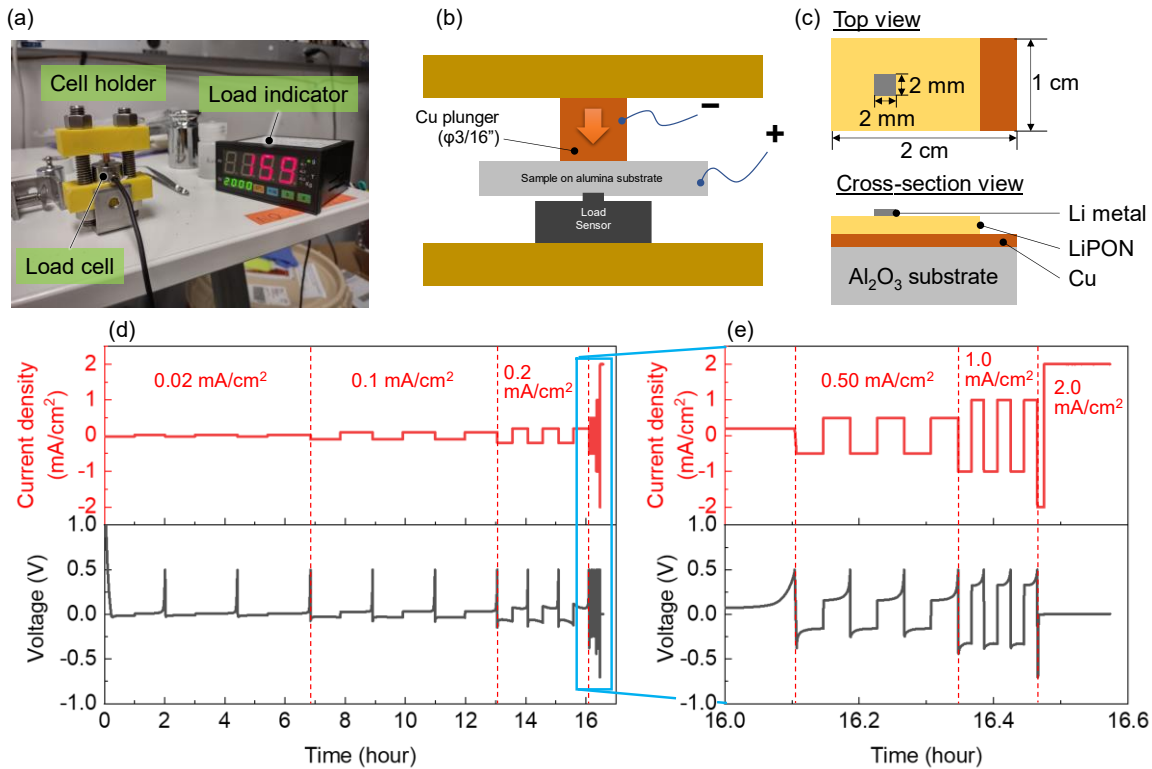
Figure 5.4 Pressure-controlled Cu/LiPON/Li cell and its setup. (a) Photograph of the experimental setup for holding thin film cell and load monitoring apparatus. Schematic illustration of (b) pressure setup and (c) configuration of Cu/LiPON/Li cell. (d) Voltage curve vs. time, and magnified image (e), where current density is set from 0.02 to 2.0 mA/cm^2. Plating is stopped at either 0.02 or 0.1 mAh/cm^2 of plating and voltage cutoff in stripping was set at 0.5 V. Pressure at around 1.1 MPa is applied to the cell.

As well as this cell can provide cycled Li/LiPON interface for ex-situ measurement, it also makes the pressure study possible. Upon Li plating/stripping on Cu, past studies claim the importance of uniaxial pressure regardless of electrolyte type, liquid[235–242] or solid[195,243–247], to obtain conformal Li deposition. Despite those examples since 1990s, for thin film batteries,

applying stack pressure has not been tried due to intrinsic atomic-level contact between layers and limitation of experimental setup. Thus, it is worth investigating pressure dependence of plated Li morphology and chemistry in the system with FIB-SEM and TEM, which must contribute to deeper understanding of Li.

5.2.2 Chip-based *in-situ* biasing in microscopy

To deeply understand interphase formation dynamics such as CEI or SEI during cell cycling operation, advanced microscopy and spectroscopy at an atomic scale required to be coupled with *in-situ* or *operando* techniques. Wang et al. from our group has successfully observed disordered LCO formation at cathode electrolyte interface with *in-situ* techniques as shown in Figure 5.5[50], where nanobattery lifted out of thin film battery were electrochemically operated inside TEM. The paper also emphasized strength and importance of *in-situ* methodology to measure dynamics of chemistry and structure at the interface, by comparing *ex-situ* measured data, where *ex-situ* data demonstrated fully relaxed CoO formation and missed chemical changes to form Li_2O or Li_2O_2. Therefore, *in-situ* microscopy is capable of capturing metastable state that is not fully structurally/chemically relaxed, as well as avoiding potential risk of air exposure during sample transfer.
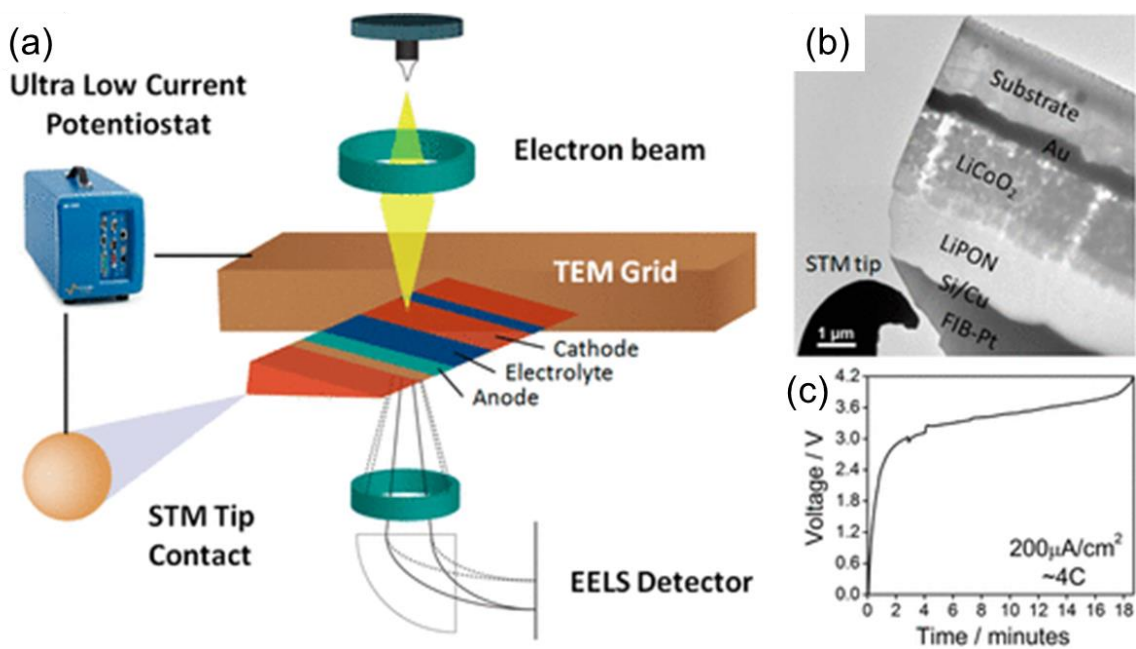
Figure 5.5 In-situ TEM biasing measurement. (a) Schematic illustration of in-situ biasing of nanobattery inside TEM. (b) TEM bright field image of STM tip connecting a nanobattery. (c) Voltage profile of the fabricated nanobattery under constant current.

Most of past research on *in-situ* microscopy have been conducted by a probe-base technique[248–255], including Hood's work (Figure 5.3 (a)) and Wang's work (Figure 5.5) that are mentioned above. While the probe-based technique pioneered *in-situ* biasing methodology and has an advantage to be able to use a conventional TEM grid for biasing, there is still a challenge to make it compatible with cryo methodology for beam sensitive materials such as Li metal. This is because the cryo-temperature is below the operating temperature of a piezo-actuator, which probe-based technique relies on for the nano-scale manipulation of the needle (STM tip)[256]. To overcome this issue, a chip-based technique can be employed. As it has already been explained in sub-chapter 4.5 and Figure 4.12, chip-based methodology utilize specially designed-chip, where a nanodevice fabricated by FIB bridges the gap (a few to a few tens of micron, depending on chip brands) on the center of the chip (Figure 4.12 (a) and (b). On both sides of the gap, metal current collectors are patterned, and provide electrical connection to a biasing holder when the chip is mounted on

it. This method secures the contact from the nanodevice to current collector and free from sensitive manipulation of the needle. The Chip-based techniques is already used for biasing perovskite solar cell[61] and studying thermal vulnerability of $LiCoO_2$ though joule heat generated by electrical current[257]. To summarize the discussion, despite technical complexities in fabrication and manipulation of the nanodevices, and operation of electron microscopy measurement with galvano/potentiostatic biasing, the in-situ microscopy must be able to offer deeper insights of structure, morphology, and chemistry at nano- or atomic-scale during battery operation, facilitating understanding of the fundamental science of the battery.

5.3 Beyond LIB

Last but not least, the third direction of the future of thin films is more focused on the application to electric devices. As mentioned in the previous section, thin film batteries can be fabricated by stacking multiple layers of thin films. However, this is not limited to battery. One of the major applications is synaptic transistor aiming for neuromorphic computing. Compared to conventional transistor such as complementary metal-oxide-semiconductor (CMOS), the advantages of synaptic transistors using Li-ion battery materials are low power consumption, scalability, and analog characteristics for neuromorphic architecture consisting of non-volatile memories. In the three-terminal device, external electrical bias migrate Li ions and intercalates them into channel material ("write" process), leading to change in conductance between source and drain electrodes ("read" process). In other words, in the device, vertical layer stacking works as a battery and lateral source and drain work as a main current path in a computation system. For example, Nguyen et al fabricated a synaptic transistor device with Ti, TiO_2 and LiPON, which works as a electrodes, channel, and electrolyte, respectively (Figure 5.6 (a)-(c)). In their device, Li ions are intercalated into TiO_2 layer, forming Li_xTiO_2, under positive voltage bias on the gate

electrode. Thus, the Li-intercalated channel becomes conductive and source-drain conductance becomes increased. Under negative biasing, Li is deintercalated from TiO_2 channel and the conductance goes back to the original state. As a channel layer, intercalation type materials has been commonly selected, such as $LiCoO_2$[108,258], WO_x[259–261], and Nb_2O_5[262]. Combining photolithography techniques with PVD, they could have realized 1.5 to 40 times conductance change with decent durability, that is, 10^5 times of write process at maximum[259].

Despite such great achievements that have been done within less than ten years, their studies mostly focus on its performance as a device. Although it is crucial to evaluate their performance upon applying the synaptic transistors to neuromorphic computing, characterization of inside the device under its operation, or quantitative analysis of Li ion dynamics, is also important direction for the device research to go. This is because slight compositional may change in the electrical properties of the Li-ion material as exemplified in the case of WO_x[260] and $Li_4Ti_5O_{12}$[112]. In the case of gate voltage biasing for (de)lithiation, it is difficult to control the amount of charge carrier, making it difficult to guess lithiation state. Furthermore, non-flat configuration (Figure 5.6 (a) and (b)) may create non-homogeneous electric field, leading to local formation of lithium-ion excess/deficient state. *In-situ* TEM combining EELS with biasing, as introduced in the previous section, could be a first choice as a characterization, due to its high spatial resolution and wide availability of elements of interest. This technique can provide crystallinity and chemistry in one device and also with and without biasing (i.e. both ON and OFF states). The synaptic transistor relies on conductive channel formation, and, therefore, observing and quantifying such formation will facilitate future development and improvement.
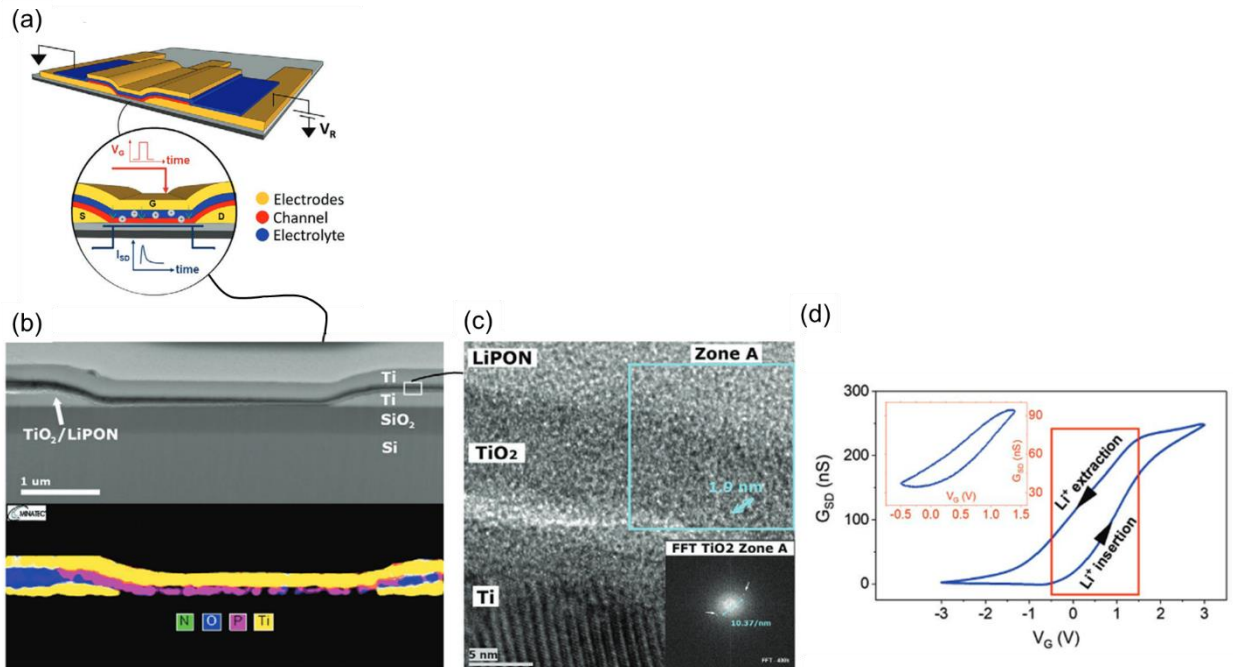
Figure 5.6 Synaptic transistor with battery materials. (a) Schematic illustration of electrodes, electrolyte, and channel layers. (b) SEM and EDS, (c) HRTEM images of the cross section of the device. (d) Conductance between the source and drain electrodes (G_{SD}) vs. gate voltage (V_G)[114].

Another direction can be the integration of thin film battery to other electric devices aiming for commercial in-chip devices. Since synaptic transistors are partially composed of battery electrodes and electrolyte, indeed, it can also be defined as a hybrid device of battery and transistor. Due to its micro-scale characteristics of PVD thin film fabrication process (no liquid, and layer-by-layer configuration), thin film battery has a potential to be compatible to other thin film devices, e.g. solar cells and sensors, where a battery is used as an energy storage and power supply. Sandbaumhüter et al. had studied performance of integration device of solar cell and battery[263], claiming that it is challenging to match operating voltage of both solar cell and battery units. Chen et al. has also investigated the integrated device of a solar cell, processor and battery as an independently-powered sensor[264]. As shown above, unlike bulk batteries, current and future thin film batteries can contribute to both fundamental research and application to commercialized in-chip devices, facilitating realization of high-performance batteries from nano to bulk scale.

5.4 Acknowledgements

Chapter 5 contains unpublished materials coauthored with Weikang Li. The dissertation author was the primary author of this chapter.

References

(1)   Ritchie, H.; Roser, M.; Rosado, P. *CO₂ and Greenhouse Gas Emissions*. OurWorldInData.org. https://ourworldindata.org/co2-and-greenhouse-gas-emissions.

(2)   Jones-Albertus, B. *Confronting the Duck Curve: How to Address Over-Generation of Solar Energy*. Office of Energy Efficiency & Renewable Energy. https://www.energy.gov/eere/articles/confronting-duck-curve-how-address-over-generation-solar-energy.

(3)   *Transportation Energy Data Book*, 40th ed.; U.S. Department of Energy, Energy Vehicle Technologies Office, Oak Ridge National Laboratory, 2022.

(4)   Goodenough, J. B.; Park, K. S. The Li-Ion Rechargeable Battery: A Perspective. *Journal of the American Chemical Society* **2013**, *135* (4), 1167–1176. https://doi.org/10.1021/ja3091438.

(5)   Huggins, R. A. *Advanced Batteries*; Springer US: Boston, MA, 2009. https://doi.org/10.1007/978-0-387-76424-5.

(6)   Osiak, M.; Geaney, H.; Armstrong, E.; O'Dwyer, C. Structuring Materials for Lithium-Ion Batteries: Advancements in Nanomaterial Structure, Composition, and Defined Assembly on Cell Performance. *J. Mater. Chem. A* **2014**, *2* (25), 9433. https://doi.org/10.1039/c4ta00534a.

(7)   Yang, L.; Ravdel, B.; Lucht, B. L. Electrolyte Reactions with the Surface of High Voltage LiNi[Sub 0.5]Mn[Sub 1.5]O[Sub 4] Cathodes for Lithium-Ion Batteries. *Electrochemical and Solid-State Letters* **2010**, *13* (8), A95. https://doi.org/10.1149/1.3428515.

(8)   Pieczonka, N. P. W.; Liu, Z.; Lu, P.; Olson, K. L.; Moote, J.; Powell, B. R.; Kim, J. H. Understanding Transition-Metal Dissolution Behavior in LiNi 0.5Mn1.5O4 High-Voltage Spinel for Lithium Ion Batteries. *Journal of Physical Chemistry C* **2013**, *117* (31), 15947–15957. https://doi.org/10.1021/jp405158m.

(9)   Kim, J. H.; Pieczonka, N. P. W.; Lu, P.; Liu, Z.; Qiao, R.; Yang, W.; Tessema, M. M.; Sun, Y. K.; Powell, B. R. In Situ Formation of a Cathode-Electrolyte Interface with Enhanced Stability by Titanium Substitution for High Voltage Spinel Lithium-Ion Batteries. *Advanced Materials Interfaces* **2015**, *2* (10), 1–13. https://doi.org/10.1002/admi.201500109.

(10)   Li, W.; Song, B.; Manthiram, A. High-Voltage Positive Electrode Materials for Lithium-Ion Batteries. *Chemical Society Reviews* **2017**, *46* (10), 3006–3059. https://doi.org/10.1039/c6cs00875e.

(11)   Sloop, S. E.; Kerr, J. B.; Kinoshita, K. The Role of Li-Ion Battery Electrolyte Reactivity in Performance Decline and Self-Discharge. *Journal of Power Sources* **2003**, *119–121*, 330–337. https://doi.org/10.1016/S0378-7753(03)00149-6.

(12)   Asl, H. Y.; Manthiram, A. Reining in Dissolved Transition-Metal Ions. *Science* **2020**, *369* (6500), 140–141. https://doi.org/10.1126/science.abc5454.

(13)   Gilbert, J. A.; Shkrob, I. A.; Abraham, D. P. Transition Metal Dissolution, Ion Migration, Electrocatalytic Reduction and Capacity Loss in Lithium-Ion Full Cells. *Journal of The Electrochemical Society* **2017**, *164* (2), A389–A399. https://doi.org/10.1149/2.1111702jes.

(14)   Zhan, C.; Lu, J.; Jeremy Kropf, A.; Wu, T.; Jansen, A. N.; Sun, Y. K.; Qiu, X.; Amine, K. Mn(II) Deposition on Anodes and Its Effects on Capacity Fade in Spinel Lithium Manganate-Carbon Systems. *Nature Communications* **2013**, *4* (Ii), 1–8. https://doi.org/10.1038/ncomms3437.

(15)   Nanda, J.; Wang, C.; Liu, P. Frontiers of Solid-State Batteries. *MRS Bulletin* **2018**, *43* (10), 740–745. https://doi.org/10.1557/mrs.2018.234.

(16)   Takada, K. Progress in Solid Electrolytes toward Realizing Solid-State Lithium Batteries. *Journal of Power Sources* **2018**, *394*, 74–85. https://doi.org/10.1016/j.jpowsour.2018.05.003.

(17)   Muramatsu, H.; Hayashi, A.; Ohtomo, T.; Hama, S.; Tatsumisago, M. Structural Change of Li2S-P2S5 Sulfide Solid Electrolytes in the Atmosphere. *Solid State Ionics* **2011**, *182* (1), 116–119. https://doi.org/10.1016/j.ssi.2010.10.013.

(18)   Kamaya, N.; Homma, K.; Yamakawa, Y.; Hirayama, M.; Kanno, R.; Yonemura, M.; Kamiyama, T.; Kato, Y.; Hama, S.; Kawamoto, K.; Mitsui, A. A Lithium Superionic Conductor. *Nature Materials* **2011**, *10* (9), 682–686. https://doi.org/10.1038/nmat3066.

(19)   Richards, W. D.; Miara, L. J.; Wang, Y.; Kim, J. C.; Ceder, G. Interface Stability in Solid-State Batteries. *Chem. Mater.* **2016**, *28* (1), 266–273. https://doi.org/10.1021/acs.chemmater.5b04082.

(20)   Banerjee, A.; Wang, X.; Fang, C.; Wu, E. A.; Meng, Y. S. Interfaces and Interphases in All-Solid-State Batteries with Inorganic Solid Electrolytes. *Chem. Rev.* **2020**, *120* (14), 6878–6933. https://doi.org/10.1021/acs.chemrev.0c00101.

(21)   Wu, B.; Chen, C.; Danilov, D. L.; Eichel, R.-A.; Notten, P. H. L. All-Solid-State Thin Film Li-Ion Batteries: New Challenges, New Materials, and New Designs. *Batteries* **2023**, *9* (3), 186. https://doi.org/10.3390/batteries9030186.

(22)   Liang, C. C.; Bro, P. A High-Voltage, Solid-State Battery System: I . Design Considerations. *J. Electrochem. Soc.* **1969**, *116* (9), 1322. https://doi.org/10.1149/1.2412312.

(23)   Bates, J. B.; Dudney, N. J.; Neudecker, B.; Ueda, A.; Evans, C. D. Thin-Film Lithium and Lithium-Ion Batteries. *Solid State Ionics* **2000**, *135* (1–4), 33–45. https://doi.org/10.1016/S0167-2738(00)00327-1.

(24) Lee, S.-H.; Liu, P.; Tracy, C. E.; Benson, D. K. All-Solid-State Rocking Chair Lithium Battery on a Flexible Al Substrate. *Electrochem. Solid-State Lett.* **1999**, *2* (9), 425. https://doi.org/10.1149/1.1390859.

(25) Neudecker, B. J.; Zuhr, R. A.; Bates, J. B. Lithium Silicon Tin Oxynitride (LiySiTON): High-Performance Anode in Thin-Film Lithium-Ion Batteries for Microelectronics. *Journal of Power Sources* **1999**, *81–82*, 27–32. https://doi.org/10.1016/S0378-7753(98)00202-X.

(26) Park, Y.-S.; Lee, S.-H.; Lee, B.-I.; Joo, S.-K. All-Solid-State Lithium Thin-Film Rechargeable Battery with Lithium Manganese Oxide. *Electrochem. Solid-State Lett.* **1998**, *2* (2), 58. https://doi.org/10.1149/1.1390733.

(27) Bates, J. B.; Dudney, N. J.; Neudecker, B. J.; Hart, F. X.; Jun, H. P.; Hackney, S. A. Preferred Orientation of Polycrystalline LiCoO2 Films. *J. Electrochem. Soc.* **2000**, *147* (1), 59. https://doi.org/10.1149/1.1393157.

(28) Dudney, N. J.; Bates, J. B.; Zuhr, R. A.; Young, S.; Robertson, J. D.; Jun, H. P.; Hackney, S. A. Nanocrystalline Li x Mn2 − y O 4 Cathodes for Solid-State Thin-Film Rechargeable Lithium Batteries. *J. Electrochem. Soc.* **1999**, *146* (7), 2455. https://doi.org/10.1149/1.1391955.

(29) Neudecker, B. J.; Zuhr, R. A.; Kwak, B. S.; Bates, J. B.; Robertson, J. D. Lithium Manganese Nickel Oxides Li x (Mn y Ni1 − y) 2 − x O 2 : I. Synthesis and Characterization of Thin Films and Bulk Phases. *J. Electrochem. Soc.* **1998**, *145* (12), 4148. https://doi.org/10.1149/1.1838929.

(30) Neudecker, B. J.; Dudney, N. J.; Bates, J. B. "Lithium-Free" Thin-Film Battery with In Situ Plated Li Anode. *Journal of The Electrochemical Society* **2000**, *147* (2), 517. https://doi.org/10.1149/1.1393226.

(31) Dudney, N. J.; Neudecker, B. J. Solid State Thin-Film Lithium Battery Systems. *Current Opinion in Solid State and Materials Science* **1999**, *4* (5), 479–482. https://doi.org/10.1016/S1359-0286(99)00052-2.

(32) Kawasoko, H.; Shirasawa, T.; Nishio, K.; Shimizu, R.; Shiraki, S.; Hitosugi, T. Clean Solid–Electrolyte/Electrode Interfaces Double the Capacity of Solid-State Lithium Batteries. *ACS Appl. Mater. Interfaces* **2021**, *13* (4), 5861–5865. https://doi.org/10.1021/acsami.0c21586.

(33) Wu, Q.; Liu, Y.; Johnson, C. S.; Li, Y.; Dees, D. W.; Lu, W. Insight into the Structural Evolution of a High-Voltage Spinel for Lithium-Ion Batteries. *Chemistry of Materials* **2014**, *26* (16), 4750–4756. https://doi.org/10.1021/cm5015288.

(34) Lu, D. S.; Yuan, L. B.; Li, J. L.; Huang, R. Q.; Guo, J. H.; Cai, Y. P. Failure Mechanism for High Voltage Graphite/LiNi0.5Mn1.5O4 (LNMO) Li-Ion Cells Stored at Elevated Temperature. *Journal of Electroanalytical Chemistry* **2015**, *758*, 33–38. https://doi.org/10.1016/j.jelechem.2015.10.018.

(35)   Lu, D.; Xu, M.; Zhou, L.; Garsuch, A.; Lucht, B. L. Failure Mechanism of Graphite/LiNi 0.5 Mn 1.5 O 4 Cells at High Voltage and Elevated Temperature. *Journal of The Electrochemical Society* **2013**, *160* (5), A3138–A3143. https://doi.org/10.1149/2.022305jes.

(36)   Yoon, T.; Park, S.; Mun, J.; Ryu, J. H.; Choi, W.; Kang, Y. S.; Park, J. H.; Oh, S. M. Failure Mechanisms of LiNi 0.5Mn 1.5O 4 Electrode at Elevated Temperature. *Journal of Power Sources* **2012**, *215*, 312–316. https://doi.org/10.1016/j.jpowsour.2012.04.103.

(37)   Li, W.; Cheng, D.; Shimizu, R.; Li, Y.; Yao, W.; Raghavendran, G.; Zhang, M.; Meng, Y. S. Artificial Cathode Electrolyte Interphase for Improving High Voltage Cycling Stability of Thick Electrode with Co-Free 5 V Spinel Oxides. *Energy Storage Materials* **2022**, *49*, 77–84. https://doi.org/10.1016/j.ensm.2022.04.002.

(38)   Intan, N. N.; Klyukin, K.; Alexandrov, V. Ab Initio Modeling of Transition Metal Dissolution from the LiNi0.5Mn1.5O4 Cathode. *ACS Applied Materials and Interfaces* **2019**, *11* (22), 20110–20116. https://doi.org/10.1021/acsami.9b06010.

(39)   Mohamedi, M.; Makino, M.; Dokko, K.; Itoh, T.; Uchida, I. Electrochemical Investigation of LiNi0.5Mn1.5O4 Thin Film Intercalation Electrodes. *Electrochimica Acta* **2002**, *48* (1), 79–84. https://doi.org/10.1016/S0013-4686(02)00554-6.

(40)   Xia, H.; Meng, Y. S.; Tang, S. B.; Lu, L.; Ceder, G. The Influence of Preparation Conditions on Electrochemical Properties of LiNi0.5Mn1.5O4 Thin Film Electrodes by PLD. *Electrochimica Acta* **2006**, *52* (8), 2822–2828. https://doi.org/10.1016/j.electacta.2006.07.013.

(41)   Xia, H.; Meng, Y. S.; Lu, L.; Ceder, G. Electrochemical Properties of Nonstoichiometric LiNi0.5Mn1.5O4−δ Thin-Film Electrodes Prepared by Pulsed Laser Deposition. *Journal of The Electrochemical Society* **2007**, *154* (8), A737. https://doi.org/10.1149/1.2741157.

(42)   Konishi, H.; Suzuki, K.; Taminato, S.; Kim, K.; Kim, S.; Lim, J.; Hirayama, M.; Kanno, R. Structure and Electrochemical Properties of LiNi0.5Mn 1.5O4 Epitaxial Thin Film Electrodes. *Journal of Power Sources* **2014**, *246*, 365–370. https://doi.org/10.1016/j.jpowsour.2013.07.051.

(43)   Konishi, H.; Suzuki, K.; Taminato, S.; Kim, K.; Zheng, Y.; Kim, S.; Lim, J.; Hirayama, M.; Son, J. Y.; Cui, Y.; Kanno, R. Effect of Surface Li3PO4 Coating on LiNi 0.5Mn1.5O4 Epitaxial Thin Film Electrodes Synthesized by Pulsed Laser Deposition. *Journal of Power Sources* **2014**, *269*, 293–298. https://doi.org/10.1016/j.jpowsour.2014.05.052.

(44)   Lee, S.; Kim, H.; Lee, J.-H.; Kim, B.-K.; Shin, H.; Kim, J.; Park, S. Nano-Interface Engineering in All-Solid-State Lithium Metal Batteries: Tailoring Exposed Crystal Facets of Epitaxially Grown LiNi0.5Mn1.5O4 Films. *Nano Energy* **2021**, *79*, 105480. https://doi.org/10.1016/j.nanoen.2020.105480.

(45) Yu, X.; Bates, J. B.; Jr, G. E. J.; Hart, F. X. A Stable Thin-Film Lithium Electrolyte: Lithium Phosphorus Oxynitride. *J. Electrochem. Soc.* **1997**, *144* (2), 524. https://doi.org/10.1149/1.1837443.

(46) Wang, J.; Du, C.; Xu, X.; He, X.; Yin, G.; Ma, Y.; Zuo, P.; Cheng, X.; Gao, Y. Lithium Phosphorus Oxynitride Coated Concentration Gradient Li[Ni0.73Co0.12Mn0.15]O2 Cathode Material with Enhanced Electrochemical Properties. *Electrochimica Acta* **2016**, *192*, 340–345. https://doi.org/10.1016/j.electacta.2016.01.176.

(47) Kim, Y.; Dudney, N. J.; Chi, M.; Martha, S. K.; Nanda, J.; Veith, G. M.; Liang, C. A Perspective on Coatings to Stabilize High-Voltage Cathodes: LiMn1.5Ni0.5O4 with Sub-Nanometer Lipon Cycled with LiPF6 Electrolyte. *J. Electrochem. Soc.* **2013**, *160* (5), A3113. https://doi.org/10.1149/2.017305jes.

(48) Santhanagopalan, D.; Qian, D.; McGilvray, T.; Wang, Z.; Wang, F.; Camino, F.; Graetz, J.; Dudney, N.; Meng, Y. S. Interface Limited Lithium Transport in Solid-State Batteries. *Journal of Physical Chemistry Letters* **2014**, *5* (2), 298–303. https://doi.org/10.1021/jz402467x.

(49) Wang, Z.; Lee, J. Z.; Xin, H. L.; Han, L.; Grillon, N.; Guy-Bouyssou, D.; Bouyssou, E.; Proust, M.; Meng, Y. S. Effects of Cathode Electrolyte Interfacial (CEI) Layer on Long Term Cycling of All-Solid-State Thin-Film Batteries. *Journal of Power Sources* **2016**, *324*, 342–348. https://doi.org/10.1016/j.jpowsour.2016.05.098.

(50) Wang, Z.; Santhanagopalan, D.; Zhang, W.; Wang, F.; Xin, H. L.; He, K.; Li, J.; Dudney, N.; Meng, Y. S. In Situ STEM-EELS Observation of Nanoscale Interfacial Phenomena in All-Solid-State Batteries. *Nano Letters* **2016**, *16* (6), 3760–3767. https://doi.org/10.1021/acs.nanolett.6b01119.

(51) Iriyama, Y.; Nishimoto, K.; Yada, C.; Abe, T.; Ogumi, Z.; Kikuchi, K. Charge-Transfer Reaction at the Lithium Phosphorus Oxynitride Glass Electrolyte/Lithium Manganese Oxide Thin-Film Interface and Its Stability on Cycling. *Journal of The Electrochemical Society* **2006**, *153* (5), A821. https://doi.org/10.1149/1.2178647.

(52) Li, C. L.; Fu, Z. W. All-Solid-State Rechargeable Thin Film Lithium Batteries with LixMn2O4 and LixMn2O4-0.5ZrO2 Cathodes. *Electrochimica Acta* **2007**, *52* (20), 6155–6164. https://doi.org/10.1016/j.electacta.2007.04.012.

(53) Phillip, N. D.; Westover, A. S.; Daniel, C.; Veith, G. M. Structural Degradation of High Voltage Lithium Nickel Manganese Cobalt Oxide (NMC) Cathodes in Solid-State Batteries and Implications for Next Generation Energy Storage. *ACS Appl. Energy Mater.* **2020**, *3* (2), 1768–1774. https://doi.org/10.1021/acsaem.9b02230.

(54) Li, J.; Ma, C.; Chi, M.; Liang, C.; Dudney, N. J. Solid Electrolyte: The Key for High-Voltage Lithium Batteries. *Advanced Energy Materials* **2015**, *5* (4), 1–6. https://doi.org/10.1002/aenm.201401408.

(55)   Zhu, Y.; He, X.; Mo, Y. Origin of Outstanding Stability in the Lithium Solid Electrolyte Materials: Insights from Thermodynamic Analyses Based on First-Principles Calculations. *ACS Appl. Mater. Interfaces* **2015**, *7* (42), 23685–23693. https://doi.org/10.1021/acsami.5b07517.

(56)   Tippens, J.; Miers, J. C.; Afshar, A.; Lewis, J. A.; Cortes, F. J. Q.; Qiao, H.; Marchese, T. S.; Di Leo, C. V.; Saldana, C.; McDowell, M. T. Visualizing Chemomechanical Degradation of a Solid-State Battery Electrolyte. *ACS Energy Lett.* **2019**, *4* (6), 1475–1483. https://doi.org/10.1021/acsenergylett.9b00816.

(57)   Ma, C.; Cheng, Y.; Yin, K.; Luo, J.; Sharafi, A.; Sakamoto, J.; Li, J.; More, K. L.; Dudney, N. J.; Chi, M. Interfacial Stability of Li Metal−Solid Electrolyte Elucidated via in Situ Electron Microscopy. **2016**. https://doi.org/10.1021/acs.nanolett.6b03223.

(58)   Haruta, M.; Shiraki, S.; Suzuki, T.; Kumatani, A.; Ohsawa, T.; Takagi, Y.; Shimizu, R.; Hitosugi, T. Negligible "Negative Space-Charge Layer Effects" at Oxide-Electrolyte/Electrode Interfaces of Thin-Film Batteries. *Nano Letters* **2015**, *15* (3), 1498–1502. https://doi.org/10.1021/nl5035896.

(59)   Kawasoko, H.; Shiraki, S.; Suzuki, T.; Shimizu, R.; Hitosugi, T. Extremely Low Resistance of Li3PO4Electrolyte/Li(Ni0.5Mn1.5)O4Electrode Interfaces. *ACS Applied Materials and Interfaces* **2018**, *10* (32), 27498–27502. https://doi.org/10.1021/acsami.8b08506.

(60)   Kawasoko, H.; Shirasawa, T.; Shiraki, S.; Suzuki, T.; Kobayashi, S.; Nishio, K.; Shimizu, R.; Hitosugi, T. Low Interface Resistance in Solid-State Lithium Batteries Using Spinel LiNi0.5Mn1.5O4(111) Epitaxial Thin Films. *ACS Applied Energy Materials* **2020**, *3* (2), 1358–1363. https://doi.org/10.1021/acsaem.9b01766.

(61)   Cheng, D.; Wynn, T. A.; Wang, X.; Wang, S.; Zhang, M.; Shimizu, R.; Bai, S.; Nguyen, H.; Fang, C.; Kim, M.; Li, W.; Lu, B.; Kim, S. J.; Meng, Y. S. Unveiling the Stable Nature of the Solid Electrolyte Interphase between Lithium Metal and LiPON via Cryogenic Electron Microscopy. *Joule* **2020**, S2542435120303949. https://doi.org/10.1016/j.joule.2020.08.013.

(62)   Sun, Y.; Guan, P.; Liu, Y.; Xu, H.; Li, S.; Chu, D. Recent Progress in Lithium Lanthanum Titanate Electrolyte towards All Solid-State Lithium Ion Secondary Battery. *Critical Reviews in Solid State and Materials Sciences* **2018**, *0* (0), 1–18. https://doi.org/10.1080/10408436.2018.1485551.

(63)   Deng, Y.; Shang, S.-J.; Mei, A.; Lin, Y.-H.; Liu, L.-Y.; Nan, C.-W. The Preparation and Conductivity Properties of Li0.5La0.5TiO3/Inactive Second Phase Composites. *Journal of Alloys and Compounds* **2009**, *472* (1), 456–460. https://doi.org/10.1016/j.jallcom.2008.04.085.

(64)   Mei, A.; Wang, X.-L.; Feng, Y.-C.; Zhao, S.-J.; Li, G.-J.; Geng, H.-X.; Lin, Y.-H.; Nan, C.-W. Enhanced Ionic Transport in Lithium Lanthanum Titanium Oxide Solid State Electrolyte by Introducing Silica. *Solid State Ionics* **2008**, *179* (39), 2255–2259. https://doi.org/10.1016/j.ssi.2008.08.013.

(65) Chen, K.; Huang, M.; Shen, Y.; Lin, Y.; Nan, C. W. Improving Ionic Conductivity of Li0.35La0.55TiO3 Ceramics by Introducing Li7La3Zr2O12 Sol into the Precursor Powder. *Solid State Ionics* **2013**, *235*, 8–13. https://doi.org/10.1016/j.ssi.2013.01.007.

(66) Chen, K.; Huang, M.; Shen, Y.; Lin, Y.; Nan, C. W. Enhancing Ionic Conductivity of Li0.35La0.55TiO3 Ceramics by Introducing Li7La3Zr2O12. *Electrochimica Acta* **2012**, *80*, 133–139. https://doi.org/10.1016/j.electacta.2012.06.115.

(67) Morata-Orrantia, A.; García-Martín, S.; Alario-Franco, M. Á. Optimization of Lithium Conductivity in La/Li Titanates. *Chem. Mater.* **2003**, *15* (21), 3991–3995. https://doi.org/10.1021/cm0300563.

(68) Lee, J. Z.; Wang, Z.; Xin, H. L.; Wynn, T. A.; Meng, Y. S. Amorphous Lithium Lanthanum Titanate for Solid-State Microbatteries. *J. Electrochem. Soc.* **2016**, *164* (1), A6268. https://doi.org/10.1149/2.0411701jes.

(69) Furusawa, S.; Tabuchi, H.; Sugiyama, T.; Tao, S.; Irvine, J. T. S. Ionic Conductivity of Amorphous Lithium Lanthanum Titanate Thin Film. *Solid State Ionics* **2005**, *176* (5), 553–558. https://doi.org/10.1016/j.ssi.2004.08.020.

(70) Ahn, J.; Yoon, S. Characteristics of Amorphous Lithium Lanthanum Titanate Electrolyte Thin Films Grown by PLD for Use in Rechargeable Lithium Microbatteries. *Electrochemical and Solid-State Letters* **2005**, *8* (2), A75. https://doi.org/10.1149/1.1843571.

(71) Nong, J.; Xu, H.; Yu, Z.; Zhu, G.; Yu, A. Properties and Preparation of Li–La–Ti–Zr–O Thin Film Electrolyte. *Materials Letters* **2015**, *154*, 167–169. https://doi.org/10.1016/j.matlet.2015.04.088.

(72) Chen, R.; Liang, W.; Zhang, H.; Wu, F.; Li, L. Preparation and Performance of Novel LLTO Thin Film Electrolytes for Thin Film Lithium Batteries. *Chin. Sci. Bull.* **2012**, *57* (32), 4199–4204. https://doi.org/10.1007/s11434-012-5292-y.

(73) Song, S.-P.; Yang, C.; Jiang, C.-Z.; Wu, Y.-M.; Guo, R.; Sun, H.; Yang, J.-L.; Xiang, Y.; Zhang, X.-K. Increasing Ionic Conductivity in Li0.33La0.56TiO3 Thin-Films via Optimization of Processing Atmosphere and Temperature. *Rare Met.* **2022**, *41* (1), 179–188. https://doi.org/10.1007/s12598-021-01782-5.

(74) Aguesse, F.; López del Amo, J. M.; Roddatis, V.; Aguadero, A.; Kilner, J. A. Enhancement of the Grain Boundary Conductivity in Ceramic Li0.34La0.55TiO3 Electrolytes in a Moisture-Free Processing Environment. *Advanced Materials Interfaces* **2014**, *1* (7), 1300143. https://doi.org/10.1002/admi.201300143.

(75) Geng, H.; Mei, A.; Lin, Y.; Nan, C. Effect of Sintering Atmosphere on Ionic Conduction and Structure of Li0.5La0.5TiO3 Solid Electrolytes. *Materials Science and Engineering: B* **2009**, *164* (2), 91–95. https://doi.org/10.1016/j.mseb.2009.07.011.

(76)   Xiong, Y.; Tao, H.; Zhao, J.; Cheng, H.; Zhao, X. Effects of Annealing Temperature on Structure and Opt-Electric Properties of Ion-Conducting LLTO Thin Films Prepared by RF Magnetron Sputtering. *Journal of Alloys and Compounds* **2011**, *509* (5), 1910–1914. https://doi.org/10.1016/j.jallcom.2010.10.086.

(77)   Inaguma, Y.; Liquan, C.; Itoh, M.; Nakamura, T.; Uchida, T.; Ikuta, H.; Wakihara, M. High Ionic Conductivity in Lithium Lanthanum Titanate. *Solid State Communications* **1993**, *86* (10), 689–693. https://doi.org/10.1016/0038-1098(93)90841-A.

(78)   Chen, C. H.; Amine, K. Ionic Conductivity, Lithium Insertion and Extraction of Lanthanum Lithium Titanate. *Solid State Ionics* **2001**, *144* (1), 51–57. https://doi.org/10.1016/S0167-2738(01)00884-0.

(79)   Zheng, Z.; Fang, H.; Liu, Z.; Wang, Y. A Fundamental Stability Study for Amorphous LiLaTiO3 Solid Electrolyte. *J. Electrochem. Soc.* **2014**, *162* (1), A244. https://doi.org/10.1149/2.0011503jes.

(80)   Moore, G. E. Cramming More Components onto Integrated Circuits. *Electronics* **1965**, *38* (8).

(81)   Zhu, Y.; Gonzalez-Rosillo, J. C.; Balaish, M.; Hood, Z. D.; Kim, K. J.; Rupp, J. L. M. Lithium-Film Ceramics for Solid-State Lithionic Devices. *Nature Reviews Materials* **2021**, *6* (4), 313–331. https://doi.org/10.1038/s41578-020-00261-0.

(82)   Olofsson, A. Silicon Compilers - Version 2.0, 2018. https://onl.sc/WiNZ1K1.

(83)   *Apple unveils M2, taking the breakthrough performance and capabilities of M1 even further*. Apple. https://onl.sc/swmCeHM.

(84)   Jacobi, C. Real-Time AI for Enterprise Workloads: The IBM Telum Processor, 2021. https://onl.sc/YMmmnEv.

(85)   Lee, M.-H. New Materials and Techniques for Resistive Switching Devices and Neuromorphic Computing, University of California San Diego, 2021.

(86)   Wang, Z.; Wu, H.; Burr, G. W.; Hwang, C. S.; Wang, K. L.; Xia, Q.; Yang, J. J. Resistive Switching Materials for Information Processing. *Nat Rev Mater* **2020**, *5* (3), 173–195. https://doi.org/10.1038/s41578-019-0159-3.

(87)   Sawa, A. Resistive Switching in Transition Metal Oxides. *Materials Today* **2008**, *11* (6), 28–36. https://doi.org/10.1016/S1369-7021(08)70119-6.

(88)   Burr, G. W.; Breitwisch, M. J.; Franceschini, M.; Garetto, D.; Gopalakrishnan, K.; Jackson, B.; Kurdi, B.; Lam, C.; Lastras, L. A.; Padilla, A.; Rajendran, B.; Raoux, S.; Shenoy, R. S. Phase Change Memory Technology. *Journal of Vacuum Science & Technology B* **2010**, *28* (2), 223–262. https://doi.org/10.1116/1.3301579.

(89) Burr, G. W.; Brightsky, M. J.; Sebastian, A.; Cheng, H.-Y.; Wu, J.-Y.; Kim, S.; Sosa, N. E.; Papandreou, N.; Lung, H.-L.; Pozidis, H.; Eleftheriou, E.; Lam, C. H. Recent Progress in Phase-Change Memory Technology. *IEEE Journal on Emerging and Selected Topics in Circuits and Systems* **2016**, *6* (2), 146–162. https://doi.org/10.1109/JETCAS.2016.2547718.

(90) Raoux, S.; Burr, G. W.; Breitwisch, M. J.; Rettner, C. T.; Chen, Y.-C.; Shelby, R. M.; Salinga, M.; Krebs, D.; Chen, S.-H.; Lung, H.-L.; Lam, C. H. Phase-Change Random Access Memory: A Scalable Technology. *IBM Journal of Research and Development* **2008**, *52* (4.5), 465–479. https://doi.org/10.1147/rd.524.0465.

(91) Tuma, T.; Pantazi, A.; Le Gallo, M.; Sebastian, A.; Eleftheriou, E. Stochastic Phase-Change Neurons. *Nature Nanotech* **2016**, *11* (8), 693–699. https://doi.org/10.1038/nnano.2016.70.

(92) Katzke, H.; Tolédano, P.; Depmeier, W. Theory of Morphotropic Transformations in Vanadium Oxides. *Phys. Rev. B* **2003**, *68* (2), 024109. https://doi.org/10.1103/PhysRevB.68.024109.

(93) Ngai, J. H.; Walker, F. J.; Ahn, C. H. Correlated Oxide Physics and Electronics. *Annual Review of Materials Research* **2014**, *44* (1), 1–17. https://doi.org/10.1146/annurev-matsci-070813-113248.

(94) Sun, W.; Gao, B.; Chi, M.; Xia, Q.; Yang, J. J.; Qian, H.; Wu, H. Understanding Memristive Switching via in Situ Characterization and Device Modeling. *Nat Commun* **2019**, *10* (1), 3453. https://doi.org/10.1038/s41467-019-11411-6.

(95) Waser, R.; Dittmann, R.; Staikov, G.; Szot, K. Redox-Based Resistive Switching Memories – Nanoionic Mechanisms, Prospects, and Challenges. *Advanced Materials* **2009**, *21* (25–26), 2632–2663. https://doi.org/10.1002/adma.200900375.

(96) Kent, A. D.; Worledge, D. C. A New Spin on Magnetic Memories. *Nature Nanotech* **2015**, *10* (3), 187–191. https://doi.org/10.1038/nnano.2015.24.

(97) Miyazaki, T.; Tezuka, N. Giant Magnetic Tunneling Effect in Fe/Al2O3/Fe Junction. *Journal of Magnetism and Magnetic Materials* **1995**, *139* (3), L231–L234. https://doi.org/10.1016/0304-8853(95)90001-2.

(98) Moodera, J. S.; Kinder, L. R.; Wong, T. M.; Meservey, R. Large Magnetoresistance at Room Temperature in Ferromagnetic Thin Film Tunnel Junctions. *Phys. Rev. Lett.* **1995**, *74* (16), 3273–3276. https://doi.org/10.1103/PhysRevLett.74.3273.

(99) Golonzka, O.; Alzate, J.-G.; Arslan, U.; Bohr, M.; Bai, P.; Brockman, J.; Buford, B.; Connor, C.; Das, N.; Doyle, B.; Ghani, T.; Hamzaoglu, F.; Heil, P.; Hentges, P.; Jahan, R.; Kencke, D.; Lin, B.; Lu, M.; Mainuddin, M.; Meterelliyoz, M.; Nguyen, P.; Nikonov, D.; O'brien, K.; Donnell, J. O.; Oguz, K.; Ouellette, D.; Park, J.; Pellegren, J.; Puls, C.; Quintero, P.; Rahman, T.; Romang, A.; Sekhar, M.; Selarka, A.; Seth, M.; Smith, A. J.; Smith, A. K.; Wei, L.; Wiegand, C.; Zhang, Z.; Fischer, K. MRAM as Embedded Non-Volatile Memory Solution for 22FFL FinFET Technology. In *2018 IEEE International*

Electron Devices Meeting (IEDM); 2018; p 18.1.1-18.1.4. https://doi.org/10.1109/IEDM.2018.8614620.

(100) Lee, K.; Chao, R.; Yamane, K.; Naik, V. B.; Yang, H.; Kwon, J.; Chung, N. L.; Jang, S. H.; Behin-Aein, B.; Lim, J. H.; K, S.; Liu, B.; Toh, E. H.; Gan, K. W.; Zeng, D.; Thiyagarajah, N.; Goh, L. C.; Ling, T.; Ting, J. W.; Hwang, J.; Zhang, L.; Low, R.; Krishnan, R.; Zhang, L.; Tan, S. L.; You, Y. S.; Seet, C. S.; Cong, H.; Wong, J.; Woo, S. T.; Quek, E.; Siah, S. Y. 22-Nm FD-SOI Embedded MRAM Technology for Low-Power Automotive-Grade-l MCU Applications. In *2018 IEEE International Electron Devices Meeting (IEDM)*; 2018; p 27.1.1-27.1.4. https://doi.org/10.1109/IEDM.2018.8614566.

(101) Song, Y. J.; Lee, J. H.; Han, S. H.; Shin, H. C.; Lee, K. H.; Suh, K.; Jeong, D. E.; Koh, G. H.; Oh, S. C.; Park, J. H.; Park, S. O.; Bae, B. J.; Kwon, O. I.; Hwang, K. H.; Seo, B. Y.; Lee, Y. K.; Hwang, S. H.; Lee, D. S.; Ji, Y.; Park, K. C.; Jeong, G. T.; Hong, H. S.; Lee, K. P.; Kang, H. K.; Jung, E. S. Demonstration of Highly Manufacturable STT-MRAM Embedded in 28nm Logic. In *2018 IEEE International Electron Devices Meeting (IEDM)*; 2018; p 18.2.1-18.2.4. https://doi.org/10.1109/IEDM.2018.8614635.

(102) Dearnaley, G.; Morgan, D. V.; Stoneham, A. M. A Model for Filament Growth and Switching in Amorphous Oxide Films. *Journal of Non-Crystalline Solids* **1970**, *4*, 593–612. https://doi.org/10.1016/0022-3093(70)90097-9.

(103) Zhu, Y. B.; Zheng, K.; Wu, X.; Ang, L. K. Enhanced Stability of Filament-Type Resistive Switching by Interface Engineering. *Sci Rep* **2017**, *7* (1), 43664. https://doi.org/10.1038/srep43664.

(104) Wong, H.-S. P.; Lee, H.-Y.; Yu, S.; Chen, Y.-S.; Wu, Y.; Chen, P.-S.; Lee, B.; Chen, F. T.; Tsai, M.-J. Metal–Oxide RRAM. *Proceedings of the IEEE* **2012**, *100* (6), 1951–1970. https://doi.org/10.1109/JPROC.2012.2190369.

(105) Bagdzevicius, S.; Maas, K.; Boudard, M.; Burriel, M. Interface-Type Resistive Switching in Perovskite Materials. *J Electroceram* **2017**, *39* (1), 157–184. https://doi.org/10.1007/s10832-017-0087-9.

(106) Milewska, A.; Świerczek, K.; Tobola, J.; Boudoire, F.; Hu, Y.; Bora, D. K.; Mun, B. S.; Braun, A.; Molenda, J. The Nature of the Nonmetal–Metal Transition in LixCoO2 Oxide. *Solid State Ionics* **2014**, *263*, 110–118. https://doi.org/10.1016/j.ssi.2014.05.011.

(107) Moradpour, A.; Schneegans, O.; Franger, S.; Revcolevschi, A.; Salot, R.; Auban-Senzier, P.; Pasquier, C.; Svoukis, E.; Giapintzakis, J.; Dragos, O.; Ciomaga, V.-C.; Chrétien, P. Resistive Switching Phenomena in LixCoO2 Thin Films. *Advanced Materials* **2011**, *23* (36), 4141–4145. https://doi.org/10.1002/adma.201101800.

(108) Fuller, E. J.; Gabaly, F. E.; Léonard, F.; Agarwal, S.; Plimpton, S. J.; Jacobs-Gedrim, R. B.; James, C. D.; Marinella, M. J.; Talin, A. A. Li-Ion Synaptic Transistor for Low Power Analog Computing. *Advanced Materials* **2017**, *29* (4), 1604310. https://doi.org/10.1002/adma.201604310.

(109) Xu, G.; Han, P.; Dong, S.; Liu, H.; Cui, G.; Chen, L. Li4Ti5O12-Based Energy Conversion and Storage Systems: Status and Prospects. *Coordination Chemistry Reviews* **2017**, *343*, 139–184. https://doi.org/10.1016/j.ccr.2017.05.006.

(110) Yan, H.; Zhang, D.; Qilu; Duo, X.; Sheng, X. A Review of Spinel Lithium Titanate (Li4Ti5O12) as Electrode Material for Advanced Energy Storage Devices. *Ceramics International* **2021**, *47* (5), 5870–5895. https://doi.org/10.1016/j.ceramint.2020.10.241.

(111) Chen, Z.; Li, H.; Wu, L.; Lu, X.; Zhang, X. Li4Ti5O12 Anode: Structural Design from Material to Electrode and the Construction of Energy Storage Devices. *The Chemical Record* **2018**, *18* (3), 350–380. https://doi.org/10.1002/tcr.201700042.

(112) Young, D.; Ransil, A.; Amin, R.; Li, Z.; Chiang, Y.-M. Electronic Conductivity in the Li4/3Ti5/3O4–Li7/3Ti5/3O4 System and Variation with State-of-Charge as a Li Battery Anode. *Advanced Energy Materials* **2013**, *3* (9), 1125–1129. https://doi.org/10.1002/aenm.201300134.

(113) Gonzalez-Rosillo, J. C.; Balaish, M.; Hood, Z. D.; Nadkarni, N.; Fraggedakis, D.; Kim, K. J.; Mullin, K. M.; Pfenninger, R.; Bazant, M. Z.; Rupp, J. L. M. Lithium-Battery Anode Gains Additional Functionality for Neuromorphic Computing through Metal–Insulator Phase Separation. *Advanced Materials* **2020**, *32* (9), 1907465. https://doi.org/10.1002/adma.201907465.

(114) Nguyen, N.-A.; Schneegans, O.; Salot, R.; Lamy, Y.; Giapintzakis, J.; Mai, V. H.; Oukassi, S. An Ultralow Power LixTiO2-Based Synaptic Transistor for Scalable Neuromorphic Computing. *Advanced Electronic Materials* **2022**, *8* (12), 2200607. https://doi.org/10.1002/aelm.202200607.

(115) Ohring, M. *The Materials Science of Thin Films*; Academic Press, 2002.

(116) Lupis, C.H.P. *Chemical Thermodynamics of Materials*; New York : North-Holland, 1983.

(117) Noh, J.-P.; Jung, K.-T.; Jang, M.-S.; Kwon, T.-H.; Cho, G.-B.; Kim, K.-W.; Nam, T.-H. Protection Effect of ZrO2 Coating Layer on LiCoO2 Thin Film Fabricated by DC Magnetron Sputtering. *Journal of Nanoscience and Nanotechnology* **2013**, *13* (10), 7152–7154. https://doi.org/10.1166/jnn.2013.7806.

(118) Mao, W.; Yuan, W. Influence of Helium on Microstructure and Electrochemical Properties of LiFePO4 Thin Films Electrodes. *Rare Metal Materials and Engineering* **2015**, *44* (11), 2702–2706. https://doi.org/10.1016/S1875-5372(16)60022-X.

(119) Bünting, A.; Uhlenbruck, S.; Sebold, D.; Buchkremer, H. P.; Vaßen, R. Three-Dimensional, Fibrous Lithium Iron Phosphate Structures Deposited by Magnetron Sputtering. *ACS Appl. Mater. Interfaces* **2015**, *7* (40), 22594–22600. https://doi.org/10.1021/acsami.5b07090.

(120) Fischer, J.; Music, D.; Bergfeldt, T.; Ziebert, C.; Ulrich, S.; Seifert, H. J. Experimental and Ab Initio Investigations on Textured Li–Mn–O Spinel Thin Film Cathodes. *Thin Solid Films* **2014**, *572*, 208–215. https://doi.org/10.1016/j.tsf.2014.08.018.

(121) Borhani-Haghighi, S.; Khare, C.; Trócoli, R.; Dushina, A.; Kieschnick, M.; LaMantia, F.; Ludwig, A. Synthesis of Nanostructured LiMn2O4 Thin Films by Glancing Angle Deposition for Li-Ion Battery Applications. *Nanotechnology* **2016**, *27* (45), 455402. https://doi.org/10.1088/0957-4484/27/45/455402.

(122) Su, S.-H.; Chiu, K.-F.; Leu, H.-J. Structural Evolution of Bias Sputtered LiNi0.5Mn1.5O4 Thin Film Cathodes for Lithium Ion Batteries. *Thin Solid Films* **2014**, *572*, 15–19. https://doi.org/10.1016/j.tsf.2014.08.034.

(123) Lv, S.; Li, Z.; Luo, X. The Influence of Preparation Conditions on Structural Evolution and Electrochemical Properties of Sputtered LiNi0.5Mn1.5O4 Thin Film Electrodes. *Applied Surface Science* **2017**, *419*, 631–636. https://doi.org/10.1016/j.apsusc.2017.04.209.

(124) Tan, G.; Wu, F.; Lu, J.; Chen, R.; Li, L.; Amine, K. Controllable Crystalline Preferred Orientation in Li-Co-Ni-Mn Oxide Cathode Thin Films for All-Solid-State Lithium Batteries. *Nanoscale* **2014**, *6* (18), 10611–10622. https://doi.org/10.1039/c4nr02949f.

(125) Baggetto, L.; Mohanty, D.; Meisner, R. A.; Bridges, C. A.; Daniel, C.; Wood, D. L.; Dudney, N. J.; Veith, G. M. Degradation Mechanisms of Lithium-Rich Nickel Manganese Cobalt Oxide Cathode Thin Films. *RSC Advances* **2014**, *4* (45), 23364–23371. https://doi.org/10.1039/c4ra03674c.

(126) Wu, F.; Tan, G.; Lu, J.; Chen, R.; Li, L.; Amine, K. Stable Nanostructured Cathode with Polycrystalline Li-Deficient Li0.28Co0.29Ni0.30Mn0.20O2 for Lithium-Ion Batteries. *Nano Lett.* **2014**, *14* (3), 1281–1287. https://doi.org/10.1021/nl404215h.

(127) Chung, Y.; Park, H.; Oh, S.; Yoon, D. Y.; Jin, S.; Jang, D.; Ko, J. M.; Cho, W. I.; Lee, S.-R. Structural and Electrochemical Properties of LiNi0.7Co0.15Mn0.15O2 Thin Film Prepared by High Frequency Hybrid Direct Current and Radio Frequency Magnetron Sputtering. *J Electroceram* **2013**, *31* (3), 316–323. https://doi.org/10.1007/s10832-013-9845-5.

(128) Lobe, S.; Dellen, C.; Finsterbusch, M.; Gehrke, H.-G.; Sebold, D.; Tsai, C.-L.; Uhlenbruck, S.; Guillon, O. Radio Frequency Magnetron Sputtering of Li7La3Zr2O12 Thin Films for Solid-State Batteries. *Journal of Power Sources* **2016**, *307*, 684–689. https://doi.org/10.1016/j.jpowsour.2015.12.054.

(129) Ma, Y.; Li, L.; Qian, J.; Qu, W.; Luo, R.; Wu, F.; Chen, R. Materials and Structure Engineering by Magnetron Sputtering for Advanced Lithium Batteries. *Energy Storage Materials* **2021**, *39*, 203–224. https://doi.org/10.1016/j.ensm.2021.04.012.

(130) Eason, R. *Pulsesd Laser Deposition of Thin Films: Application-Led Growth of Functional Materials*, 1. Aufl.; Wiley-Interscience, 2007.

(131) Kuwata, N.; Kawamura, J.; Toribami, K.; Hattori, T.; Sata, N. Thin-Film Lithium-Ion Battery with Amorphous Solid Electrolyte Fabricated by Pulsed Laser Deposition. *6* **2004**, *6* (4), 417–421. https://doi.org/10.1016/j.elecom.2004.02.010.

(132) Cao, C.; Li, Z.-B.; Wang, X.-L.; Zhao, X.-B.; Han, W.-Q. Recent Advances in Inorganic Solid Electrolytes for Lithium Batteries. *Frontiers in Energy Research* **2014**, *2* (June), 1–10. https://doi.org/10.3389/fenrg.2014.00025.

(133) Bohnke, O. The Fast Lithium-Ion Conducting Oxides Li3xLa2/3−xTiO3 from Fundamentals to Application. *Solid State Ionics* **2008**, *179* (1), 9–15. https://doi.org/10.1016/j.ssi.2007.12.022.

(134) Yu, C. Probing Li-Ion Transport in Sulfide-Based Solid-State Batteries. Doctral Thesis, Delft University of Technology, 2017. https://doi.org/10.4233/uuid:4c1fca32-534f-464b-9035-a6a622ca1679.

(135) Wang, C.; Gong, Y.; Dai, J.; Zhang, L.; Xie, H.; Pastel, G.; Liu, B.; Wachsman, E.; Wang, H.; Hu, L. In Situ Neutron Depth Profiling of Lithium Metal–Garnet Interfaces for Solid State Batteries. *J. Am. Chem. Soc.* **2017**, *139* (40), 14257–14264. https://doi.org/10.1021/jacs.7b07904.

(136) Han, F.; Westover, A. S.; Yue, J.; Fan, X.; Wang, F.; Chi, M.; Leonard, D. N.; Dudney, N. J.; Wang, H.; Wang, C. High Electronic Conductivity as the Origin of Lithium Dendrite Formation within Solid Electrolytes. *Nature Energy* **2019**, *4* (3), 187–196. https://doi.org/10.1038/s41560-018-0312-z.

(137) Downing, R. G.; Lamaze, G. P.; Langland, J. K.; Hwang, S. T. Neutron Depth Profiling: Overview and Description of NIST Facilities. *J. RES. NATL. INST. STAN.* **1993**, *98* (1), 109. https://doi.org/10.6028/jres.098.008.

(138) Danilov, D. L.; Chen, C.; Jiang, M.; Eichel, R.-A.; Notten, P. H. L. On the Conversion of NDP Energy Spectra into Depth Concentration Profiles for Thin-Films All-Solid-State Batteries. *Radiation Effects and Defects in Solids* **2020**, *175* (3–4), 367–382. https://doi.org/10.1080/10420150.2019.1701468.

(139) Ziegler, J. SRIM & TRIM. *http://www.srim.org/* **2013**.

(140) Weaver, J. L. Neutron Depth Profiling Data Processing, 2019.

(141) *Introduction to Focused Ion Beams: Instrumentation, Theory, Techniques, and Practice*; Giannuzzi, L. A., Stevie, F. A., Eds.; Springer: New York, 2005.

(142) Lindquist, N. C.; Nagpal, P.; McPeak, K. M.; Norris, D. J.; Oh, S.-H. Engineering Metallic Nanostructures for Plasmonics and Nanophotonics. *Rep. Prog. Phys.* **2012**, *75* (3), 036501. https://doi.org/10.1088/0034-4885/75/3/036501.

(143) Volkert, C. A.; Minor, A. M. Focused Ion Beam Microscopy and Micromachining. *MRS Bulletin* **2007**, *32* (5), 389–399. https://doi.org/10.1557/mrs2007.62.

(144) Mayer, J.; Giannuzzi, L. A.; Kamino, T.; Michael, J. TEM Sample Preparation and FIB-Induced Damage. *MRS Bull.* **2007**, *32* (5), 400–407. https://doi.org/10.1557/mrs2007.63.

(145) Kim, M.; Ahn, N.; Cheng, D.; Xu, M.; Ham, S.-Y.; Pan, X.; Kim, S. J.; Luo, Y.; Fenning, D. P.; Tan, D. H. S.; Zhang, M.; Zhu, G.; Jeong, K.; Choi, M.; Meng, Y. S. Imaging Real-Time Amorphization of Hybrid Perovskite Solar Cells under Electrical Biasing. *ACS Energy Lett.* **2021**, *6* (10), 3530–3537. https://doi.org/10.1021/acsenergylett.1c01707.

(146) Placke, T.; Kloepsch, R.; Dühnen, S.; Winter, M. Lithium Ion, Lithium Metal, and Alternative Rechargeable Battery Technologies: The Odyssey for High Energy Density. *J Solid State Electrochem* **2017**, *21* (7), 1939–1964. https://doi.org/10.1007/s10008-017-3610-7.

(147) Reddy, M. V.; Mauger, A.; Julien, C. M.; Paolella, A.; Zaghib, K. Brief History of Early Lithium-Battery Development. *Materials* **2020**, *13* (8), 1884. https://doi.org/10.3390/ma13081884.

(148) Brandt, K. Historical Development of Secondary Lithium Batteries. *Solid State Ionics* **1994**, *69* (3), 173–183. https://doi.org/10.1016/0167-2738(94)90408-1.

(149) Ohzuku, T.; Brodd, R. J. An Overview of Positive-Electrode Materials for Advanced Lithium-Ion Batteries. *Journal of Power Sources* **2007**, *174* (2), 449–456. https://doi.org/10.1016/j.jpowsour.2007.06.154.

(150) Liu, J.; Bao, Z.; Cui, Y.; Dufek, E. J.; Goodenough, J. B.; Khalifah, P.; Li, Q.; Liaw, B. Y.; Liu, P.; Manthiram, A.; Meng, Y. S.; Subramanian, V. R.; Toney, M. F.; Viswanathan, V. V.; Whittingham, M. S.; Xiao, J.; Xu, W.; Yang, J.; Yang, X.-Q.; Zhang, J.-G. Pathways for Practical High-Energy Long-Cycling Lithium Metal Batteries. *Nat Energy* **2019**, *4* (3), 180–186. https://doi.org/10.1038/s41560-019-0338-x.

(151) Niu, C.; Liu, D.; Lochala, J. A.; Anderson, C. S.; Cao, X.; Gross, M. E.; Xu, W.; Zhang, J.-G.; Whittingham, M. S.; Xiao, J.; Liu, J. Balancing Interfacial Reactions to Achieve Long Cycle Life in High-Energy Lithium Metal Batteries. *Nat Energy* **2021**, 1–10. https://doi.org/10.1038/s41560-021-00852-3.

(152) Tarascon, J.-M.; Armand, M. Issues and Challenges Facing Rechargeable Lithium Batteries. *Nature* **2001**, *414* (6861), 359–367. https://doi.org/10.1038/35104644.

(153) Kim, T.; Song, W.; Son, D.-Y.; Ono, L. K.; Qi, Y. Lithium-Ion Batteries: Outlook on Present, Future, and Hybridized Technologies. *J. Mater. Chem. A* **2019**, *7* (7), 2942–2964. https://doi.org/10.1039/C8TA10513H.

(154) Liu, Y.-T.; Liu, S.; Li, G.-R.; Gao, X.-P. Strategy of Enhancing the Volumetric Energy Density for Lithium–Sulfur Batteries. *Advanced Materials* **2021**, *33* (8), 2003955. https://doi.org/10.1002/adma.202003955.

(155) Choi, J. W.; Aurbach, D. Promise and Reality of Post-Lithium-Ion Batteries with High Energy Densities. *Nat Rev Mater* **2016**, *1* (4), 1–16. https://doi.org/10.1038/natrevmats.2016.13.

(156) Yu, X.; Yu, W. A.; Manthiram, A. Advances and Prospects of High-Voltage Spinel Cathodes for Lithium-Based Batteries. *Small Methods* **2021**, *5* (5), 2001196. https://doi.org/10.1002/smtd.202001196.

(157) Xu, H.; Zhang, H.; Ma, J.; Xu, G.; Dong, T.; Chen, J.; Cui, G. Overcoming the Challenges of 5 V Spinel LiNi0.5Mn1.5O4 Cathodes with Solid Polymer Electrolytes. *ACS Energy Lett.* **2019**, *4* (12), 2871–2886. https://doi.org/10.1021/acsenergylett.9b01871.

(158) Lu, J.; Lee, K. S. Spinel Cathodes for Advanced Lithium Ion Batteries: A Review of Challenges and Recent Progress. *Materials Technology* **2016**, *31* (11), 628–641. https://doi.org/10.1080/10667857.2016.1208957.

(159) Park, S. H.; Oh, S. W.; Kang, S. H.; Belharouak, I.; Amine, K.; Sun, Y. K. Comparative Study of Different Crystallographic Structure of LiNi0.5Mn1.5O4-δ Cathodes with Wide Operation Voltage (2.0-5.0 V). *Electrochimica Acta* **2007**, *52* (25), 7226–7230. https://doi.org/10.1016/j.electacta.2007.05.050.

(160) Li, W.; Cho, Y.-G.; Yao, W.; Li, Y.; Cronk, A.; Shimizu, R.; Schroeder, M. A.; Fu, Y.; Zou, F.; Battaglia, V.; Manthiram, A.; Zhang, M.; Meng, Y. S. Enabling High Areal Capacity for Co-Free High Voltage Spinel Materials in next-Generation Li-Ion Batteries. *Journal of Power Sources* **2020**, *473*, 228579. https://doi.org/10.1016/j.jpowsour.2020.228579.

(161) Mancini, M.; Axmann, P.; Gabrielli, G.; Kinyanjui, M.; Kaiser, U.; Wohlfahrt-Mehrens, M. A High-Voltage and High-Capacity Li1+x Ni0.5 Mn1.5 O4 Cathode Material: From Synthesis to Full Lithium-Ion Cells. *ChemSusChem* **2016**, *9* (14), 1843–1849. https://doi.org/10.1002/cssc.201600365.

(162) Hofmann, A.; Höweling, A.; Bohn, N.; Müller, M.; Binder, J. R.; Hanemann, T. Additives for Cycle Life Improvement of High-Voltage LNMO-Based Li-Ion Cells. *ChemElectroChem* **2019**, *6* (20), 5255–5263. https://doi.org/10.1002/celc.201901120.

(163) Arbizzani, C.; De Giorgio, F.; Mastragostino, M. Characterization Tests for Plug-in Hybrid Electric Vehicle Application of Graphite/LiNi0.4Mn1.6O4 Cells with Two Different Separators and Electrolytes. *Journal of Power Sources* **2014**, *266*, 170–174. https://doi.org/10.1016/j.jpowsour.2014.05.016.

(164) Hu, L.; Amine, K.; Zhang, Z. Fluorinated Electrolytes for 5-V Li-Ion Chemistry: Dramatic Enhancement of LiNi0.5Mn1.5O4/Graphite Cell Performance by a Lithium Reservoir. *Electrochemistry Communications* **2014**, *44*, 34–37. https://doi.org/10.1016/j.elecom.2014.04.006.

(165) De Giorgio, F.; Laszczynski, N.; von Zamory, J.; Mastragostino, M.; Arbizzani, C.; Passerini, S. Graphite//LiNi0.5Mn1.5O4 Cells Based on Environmentally Friendly Made-in-Water Electrodes. *ChemSusChem* **2017**, *10* (2), 379–386. https://doi.org/10.1002/cssc.201601249.

(166) Lee, T. J.; Lee, J. B.; Yoon, T.; Kim, D.; Chae, O. B.; Jung, J.; Soon, J.; Ryu, J. H.; Kim, J. J.; Oh, S. M. Tris(Pentafluorophenyl)Silane as an Electrolyte Additive for 5 V

LiNi0.5Mn1.5O4 Positive Electrode. *J. Electrochem. Soc.* **2016**, *163* (6), A898. https://doi.org/10.1149/2.0501606jes.

(167) Milien, M. S.; Beyer, H.; Beichel, W.; Klose, P.; Gasteiger, H. A.; Lucht, B. L.; Krossing, I. Lithium Bis(2,2,2-Trifluoroethyl)Phosphate Li[O2P(OCH2CF3)2]: A High Voltage Additive for LNMO/Graphite Cells. *J. Electrochem. Soc.* **2018**, *165* (11), A2569. https://doi.org/10.1149/2.0541811jes.

(168) Li, Y.; Veith, G. M.; Browning, K. L.; Chen, J.; Hensley, D. K.; Paranthaman, M. P.; Dai, S.; Sun, X.-G. Lithium Malonatoborate Additives Enabled Stable Cycling of 5V Lithium Metal and Lithium Ion Batteries. *Nano Energy* **2017**, *40*, 9–19. https://doi.org/10.1016/j.nanoen.2017.07.051.

(169) Kim, C.-K.; Kim, K.; Shin, K.; Woo, J.-J.; Kim, S.; Hong, S. Y.; Choi, N.-S. Synergistic Effect of Partially Fluorinated Ether and Fluoroethylene Carbonate for High-Voltage Lithium-Ion Batteries with Rapid Chargeability and Dischargeability. *ACS Appl. Mater. Interfaces* **2017**, *9* (50), 44161–44172. https://doi.org/10.1021/acsami.7b12352.

(170) Solchenbach, S.; Wetjen, M.; Pritzl, D.; Schwenke, K. U.; Gasteiger, H. A. Lithium Oxalate as Capacity and Cycle-Life Enhancer in LNMO/Graphite and LNMO/SiG Full Cells. *J. Electrochem. Soc.* **2018**, *165* (3), A512. https://doi.org/10.1149/2.0611803jes.

(171) Alvarado, J.; Schroeder, M. A.; Zhang, M.; Borodin, O.; Gobrogge, E.; Olguin, M.; Ding, M. S.; Gobet, M.; Greenbaum, S.; Meng, Y. S.; Xu, K. A Carbonate-Free, Sulfone-Based Electrolyte for High-Voltage Li-Ion Batteries. *Materials Today* **2018**, *21* (4), 341–353. https://doi.org/10.1016/j.mattod.2018.02.005.

(172) Xu, G.; Pang, C.; Chen, B.; Ma, J.; Wang, X.; Chai, J.; Wang, Q.; An, W.; Zhou, X.; Cui, G.; Chen, L. Prescribing Functional Additives for Treating the Poor Performances of High-Voltage (5 V-Class) LiNi0.5Mn1.5O4/MCMB Li-Ion Batteries. *Advanced Energy Materials* **2018**, *8* (9), 1–14. https://doi.org/10.1002/aenm.201701398.

(173) Herbert, E. G.; Tenhaeff, W. E.; Dudney, N. J.; Pharr, G. M. Mechanical Characterization of LiPON Films Using Nanoindentation. *Thin Solid Films* **2011**, *520* (1), 413–418. https://doi.org/10.1016/j.tsf.2011.07.068.

(174) Marple, M. A. T.; Wynn, T. A.; Cheng, D.; Shimizu, R.; Mason, H. E.; Meng, Y. S. Local Structure of Glassy Lithium Phosphorus Oxynitride Thin Films: A Combined Experimental and Ab Initio Approach. *Angewandte Chemie International Edition* **2020**, *59* (49), 22185–22193. https://doi.org/10.1002/anie.202009501.

(175) Song, J.; Shin, D. W.; Lu, Y.; Amos, C. D.; Manthiram, A.; Goodenough, J. B. Role of Oxygen Vacancies on the Performance of Li[Ni 0.5-XMn 1.5+ x]O 4 (x = 0, 0.05, and 0.08) Spinel Cathodes for Lithium-Ion Batteries. *Chemistry of Materials* **2012**, *24* (15), 3101–3109. https://doi.org/10.1021/cm301825h.

(176) Lee, E. S.; Nam, K. W.; Hu, E.; Manthiram, A. Influence of Cation Ordering and Lattice Distortion on the Charge-Discharge Behavior of LiMn 1.5 Ni 0.5 O 4 Spinel between 5.0

and 2.0 v. *Chemistry of Materials* **2012**, *24* (18), 3610–3620. https://doi.org/10.1021/cm3020836.

(177) Lamaze, G. P.; Chen-Mayer, H. H.; Becker, D. A.; Vereda, F.; Goldner, R. B.; Haas, T.; Zerigian, P. Cold Neutron Depth Profiling of Lithium-Ion Battery Materials. *Journal of Power Sources* **2003**, *119–121*, 680–685. https://doi.org/10.1016/S0378-7753(03)00232-5.

(178) Tan, C.; Leung, K. Y.; Liu, D. X.; Canova, M.; Downing, R. G.; Co, A. C.; Cao, L. R. Gamma Radiation Effects on Li-Ion Battery Electrolyte in Neutron Depth Profiling for Lithium Quantification. *J Radioanal Nucl Chem* **2015**, *305* (2), 675–680. https://doi.org/10.1007/s10967-015-4006-8.

(179) Nagpure, S. C.; Downing, R. G.; Bhushan, B.; Babu, S. S.; Cao, L. Neutron Depth Profiling Technique for Studying Aging in Li-Ion Batteries. *Electrochimica Acta* **2011**, *56* (13), 4735–4743. https://doi.org/10.1016/j.electacta.2011.02.037.

(180) Zhang, X.; Verhallen, T. W.; Labohm, F.; Wagemaker, M. Direct Observation of Li-Ion Transport in Electrodes under Nonequilibrium Conditions Using Neutron Depth Profiling. *Advanced Energy Materials* **2015**, *5* (15), 1500498. https://doi.org/10.1002/aenm.201500498.

(181) Tomandl, I.; Vacik, J.; Kobayashi, T.; Sierra, Y. M.; Hnatowicz, V.; Lavreniev, V.; Horak, P.; Ceccio, G.; Cannavo, A.; Baba, M.; Ye, R. Analysis of Li Distribution in Ultrathin All-Solid-State Li-Ion Battery (ASSLiB) by Neutron Depth Profiling (NDP). *Radiation Effects and Defects in Solids* **2020**, *175* (3–4), 394–405. https://doi.org/10.1080/10420150.2019.1701471.

(182) Weaver, J. L.; Jobs, A.; Downing, R. G. Energy Broadening of Neutron Depth Profiles by Thin Polyamide Films. *Under Review*.

(183) J. Lyons, D.; L. Weaver, J.; C. Co, A. Considerations in Applying Neutron Depth Profiling (NDP) to Li-Ion Battery Research. *Journal of Materials Chemistry A* **2022**, *10* (5), 2336–2351. https://doi.org/10.1039/D1TA09639G.

(184) Intan, N. N.; Klyukin, K.; Alexandrov, V. Theoretical Insights into Oxidation States of Transition Metals at (001) and (111) LiNi 0.5 Mn 1.5 O 4 Spinel Surfaces. *Journal of The Electrochemical Society* **2018**, *165* (5), A1099–A1103. https://doi.org/10.1149/2.1251805jes.

(185) Xu, B.; Fell, C. R.; Chi, M.; Meng, Y. S. Identifying Surface Structural Changes in Layered Li-Excess Nickel Manganese Oxides in High Voltage Lithium Ion Batteries: A Joint Experimental and Theoretical Study. *Energy and Environmental Science* **2011**, *4* (6), 2223–2233. https://doi.org/10.1039/c1ee01131f.

(186) Wang, Z. L.; Yin, J. S.; Jiang, Y. D. EELS Analysis of Cation Valence States and Oxygen Vacancies in Magnetic Oxides. *Micron* **2000**, *31* (5), 571–580. https://doi.org/10.1016/S0968-4328(99)00139-0.

(187) Liang, W.; Wang, P.; Ding, H.; Wang, B.; Li, S. Granularity Control Enables High Stability and Elevated-Temperature Properties of Micron-Sized Single-Crystal LiNi0.5Mn1.5O4 Cathodes at High Voltage. *Journal of Materiomics* **2021**, *7* (5), 1049–1060. https://doi.org/10.1016/j.jmat.2021.02.003.

(188) Luo, S.; Li, J.; Lu, J.; Tao, F.; Wan, J.; Zhang, B.; Zhou, X.; Hu, C. High-Performance Aqueous Asymmetric Supercapacitor Based on Hierarchical Wheatear-like LiNi0.5Mn1.5O4 Cathode and Porous Fe2O3 Anode. *Materials Today Physics* **2021**, *17*, 100337. https://doi.org/10.1016/j.mtphys.2020.100337.

(189) Schichtel, P.; Geiß, M.; Leichtweiß, T.; Sann, J.; Weber, D. A.; Janek, J. On the Impedance and Phase Transition of Thin Film All-Solid-State Batteries Based on the Li4Ti5O12 System. *Journal of Power Sources* **2017**, *360*, 593–604. https://doi.org/10.1016/j.jpowsour.2017.06.044.

(190) Usubelli, C.; Besli, M. M.; Kuppan, S.; Jiang, N.; Metzger, M.; Dinia, A.; Christensen, J.; Gorlin, Y. Understanding the Overlithiation Properties of LiNi0.6Mn0.2Co0.2O2 Using Electrochemistry and Depth-Resolved X-Ray Absorption Spectroscopy. *J. Electrochem. Soc.* **2020**, *167* (8), 080514. https://doi.org/10.1149/1945-7111/ab8a9d.

(191) Takada, K.; Ohno, T.; Ohta, N.; Ohnishi, T.; Tanaka, Y. Positive and Negative Aspects of Interfaces in Solid-State Batteries. *ACS Energy Lett.* **2018**, *3* (1), 98–103. https://doi.org/10.1021/acsenergylett.7b01105.

(192) de Klerk, N. J. J.; Wagemaker, M. Space-Charge Layers in All-Solid-State Batteries; Important or Negligible? *ACS Appl. Energy Mater.* **2018**, *1* (10), 5609–5618. https://doi.org/10.1021/acsaem.8b01141.

(193) Xia, Q.; Sun, S.; Xu, J.; Zan, F.; Yue, J.; Zhang, Q.; Gu, L.; Xia, H. Self-Standing 3D Cathodes for All-Solid-State Thin Film Lithium Batteries with Improved Interface Kinetics. *Small* **2018**, *14* (52), 1804149. https://doi.org/10.1002/smll.201804149.

(194) Sharafi, A.; Meyer, H. M.; Nanda, J.; Wolfenstine, J.; Sakamoto, J. Characterizing the Li–Li7La3Zr2O12 Interface Stability and Kinetics as a Function of Temperature and Current Density. *Journal of Power Sources* **2016**, *302*, 135–139. https://doi.org/10.1016/j.jpowsour.2015.10.053.

(195) Doux, J.-M.; Yang, Y.; Tan, D. H. S.; Nguyen, H.; Wu, E. A.; Wang, X.; Banerjee, A.; Meng, Y. S. Pressure Effects on Sulfide Electrolytes for All Solid-State Batteries. *J. Mater. Chem. A* **2020**, *8* (10), 5049–5055. https://doi.org/10.1039/C9TA12889A.

(196) Zhang, W.; Leichtweiß, T.; Culver, S. P.; Koerver, R.; Das, D.; Weber, D. A.; Zeier, W. G.; Janek, J. The Detrimental Effects of Carbon Additives in Li10GeP2S12-Based Solid-State Batteries. *ACS Appl. Mater. Interfaces* **2017**, *9* (41), 35888–35896. https://doi.org/10.1021/acsami.7b11530.

(197) Tan, D. H. S.; Wu, E. A.; Nguyen, H.; Chen, Z.; Marple, M. A. T.; Doux, J.-M.; Wang, X.; Yang, H.; Banerjee, A.; Meng, Y. S. Elucidating Reversible Electrochemical Redox of

Li6PS5Cl Solid Electrolyte. *ACS Energy Lett.* **2019**, *4* (10), 2418–2427. https://doi.org/10.1021/acsenergylett.9b01693.

(198) Tan, D. H. S.; Chen, Y.-T.; Yang, H.; Bao, W.; Sreenarayanan, B.; Doux, J.-M.; Li, W.; Lu, B.; Ham, S.-Y.; Sayahpour, B.; Scharf, J.; Wu, E. A.; Deysher, G.; Han, H. E.; Hah, H. J.; Jeong, H.; Lee, J. B.; Chen, Z.; Meng, Y. S. Carbon-Free High-Loading Silicon Anodes Enabled by Sulfide Solid Electrolytes. *Science* **2021**, *373* (6562), 1494–1499. https://doi.org/10.1126/science.abg7217.

(199) Kim, J. H.; Park, J.; Cheong, J. Y.; Song, A.; Chung, K. B.; Park, Y. C.; Kim, I. D.; Kim, Y. J.; Park, K.; Kim, H. S. Suppressed Ionic Contamination of LiNi0.5Mn1.5O4 with a Pt/ITO/Stainless Steel Multilayer Current Collector. *Ceramics International* **2018**, *44* (16), 20093–20104. https://doi.org/10.1016/j.ceramint.2018.07.284.

(200) Li, Y.; Wang, Z.; Midya, R.; Xia, Q.; Yang, J. J. Review of Memristor Devices in Neuromorphic Computing: Materials Sciences and Device Challenges. *J. Phys. D: Appl. Phys.* **2018**, *51* (50), 503002. https://doi.org/10.1088/1361-6463/aade3f.

(201) Kim, S. J.; Kim, S. B.; Jang, H. W. Competing Memristors for Brain-Inspired Computing. *iScience* **2021**, *24* (1), 101889. https://doi.org/10.1016/j.isci.2020.101889.

(202) Dudney, N. J. Solid-State Thin-Film Rechargeable Batteries. *Materials Science and Engineering B: Solid-State Materials for Advanced Technology* **2005**, *116* (3 SPEC.ISS.), 245–249. https://doi.org/10.1016/j.mseb.2004.05.045.

(203) Gao, P.; Wang, Z.; Fu, W.; Liao, Z.; Liu, K.; Wang, W.; Bai, X.; Wang, E. In Situ TEM Studies of Oxygen Vacancy Migration for Electrically Induced Resistance Change Effect in Cerium Oxides. *Micron* **2010**, *41* (4), 301–305. https://doi.org/10.1016/j.micron.2009.11.010.

(204) Das, U.; Das, D.; Paul, B.; Rabha, T.; Pattanayak, S.; Kanjilal, A.; Bhattacharjee, S.; Sarkar, P.; Roy, A. Induced Vacancy-Assisted Filamentary Resistive Switching Device Based on RbPbI3–XClx Perovskite for RRAM Application. *ACS Appl. Mater. Interfaces* **2020**, *12* (37), 41718–41727. https://doi.org/10.1021/acsami.0c10123.

(205) Verde, M. G.; Baggetto, L.; Balke, N.; Veith, G. M.; Seo, J. K.; Wang, Z.; Meng, Y. S. Elucidating the Phase Transformation of Li4Ti5O12 Lithiation at the Nanoscale. *ACS Nano* **2016**, *10* (4), 4312–4321. https://doi.org/10.1021/acsnano.5b07875.

(206) Ko, C.; Ramanathan, S. Observation of Electric Field-Assisted Phase Transition in Thin Film Vanadium Oxide in a Metal-Oxide-Semiconductor Device Geometry. *Appl. Phys. Lett.* **2008**, *93* (25), 252101. https://doi.org/10.1063/1.3050464.

(207) Shi, T.; Wu, J.-F.; Liu, Y.; Yang, R.; Guo, X. Behavioral Plasticity Emulated with Lithium Lanthanum Titanate-Based Memristive Devices: Habituation. *Advanced Electronic Materials* **2017**, *3* (9), 1700046. https://doi.org/10.1002/aelm.201700046.

(208) Deng, Y.; Xu, X.; Zhang, L.; Du, F.; Liu, Q.; Chen, J.; Meng, K.; Wu, Y.; Yang, M.; Jiang, Y. Lithium Incorporation Enhanced Resistive Switching Behaviors in Lithium Lanthanum Titanium Oxide-Based Heterostructure. *Journal of Materials Science & Technology* **2022**, *128*, 142–147. https://doi.org/10.1016/j.jmst.2022.04.029.

(209) Kresse, G.; Joubert, D. From Ultrasoft Pseudopotentials to the Projector Augmented-Wave Method. *Phys. Rev. B* **1999**, *59* (3), 1758–1775. https://doi.org/10.1103/PhysRevB.59.1758.

(210) Perdew, J. P.; Burke, K.; Ernzerhof, M. Generalized Gradient Approximation Made Simple. *Phys. Rev. Lett.* **1996**, *77* (18), 3865–3868. https://doi.org/10.1103/PhysRevLett.77.3865.

(211) Momma, K.; Izumi, F. VESTA 3 for Three-Dimensional Visualization of Crystal, Volumetric and Morphology Data. *J Appl Cryst* **2011**, *44* (6), 1272–1276. https://doi.org/10.1107/S0021889811038970.

(212) Kim, K. M.; Zhang, J.; Graves, C.; Yang, J. J.; Choi, B. J.; Hwang, C. S.; Li, Z.; Williams, R. S. Low-Power, Self-Rectifying, and Forming-Free Memristor with an Asymmetric Programing Voltage for a High-Density Crossbar Application. *Nano Lett.* **2016**, *16* (11), 6724–6732. https://doi.org/10.1021/acs.nanolett.6b01781.

(213) Hulbert, B. S.; McCormack, S. J.; Tseng, K.-P.; Kriven, W. M. Thermal Expansion and Phase Transformation in the Rare Earth Di-Titanate ($R_2 Ti_2 O_7$) System. *Acta Crystallogr B Struct Sci Cryst Eng Mater* **2021**, *77* (3), 397–407. https://doi.org/10.1107/S2052520621004479.

(214) Li, Y.; Yang, Y.; Shu, X.; Wan, D.; Wei, N.; Yu, X.; Breese, M. B. H.; Venkatesan, T.; Xue, J. M.; Liu, Y.; Li, S.; Wu, T.; Chen, J. From Titanium Sesquioxide to Titanium Dioxide: Oxidation-Induced Structural, Phase, and Property Evolution. *Chem. Mater.* **2018**, *30* (13), 4383–4392. https://doi.org/10.1021/acs.chemmater.8b01739.

(215) Das, T. K.; Ilaiyaraja, P.; Mocherla, P. S. V.; Bhalerao, G. M.; Sudakar, C. Influence of Surface Disorder, Oxygen Defects and Bandgap in TiO2 Nanostructures on the Photovoltaic Properties of Dye Sensitized Solar Cells. *Solar Energy Materials and Solar Cells* **2016**, *144*, 194–209. https://doi.org/10.1016/j.solmat.2015.08.036.

(216) Nakamura, I.; Negishi, N.; Kutsuna, S.; Ihara, T.; Sugihara, S.; Takeuchi, K. Role of Oxygen Vacancy in the Plasma-Treated TiO2 Photocatalyst with Visible Light Activity for NO Removal. *Journal of Molecular Catalysis A: Chemical* **2000**, *161* (1), 205–212. https://doi.org/10.1016/S1381-1169(00)00362-9.

(217) Wang, M. J.; Wolfenstine, J. B.; Sakamoto, J. Mixed Electronic and Ionic Conduction Properties of Lithium Lanthanum Titanate. *Advanced Functional Materials* **2020**, *30* (10), 1909140. https://doi.org/10.1002/adfm.201909140.

(218) Wenzel, S.; Leichtweiss, T.; Krüger, D.; Sann, J.; Janek, J. Interphase Formation on Lithium Solid Electrolytes—An in Situ Approach to Study Interfacial Reactions by Photoelectron Spectroscopy. *Solid State Ionics* **2015**, *278*, 98–105. https://doi.org/10.1016/j.ssi.2015.06.001.

(219) Wolfenstine, J.; Allen, J. L.; Read, J.; Sakamoto, J.; Gonalez-Doncel, G. Hot-Pressed Li0.33La0.57TiO3. *Journal of Power Sources* **2010**, *195* (13), 4124–4128. https://doi.org/10.1016/j.jpowsour.2009.12.109.

(220) Yang, K.-Y.; Leu, I.-C.; Fung, K.-Z.; Hon, M.-H.; Hsu, M.-C.; Hsiao, Y.-J.; Wang, M.-C. Mechanism of the Interfacial Reaction between Cation-Deficient La $_{0.56}$ Li $_{0.33}$ TiO $_3$ and Metallic Lithium at Room Temperature. *J. Mater. Res.* **2008**, *23* (7), 1813–1825. https://doi.org/10.1557/JMR.2008.0255.

(221) Reynolds, C. D.; Slater, P. R.; Hare, S. D.; Simmons, M. J. H.; Kendrick, E. A Review of Metrology in Lithium-Ion Electrode Coating Processes. *Materials & Design* **2021**, *209*, 109971. https://doi.org/10.1016/j.matdes.2021.109971.

(222) Liu, Y.; Zhang, R.; Wang, J.; Wang, Y. Current and Future Lithium-Ion Battery Manufacturing. *iScience* **2021**, *24* (4), 102332. https://doi.org/10.1016/j.isci.2021.102332.

(223) Schwietert, T. K.; Arszelewska, V. A.; Wang, C.; Yu, C.; Vasileiadis, A.; de Klerk, N. J. J.; Hageman, J.; Hupfer, T.; Kerkamm, I.; Xu, Y.; van der Maas, E.; Kelder, E. M.; Ganapathy, S.; Wagemaker, M. Clarifying the Relationship between Redox Activity and Electrochemical Stability in Solid Electrolytes. *Nat. Mater.* **2020**, *19* (4), 428–435. https://doi.org/10.1038/s41563-019-0576-0.

(224) Baggetto, L.; Dudney, N. J.; Veith, G. M. Surface Chemistry of Metal Oxide Coated Lithium Manganese Nickel Oxide Thin Film Cathodes Studied by XPS. *Electrochimica Acta* **2013**, *90*, 135–147. https://doi.org/10.1016/j.electacta.2012.11.120.

(225) Hou, T.; Yang, G.; Rajput, N. N.; Self, J.; Park, S.-W.; Nanda, J.; Persson, K. A. The Influence of FEC on the Solvation Structure and Reduction Reaction of LiPF6/EC Electrolytes and Its Implication for Solid Electrolyte Interphase Formation. *Nano Energy* **2019**, *64* (May), 103881. https://doi.org/10.1016/j.nanoen.2019.103881.

(226) Suo, L.; Xue, W.; Gobet, M.; Greenbaum, S. G.; Wang, C.; Chen, Y.; Yang, W.; Li, Y.; Li, J. Fluorine-Donating Electrolytes Enable Highly Reversible 5-V-Class Li Metal Batteries. *Proceedings of the National Academy of Sciences of the United States of America* **2018**, *115* (6), 1156–1161. https://doi.org/10.1073/pnas.1712895115.

(227) Yan, G.; Li, X.; Wang, Z.; Guo, H.; Peng, W.; Hu, Q.; Wang, J. Fluorinated Solvents for High-Voltage Electrolyte in Lithium-Ion Battery. *Journal of Solid State Electrochemistry* **2017**, *21* (6), 1589–1597. https://doi.org/10.1007/s10008-017-3508-4.

(228) Xu, Y.; Liu, J.; Zhou, L.; Zeng, L.; Yang, Z. FEC as the Additive of 5 V Electrolyte and Its Electrochemical Performance for LiNi0.5Mn1.5O4. *Journal of Electroanalytical Chemistry* **2017**, *791*, 109–116. https://doi.org/10.1016/j.jelechem.2017.03.017.

(229) Xia, J.; Nie, M.; Burns, J. C.; Xiao, A.; Lamanna, W. M.; Dahn, J. R. Fluorinated Electrolyte for 4.5 v Li(Ni0.4Mn0.4Co0.2)O2/Graphite Li-Ion Cells. *Journal of Power Sources* **2016**, *307*, 340–350. https://doi.org/10.1016/j.jpowsour.2015.12.132.

(230) Delp, S. A.; Borodin, O.; Olguin, M.; Eisner, C. G.; Allen, J. L.; Jow, T. R. Importance of Reduction and Oxidation Stability of High Voltage Electrolytes and Additives. *Electrochimica Acta* **2016**, *209*, 498–510. https://doi.org/10.1016/j.electacta.2016.05.100.

(231) He, M.; Hu, L.; Xue, Z.; Su, C. C.; Redfern, P.; Curtiss, L. A.; Polzin, B.; Von Cresce, A.; Xu, K.; Zhang, Z. Fluorinated Electrolytes for 5-V Li-Ion Chemistry: Probing Voltage Stability of Electrolytes with Electrochemical Floating Test. *Journal of the Electrochemical Society* **2015**, *162* (9), A1725–A1729. https://doi.org/10.1149/2.0231509jes.

(232) Borodin, O.; Olguin, M.; Spear, C. E.; Leiter, K. W.; Knap, J. Towards High Throughput Screening of Electrochemical Stability of Battery Electrolytes. *Nanotechnology* **2015**, *26* (35). https://doi.org/10.1088/0957-4484/26/35/354003.

(233) Hood, Z. D.; Chen, X.; Sacci, R. L.; Liu, X.; Veith, G. M.; Mo, Y.; Niu, J.; Dudney, N. J.; Chi, M. Elucidating Interfacial Stability between Lithium Metal Anode and Li Phosphorus Oxynitride via In Situ Electron Microscopy. *Nano Lett.* **2021**, *21* (1), 151–157. https://doi.org/10.1021/acs.nanolett.0c03438.

(234) Wang, X.; Zhang, M.; Alvarado, J.; Wang, S.; Sina, M.; Lu, B.; Bouwer, J.; Xu, W.; Xiao, J.; Zhang, J.-G.; Liu, J.; Meng, Y. S. New Insights on the Structure of Electrochemically Deposited Lithium Metal and Its Solid Electrolyte Interphases via Cryogenic TEM. *Nano Letters* **2017**, *17* (12), 7606–7612. https://doi.org/10.1021/acs.nanolett.7b03606.

(235) Wilkinson, D. P.; Blom, H.; Brandt, K.; Wainwright, D. Effects of Physical Constraints on Li Cyclability. *Journal of Power Sources* **1991**, *36* (4), 517–527. https://doi.org/10.1016/0378-7753(91)80077-B.

(236) Louli, A. J.; Genovese, M.; Weber, R.; Hames, S. G.; Logan, E. R.; Dahn, J. R. Exploring the Impact of Mechanical Pressure on the Performance of Anode-Free Lithium Metal Cells. *J. Electrochem. Soc.* **2019**, *166* (8), A1291. https://doi.org/10.1149/2.0091908jes.

(237) Hirai, T.; Yoshimatsu, I.; Yamaki, J. Influence of Electrolyte on Lithium Cycling Efficiency with Pressurized Electrode Stack. *J. Electrochem. Soc.* **1994**, *141* (3), 611. https://doi.org/10.1149/1.2054778.

(238) Yin, X.; Tang, W.; Jung, I. D.; Phua, K. C.; Adams, S.; Lee, S. W.; Zheng, G. W. Insights into Morphological Evolution and Cycling Behaviour of Lithium Metal Anode under Mechanical Pressure. *Nano Energy* **2018**, *50*, 659–664. https://doi.org/10.1016/j.nanoen.2018.06.003.

(239) Weber, R.; Genovese, M.; Louli, A. J.; Hames, S.; Martin, C.; Hill, I. G.; Dahn, J. R. Long Cycle Life and Dendrite-Free Lithium Morphology in Anode-Free Lithium Pouch Cells Enabled by a Dual-Salt Liquid Electrolyte. *Nat Energy* **2019**, *4* (8), 683–689. https://doi.org/10.1038/s41560-019-0428-9.

(240) Zhang, X.; Wang, Q. J.; Harrison, K. L.; Jungjohann, K.; Boyce, B. L.; Roberts, S. A.; Attia, P. M.; Harris, S. J. Rethinking How External Pressure Can Suppress Dendrites in Lithium

Metal Batteries. *J. Electrochem. Soc.* **2019**, *166* (15), A3639. https://doi.org/10.1149/2.0701914jes.

(241) Fang, C.; Lu, B.; Pawar, G.; Zhang, M.; Cheng, D.; Chen, S.; Ceja, M.; Doux, J.-M.; Musrock, H.; Cai, M.; Liaw, B.; Meng, Y. S. Pressure-Tailored Lithium Deposition and Dissolution in Lithium Metal Batteries. *Nat Energy* **2021**, *6* (10), 987–994. https://doi.org/10.1038/s41560-021-00917-3.

(242) Lu, B.; Bao, W.; Yao, W.; Doux, J.-M.; Fang, C.; Meng, Y. S. Editors' Choice—Methods—Pressure Control Apparatus for Lithium Metal Batteries. *J. Electrochem. Soc.* **2022**, *169* (7), 070537. https://doi.org/10.1149/1945-7111/ac834c.

(243) Wang, M. J.; Choudhury, R.; Sakamoto, J. Characterizing the Li-Solid-Electrolyte Interface Dynamics as a Function of Stack Pressure and Current Density. *Joule* **2019**, *3* (9), 2165–2178. https://doi.org/10.1016/j.joule.2019.06.017.

(244) Kasemchainan, J.; Zekoll, S.; Spencer Jolly, D.; Ning, Z.; Hartley, G. O.; Marrow, J.; Bruce, P. G. Critical Stripping Current Leads to Dendrite Formation on Plating in Lithium Anode Solid Electrolyte Cells. *Nat. Mater.* **2019**, *18* (10), 1105–1111. https://doi.org/10.1038/s41563-019-0438-9.

(245) Yan, H.; Tantratian, K.; Ellwood, K.; Harrison, E. T.; Nichols, M.; Cui, X.; Chen, L. How Does the Creep Stress Regulate Void Formation at the Lithium-Solid Electrolyte Interface during Stripping? *Advanced Energy Materials* **2022**, *12* (2), 2102283. https://doi.org/10.1002/aenm.202102283.

(246) Doux, J.-M.; Nguyen, H.; Tan, D. H. S.; Banerjee, A.; Wang, X.; Wu, E. A.; Jo, C.; Yang, H.; Meng, Y. S. Stack Pressure Considerations for Room-Temperature All-Solid-State Lithium Metal Batteries. *Advanced Energy Materials* **2020**, *10* (1), 1903253. https://doi.org/10.1002/aenm.201903253.

(247) Ham, S.-Y.; Yang, H.; Nunez-cuacuas, O.; Tan, D. H. S.; Chen, Y.-T.; Deysher, G.; Cronk, A.; Ridley, P.; Doux, J.-M.; Wu, E. A.; Jang, J.; Meng, Y. S. Assessing the Critical Current Density of All-Solid-State Li Metal Symmetric and Full Cells. *Energy Storage Materials* **2023**, *55*, 455–462. https://doi.org/10.1016/j.ensm.2022.12.013.

(248) Xie, J.; Li, J.; Mai, W.; Hong, G. A Decade of Advanced Rechargeable Batteries Development Guided by in Situ Transmission Electron Microscopy. *Nano Energy* **2021**, *83*, 105780. https://doi.org/10.1016/j.nanoen.2021.105780.

(249) Shao, R.; Chen, S.; Dou, Z.; Zhang, J.; Ma, X.; Zhu, R.; Xu, J.; Gao, P.; Yu, D. Atomic-Scale Probing of Reversible Li Migration in 1T-V1+xSe2 and the Interactions between Interstitial V and Li. *Nano Lett.* **2018**, *18* (9), 6094–6099. https://doi.org/10.1021/acs.nanolett.8b03154.

(250) Li, Q.; Yao, Z.; Lee, E.; Xu, Y.; Thackeray, M. M.; Wolverton, C.; Dravid, V. P.; Wu, J. Dynamic Imaging of Crystalline Defects in Lithium-Manganese Oxide Electrodes during

Electrochemical Activation to High Voltage. *Nat Commun* **2019**, *10* (1), 1692. https://doi.org/10.1038/s41467-019-09408-2.

(251) Li, Q.; Wu, J.; Yao, Z.; Xu, Y.; Thackeray, M. M.; Wolverton, C.; Dravid, V. P. Dynamic Imaging of Metastable Reaction Pathways in Lithiated Cobalt Oxide Electrodes. *Nano Energy* **2018**, *44*, 15–22. https://doi.org/10.1016/j.nanoen.2017.11.052.

(252) Ryu, J.; Chen, T.; Bok, T.; Song, G.; Ma, J.; Hwang, C.; Luo, L.; Song, H.-K.; Cho, J.; Wang, C.; Zhang, S.; Park, S. Mechanical Mismatch-Driven Rippling in Carbon-Coated Silicon Sheets for Stress-Resilient Battery Anodes. *Nat Commun* **2018**, *9* (1), 2924. https://doi.org/10.1038/s41467-018-05398-9.

(253) An, W.; Gao, B.; Mei, S.; Xiang, B.; Fu, J.; Wang, L.; Zhang, Q.; Chu, P. K.; Huo, K. Scalable Synthesis of Ant-Nest-like Bulk Porous Silicon for High-Performance Lithium-Ion Battery Anodes. *Nat Commun* **2019**, *10* (1), 1447. https://doi.org/10.1038/s41467-019-09510-5.

(254) Tao, X.; Liu, Y.; Liu, W.; Zhou, G.; Zhao, J.; Lin, D.; Zu, C.; Sheng, O.; Zhang, W.; Lee, H.-W.; Cui, Y. Solid-State Lithium–Sulfur Batteries Operated at 37 °C with Composites of Nanostructured Li7La3Zr2O12/Carbon Foam and Polymer. *Nano Lett.* **2017**, *17* (5), 2967–2972. https://doi.org/10.1021/acs.nanolett.7b00221.

(255) Cheng, Q.; Li, A.; Li, N.; Li, S.; Zangiabadi, A.; Li, T.-D.; Huang, W.; Li, A. C.; Jin, T.; Song, Q.; Xu, W.; Ni, N.; Zhai, H.; Dontigny, M.; Zaghib, K.; Chuan, X.; Su, D.; Yan, K.; Yang, Y. Stabilizing Solid Electrolyte-Anode Interface in Li-Metal Batteries by Boron Nitride-Based Nanocomposite Coating. *Joule* **2019**, *3* (6), 1510–1522. https://doi.org/10.1016/j.joule.2019.03.022.

(256) *Temperature-Dependent Behavior of piezo actuator*. Temperature-Dependent Behavior , PI Ceramic GmbH. https://www.piceramic.com/en/expertise/piezo-technology/properties-piezo-actuators/temperature-dependence.

(257) Sun, C.; Liao, X.; Xia, F.; Zhao, Y.; Zhang, L.; Mu, S.; Shi, S.; Li, Y.; Peng, H.; Van Tendeloo, G.; Zhao, K.; Wu, J. High-Voltage Cycling Induced Thermal Vulnerability in LiCoO2 Cathode: Cation Loss and Oxygen Release Driven by Oxygen Vacancy Migration. *ACS Nano* **2020**, *14* (5), 6181–6190. https://doi.org/10.1021/acsnano.0c02237.

(258) Nikam, R. D.; Kwak, M.; Lee, J.; Rajput, K. G.; Banerjee, W.; Hwang, H. Near Ideal Synaptic Functionalities in Li Ion Synaptic Transistor Using Li3POxSex Electrolyte with High Ionic Conductivity. *Sci Rep* **2019**, *9* (1), 18883. https://doi.org/10.1038/s41598-019-55310-8.

(259) Tang, J.; Bishop, D.; Kim, S.; Copel, M.; Gokmen, T.; Todorov, T.; Shin, S.; Lee, K.-T.; Solomon, P.; Chan, K.; Haensch, W.; Rozen, J. ECRAM as Scalable Synaptic Cell for High-Speed, Low-Power Neuromorphic Computing. In *2018 IEEE International Electron Devices Meeting (IEDM)*; IEEE: San Francisco, CA, 2018; p 13.1.1-13.1.4. https://doi.org/10.1109/IEDM.2018.8614551.

(260) Lee, J.; Nikam, R. D.; Lim, S.; Kwak, M.; Hwang, H. Excellent Synaptic Behavior of Lithium-Based Nano-Ionic Transistor Based on Optimal WO2.7 Stoichiometry with High Ion Diffusivity. *Nanotechnology* **2020**, *31* (23), 235203. https://doi.org/10.1088/1361-6528/ab793d.

(261) Lee, K.; Kwak, M.; Choi, W.; Lee, C.; Lee, J.; Noh, S.; Lee, J.; Lee, H.; Hwang, H. Improved Synaptic Functionalities of Li-Based Nano-Ionic Synaptic Transistor with Ultralow Conductance Enabled by Al2O3 Barrier Layer. *Nanotechnology* **2021**, *32* (27), 275201. https://doi.org/10.1088/1361-6528/abf071.

(262) Li, Y.; Xuan, Z.; Lu, J.; Wang, Z.; Zhang, X.; Wu, Z.; Wang, Y.; Xu, H.; Dou, C.; Kang, Y.; Liu, Q.; Lv, H.; Shang, D. One Transistor One Electrolyte-Gated Transistor Based Spiking Neural Network for Power-Efficient Neuromorphic Computing System. *Advanced Functional Materials* **2021**, *31* (26), 2100042. https://doi.org/10.1002/adfm.202100042.

(263) Sandbaumhüter, F.; Agbo, S. N.; Tsai, C.-L.; Astakhov, O.; Uhlenbruck, S.; Rau, U.; Merdzhanova, T. Compatibility Study towards Monolithic Self-Charging Power Unit Based on All-Solid Thin-Film Solar Module and Battery. *Journal of Power Sources* **2017**, *365*, 303–307. https://doi.org/10.1016/j.jpowsour.2017.08.103.

(264) Chen, G.; Fojtik, M.; Kim, D.; Fick, D.; Park, J.; Seok, M.; Chen, M.-T.; Foo, Z.; Sylvester, D.; Blaauw, D. Millimeter-Scale Nearly Perpetual Sensor System with Stacked Battery and Solar Cells. In *2010 IEEE International Solid-State Circuits Conference - (ISSCC)*; 2010; pp 288–289. https://doi.org/10.1109/ISSCC.2010.5433921.